Abstract

Bolometric Response of Superconducting Microbridges

and Single-Walled Carbon Nanotubes

Daniel Ferguson Santavicca

2009

A bolometer is a device that uses a temperature-dependent resistance to detect power. The strongly temperature-dependent resistance of a superconductor biased on its superconducting phase transition can be used to make an extremely sensitive bolometric detector. We have developed two different types of superconducting bolometers for applications in terahertz spectroscopy.

The first type of superconducting bolometer consists of a thin film niobium microbridge with a superconducting critical temperature of approximately 6 K. The device is made much smaller than the detection wavelength (~0.1-1 mm) to increase the sensitivity, and efficient coupling is achieved by integrating the microbridge in a planar terahertz antenna. The response time is set by electron-phonon coupling in the niobium, which can be faster than one nanosecond. This detector has been developed for applications in time-resolved terahertz spectroscopy, in which one uses a terahertz signal to probe the state of a dynamic system on nanosecond to microsecond timescales.

The second type of superconducting bolometer consists of a thin film titanium nanobridge with a superconducting critical temperature of 0.3 K. This device is designed to achieve extremely high sensitivity and is predicted to be capable of detecting

individual terahertz photons (energy ~1-10 meV). To test these devices, we have developed a new experimental technique in which the energy of a single terahertz photon is simulated by the absorbed energy of a fast microwave pulse. We find that, consistent with theoretical predictions, this device achieves sufficient energy resolution to detect single terahertz photons.

Finally, we discuss how the experimental techniques that we have developed to characterize superconducting bolometric detectors can also be used to study the physics of a different system, the single-walled carbon nanotube. Measurements of the bolometric response enable us to study the inelastic scattering processes in the nanotube. In particular, we are able to determine the thermal conductance for cooling of the nanotube electron system as a function of both the temperature of the electron system and the nanotube length.

Bolometric Response of Superconducting Microbridges and Single-Walled Carbon Nanotubes

A Dissertation
Presented to the Faculty of the Graduate School
of
Yale University
in Candidacy for the Degree of
Doctor of Philosophy

by
Daniel Ferguson Santavicca

Dissertation Director: Professor Daniel E. Prober

December 2009

Acknowledgements

First I would like to thank my advisor, Prof. Daniel Prober, whose ideas were the motivation for this work, and who has always been a strong advocate for his students. I also thank all the members of the Prober Lab with whom I have worked these past six years, including Anthony Annunziata, Joel Chudow, Dr. Luigi Frunzio, Dr. Yan Yin, Veronica Savu, Matthew Reese, Briana Jewczyn, and Zoe Pham-Jackel. The funding for this work has come from the National Science Foundation through NSF-CHE, NSF-DMR, and NSF-AST, and also from Yale University.

Beyond our lab, I have benefited from the sharing of equipment and expertise with colleagues down the hall in the groups of Prof. Robert Schoelkopf and Prof. Michel Devoret. In particular, I thank Dr. Markus Brink for many helpful discussions on carbon nanotubes. It is especially important to acknowledge the device fabrication work performed by others, because without this none of the experiments described here would have been possible. The niobium microbolometers discussed in chapter 2 were fabricated with Anthony Annunziata, Matthew Reese, and Dr. Luigi Frunzio here at Yale. The titanium nanobolometer devices discussed in chapter 3 were fabricated by David Olaya in the group of Prof. Michael Gershenson at Rutgers University. Jian Wei and Dr. Sergey Pereverzev also worked on the development of this fabrication process at Rutgers. The nanotube sample discussed in chapter 4 was grown and patterned by Meninder Purewal

in the group of Prof. Philip Kim at Columbia University. Joel Chudow has also worked on nanotube growth and fabrication for terahertz measurements, discussed briefly at the end of chapter 4, which are presently in the development stage.

This work has benefited considerably from several fruitful collaborations. I learned much of what I know about terahertz spectroscopy from working with the group of Prof. Charles Schmuttenmaer in the Chemistry Department at Yale, especially from Alan True, Michael Williams, and Rebecca Milot. I learned a lot about measurement technique from Prof. Bertrand Reulet of the University of Paris - Orsay during his research visits to our lab. The work described in chapter 3 was begun working together with Prof. Reulet during his visit to our lab in the summer of 2008, and has been continued on his subsequent visit during the summer of 2009. I also benefited from interacting with several other faculty members who have been research visitors in our lab, including Prof. Aviad Frydman, Prof. Michael Reznikov, and Prof. Venkat Chandrasekhar. The work on the titanium nanobolometers is a collaboration with Dr. Boris Karasik at the Jet Propulsion Lab, and is part of a larger effort that he has been guiding forward since he first proposed this type of detector in 1999.

I would also like to thank the members of my committee – Prof. Victor Henrich, Prof. Charles Schmuttenmaer, and Prof. Robert Schoelkopf, as well as the outside reader, Prof. K. Sigfrid Yngvesson of the University of Massachusetts Amherst – for their careful reading of this thesis. The department administrators in Applied Physics – Giselle DeVito, Maria Gubitosi, and Terri Evangeliste – have made this a more pleasant place to study and work and deserve a special thank you. Finally, I would like to thank my wife, Becky, and my family for all their support over the years.

Table of Contents

List of Figures

List of Tables

Commonly used symbols and abbreviations

L	length
R	electrical resistance
R_n	normal state (non-superconducting) electrical resistance
G	thermal conductance
$G_{e\text{-}ph}$	electron-phonon thermal conductance
G_{diff}	electron diffusion thermal conductance
G_c	contact thermal conductance
κ	thermal conductivity
C	heat capacity
C_e	electronic heat capacity
τ	exponential time constant
τ_0	thermal time constant without electrothermal feedback
τ_{eff}	thermal time constant with electrothermal feedback
$\tau_{e\text{-}ph}$	electron-phonon inelastic scattering time
$\tau_{e\text{-}e}$	electron-electron inelastic scattering time
ℓ_e	electron mean free path
h	Planck's constant

k_B	Boltzmann's constant
$\mathscr{L}$	Lorenz number
ε	relative dielectric constant
Z	impedance
Γ	voltage reflection coefficient
B	bandwidth
f_{3dB}	3 dB bandwidth
η	coupling efficiency
η_m	mixer conversion efficiency
NEP	noise equivalent power
NEP_{th}	thermal fluctuation NEP
NEP_J	Johnson noise NEP
NEP_{photon}	photon noise NEP
NEP_{amp}	amplifier noise NEP
S	responsivity
I_c	superconducting critical current
T_c	superconducting critical temperature
T_{bath}	bath (substrate) temperature
T_e	electron system temperature
LO	local oscillator
RF	radio frequency
IF	intermediate frequency
ZBA	zero bias anomaly

SPP	surface polar phonon
SWNT	single-walled carbon nanotube
δE	energy resolution
rms	root mean square
FWHM	full-width at half-maximum
FTS	Fourier-transform spectrometer/spectroscopy

Chapter 1

Introduction to Bolometers

1.1 Overview of this dissertation

In the present chapter, we introduce the concept of the bolometer and provide a brief historical context, with an emphasis on the superconducting bolometer and its use as a detector of infrared signals. We also develop a general theoretical description of bolometer performance in order to understand the key figures of merit, including the speed, sensitivity, and dynamic range. More specific treatments of these figures of merit will be discussed in the context of particular devices in subsequent chapters.

In chapter 2, we describe microwave and terahertz (THz) frequency characterizations of superconducting niobium bolometers. We have developed these devices for applications in time-resolved THz spectroscopy. These devices are intended for so-called intermediate time resolution measurements, covering nanosecond to microsecond timescales, where an optical delay line becomes impractically long but a conventional bolometer is too slow. We describe the development of a broadband THz

spectrometer and its use to characterize these devices at THz frequencies, and we discuss optimization of the planar antenna geometry used for coupling of the incident THz signal. Finally, we describe an initial demonstration of this device in a time-resolved THz spectroscopy experiment.

In chapter 3, we describe a new experimental technique in which a fast microwave pulse is used to simulate a single photon of higher frequency. We have used this technique to characterize a bolometric calorimeter consisting of a superconducting titanium nanobridge with higher gap superconducting niobium contacts. This device has been developed with the goal of achieving energy-resolved THz single-photon detection. In this chapter, we consider in detail the theoretical energy resolution of a bolometric calorimeter with electrothermal feedback.

Finally, in chapter 4, we discuss how the experimental techniques developed to characterize superconducting bolometric detectors can also be used to study the physics of a different system, the single-walled carbon nanotube. Measurements of the bolometric response enable us to study the inelastic scattering processes in the nanotube. In particular, we are able to determine the thermal conductance for cooling of the nanotube electron system as a function of both the temperature of the electron system and the nanotube length. Using this thermal conductance, we are able to clearly distinguish between the bolometric (thermal) and non-thermal high frequency response.

1.2 A brief history of the bolometer

A bolometer measures the power in an electromagnetic signal by using the signal to heat an element with a temperature-dependent resistance. The bolometer was invented

around 1880 by Samuel Pierpont Langley, a distinguished American astronomer and physicist, as well as an early pioneer of aviation (Langley 1881, Loettgers 2003). The term bolometer derives from the Greek *bole*, meaning ray. The first bolometer focused light onto a thin strip of iron and used a Wheatstone bridge to record changes in the resistance of the iron strip. Combining the device with a prism, Langley measured the power spectrum from the sun as well as other sources of light. It is fitting that Langley was particularly interested in "invisible heat spectra," or infrared radiation, as the bolometer has been, and remains, a key tool for infrared spectroscopy.

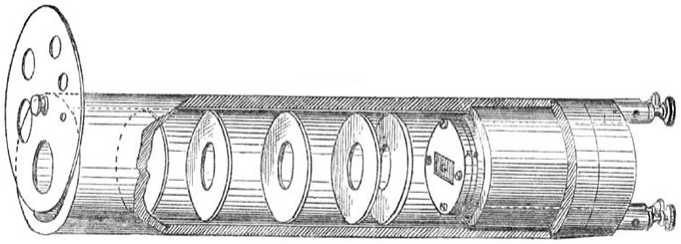

Figure 1.1. Sketch of the first bolometer by S. P. Langley, from (Langley 1881).

The first bolometers used metal films, but a desire for increased sensitivity led scientists to cool bolometers to cryogenic temperatures, where metals are no longer useful bolometric elements. These cryogenically-cooled detectors used semiconductors or superconductors. We will focus here on the superconducting bolometer, as it is the primary subject of this work. The first superconducting bolometer was made at Johns Hopkins University in 1942. A blackened aluminum sheet was used as an infrared absorber, and a tantalum wire held on its superconducting transition at 3.2 K was used as a thermometer (Andrews 1942).

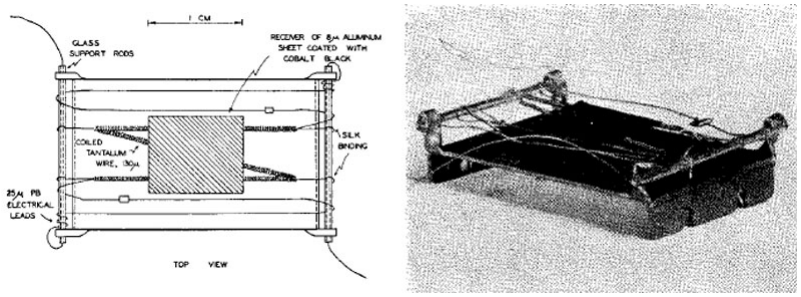

Figure 1.2. The first superconducting bolometer, from (Andrews 1942). The device used blacked aluminum as an infrared absorber and a superconducting tantalum wire as a thermometer.

The modern superconducting bolometer arguably began with the work of Clarke and colleagues at the University of California at Berkeley on the composite aluminum bolometer in 1977. This device consisted of a 135 μm thick, 4 x 4 mm sapphire substrate on which was deposited a superconducting aluminum film, which served as the bolometric thermometer, and a bismuth film, which served as an efficient absorber of far-infrared radiation. The device was thermally isolated from the environment by suspending it with indium-coated nylon thread. This device achieved an impressive noise equivalent power (NEP, discussed in section 1.4.2) of approximately 10^{-15} W/(Hz)$^{1/2}$ at an operating temperature of 1.27 K. This means that the device could detect a femtowatt signal with a signal-to-noise ratio of 1 in approximately 1 second of averaging.

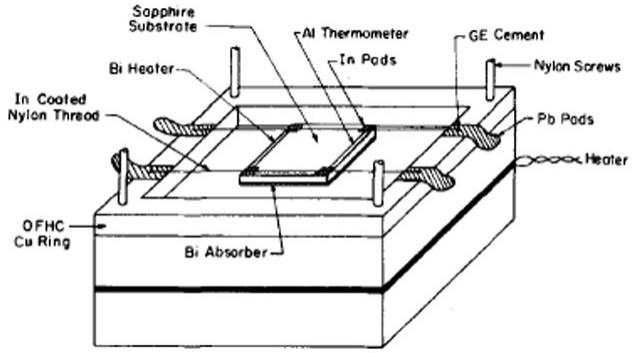

Figure 1.3. The composite aluminum superconducting bolometer developed at Berkeley, from (Clarke 1977).

Since the development of this device, which was carefully assembled by hand, advances in bolometer technology have been closely tied with the development of microfabrication facilities in academic and industrial research labs. Microfabrication – and, more recently, nanofabrication – allows the active device volume to be significantly reduced, which increases the sensitivity. Perhaps just as importantly, at least from an applications standpoint, it allows the simultaneous fabrication of large numbers of nearly identical devices.

Rutledge and colleagues pioneered the development of antenna-coupled bolometers for far-infrared detection. They used microfabrication to make a bolometer that was significantly smaller than a wavelength, and simultaneously fabricated a planar antenna geometry for efficient coupling of the incident signal (Hwang 1979). This technique was key to achieving new levels of sensitivity in far-infrared spectroscopy. Rutledge also developed the technique of through-substrate coupling for antenna-coupled bolometers (Rutledge 1983), which exploits the fact that an antenna at an air-dielectric interface couples preferentially through the higher dielectric medium.

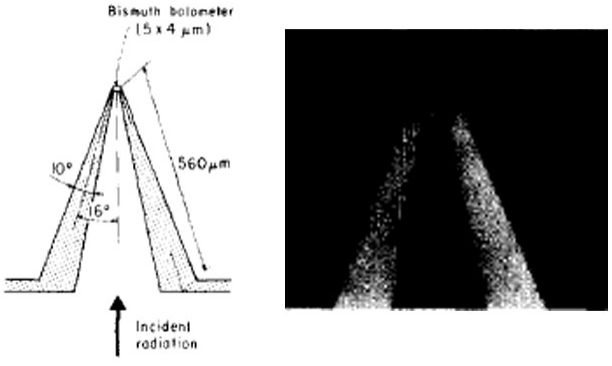

Figure 1.4. The first microfabricated antenna-coupled bolometer, from (Hwang 1979).

Another important achievement was the appreciation of electrothermal feedback – the effect of the electrical readout on the heating – which can significantly speed up the response time and also improve the device sensitivity (Irwin 1995, Lee 1996). Superconducting bolometers using a low-impedance SQUID readout with strong negative electrothermal feedback are now routinely used for sensitive detection from the infrared to x-rays (Irwin 2005).

The 1990s also saw extensive exploration of new materials and device geometries, combined with a more detailed understanding of device performance (Karasik 1996, Floet 1999, Kollberg 2006). New geometries included devices that exploited higher gap superconducting contacts to confine hot electrons in order to maximize the sensitivity (Nahum 1993), as well as the use of devices that used cooling via the outdiffusion of hot electrons into the contacts to significantly speed up the response time (Prober 1993).

Since their discovery in 1989, high-temperature superconductors have received considerable attention as bolometric materials (Richards 1989, Richards 1994). Higher operating temperatures are convenient, but the resulting decrease in sensitivity has prevented these materials from supplanting low temperature superconductors as the material of choice for sensitive superconducting bolometers. This remains, however, an area of active research.

The past decade has been marked by a shift toward applications, which in large part means the development of multi-pixel arrays. There has been extensive research on multiplexed readouts for large-scale bolometer arrays (Chervenak 1999, Irwin 2004, Richards 2004, Mazin 2006), leading to the first implementation of a multiplexed

superconducting bolometer array for astronomical observation (Benford 2002). Another application example is the recent development of far-infrared superconducting bolometer arrays for passive sensing at ambient temperatures, which can be used for concealed weapon detection (Luukanen 2008). This application exploits the ability of far-infrared signals to pass through fabric.

1.3 Nomenclature

In the literature on superconducting bolometers, a variety of names are applied to these devices. For the sake of clarity, we will briefly review the commonly used terms. Any device that fits the description given in the first sentence of the previous section is a bolometer. A composite bolometer uses separate absorber and bolometric elements. A monolithic bolometer combines these two functions in a single element.

The term hot-electron bolometer (HEB) refers to a device in which the electron system is heated relative to the lattice (phonon) temperature. At room temperature, the electron and phonon systems in a metal are strongly coupled. At cryogenic temperatures, these systems are less strongly coupled, and it becomes possible to drive the electrons significantly out of thermal equilibrium with the phonons (Wellstood 1994). For very thin films on insulating substrates, the phonon system in the film and the phonon system in the substrate are well coupled, and the relevant thermal conductance describing the cooling of the electron system in the film is the electron-phonon thermal conductance. This is the case for the superconducting bolometer devices discussed in this dissertation.

The bolometer can be operated as either a direct detector or a heterodyne mixer. A direct detector, sometimes called an incoherent detector, measures the total absorbed

power in the device input bandwidth. It can be combined with an external frequency selective element such as a prism, a diffraction grating, or a resonant circuit to achieve spectral resolution. When very high spectral resolution is required, the bolometer can be operated as a heterodyne mixer. This mode of operation exploits the thermal nonlinearity of the bolometer to take inputs at two high frequencies and produce an output at their difference frequency. The inputs consist of a known signal, called the local oscillator or LO, and an unknown signal of interest, called the RF. If we couple to the bolometer the high frequency signals $V_{RF}cos(\omega_{RF}t)$ and $V_{LO}cos(\omega_{LO}t)$, with $\omega_{RF} \approx \omega_{LO}$, the resulting time-dependent resistance $R(t)$ is given by

$$\begin{aligned} R(t) \propto T(t) \propto P_{in}(t) &= \left[V_{RF}\cos(\omega_{RF}t) + V_{LO}\cos(\omega_{LO}t)\right]^2 / R \\ &= V_{RF}V_{LO}\cos\left(\left|\omega_{RF} - \omega_{LO}\right|t\right)/R + \text{higher frequency terms} \end{aligned} \quad . \qquad (1.1)$$

From the trigonometric product identity, we see that the resistance oscillates at the intermediate frequency, or IF, $\omega_{IF} = |\omega_{RF}-\omega_{LO}|$. It will also oscillate at higher frequencies, provided that the thermal response of the device is fast enough to follow these higher frequencies. The IF signal is a frequency down-converted version of the RF signal, with both amplitude and phase information preserved. Spectral resolving can then be accomplished with high resolution at the IF.

While a bolometer measures power, a detector that measures energy is known as a calorimeter. In practice, the same device can often perform both functions. To avoid having to change names depending on whether one is detecting power or energy, the term transition edge sensor (TES) is sometimes used to describe a detector that is based on the heating of an element that is biased on its superconducting transition. Detectors operated in calorimetric mode will be discussed in detail in chapter 3.

1.4 Bolometer theory

Key figures of merit for a bolometric detector include the responsivity, the speed, the sensitivity, and the dynamic range. Using a uniform temperature approximation, we will derive general expressions for these figures of merit. The focus of this section will be to illustrate the relevant physical parameters in order to understand the physics of bolometric devices. More specific theoretical treatments will be discussed in the context of particular devices in subsequent chapters.

1.4.1 Responsivity and time constant

For small signal inputs, the bolometer is characterized by a temperature-dependent resistance $R(T) = R_0 + (dR/dT)\delta T$; a heat capacity $C = dE/dT$, E being the internal energy; as well as a thermal conductance $G = dP/dT$, with P the power flow from the device to the environment. This is seen conceptually in figure 1.5. In a hot electron device, C and T refer to the electron system, and G is the thermal conductance for energy to leave the electron system.

We assume that we couple some power to the bolometer, and this power heats up the active element of our detector. For the sake of simplicity, we will consider here the case of a uniform temperature. If we assume small heating such that we can linearize the temperature-dependence of the thermal conductance, then the heat loss of our device following an excitation is described by the differential equation

$$C\frac{dT}{dt} = -GT \tag{1.2}$$

with the solution

$$\delta T = T_1 e^{-t/\tau_0} \tag{1.3}$$

where T_1 is the temperature offset and the time constant for returning to equilibrium is $\tau_0 = C/G$. This time constant is commonly referred to as the intrinsic time constant, for reasons that will be seen shortly.

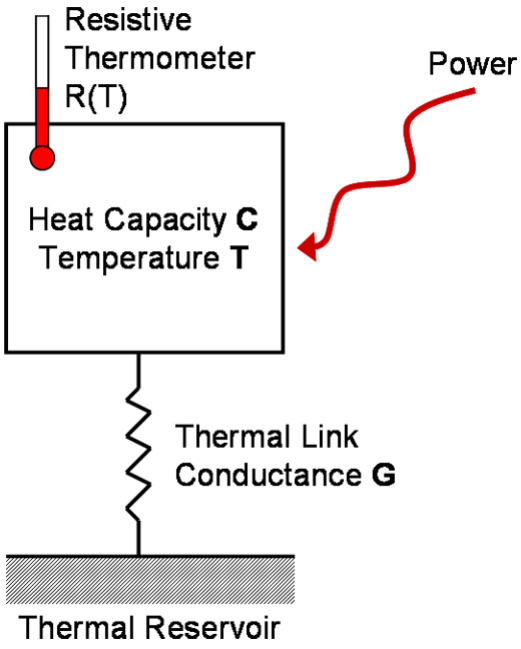

Figure 1.5. Conceptual schematic of a bolometer.

A change in temperature will correspond to a change in resistance $\delta R(t) = \delta T(t)[dR/dT]$. We now consider applying a dc current I to the bolometer in order to convert the change in resistance to a change in voltage. We define the responsivity of the bolometer as the change in voltage divided by the change in power coupled to the device, in units of V/W. We assume that we couple to the device some input power $P_{signal} = P_0 + P_1 e^{i\omega t}$. The resulting device temperature will be $T = T_0 + T_1 e^{i\omega t}$. We must also account for the Joule power from the bias current, $P_{bias} = I^2 R(T) = I^2[R(T_0) + \{dR/dT\}T_1 e^{i\omega t}]$. The

output power is $P_{out} = G[T - T_{bath}]$, where T_{bath} is the temperature of the environment. By conservation of energy, we have

$$P_{signal} + P_{bias} = P_{out} + C\frac{dT}{dt}. \tag{1.4}$$

Using the above relations, we can rewrite equation (1.4) as

$$P_0 + P_1 e^{i\omega t} + I^2[R(T_0) + \frac{dR}{dT}T_1 e^{i\omega t}] = G(T_0 - T_{bath}) + GT_1 e^{i\omega t} + i\omega C T_1 e^{i\omega t}. \tag{1.5}$$

Equating the time-dependent terms, we have

$$\frac{P_1}{T_1} = G + i\omega C - I^2\frac{dR}{dT}. \tag{1.6}$$

The frequency-dependent responsivity $S(\omega)$ is defined as the ratio of the output voltage change V_1 to the signal power P_1, where $V_1 = I\,[dR/dT]\,T_1$. Combining this with equation (1.6), we can write

$$S(\omega) = \frac{I\frac{dR}{dT}}{G + i\omega C - I^2\frac{dR}{dT}} \tag{1.7}$$

Note that if we take the bias current to zero, this becomes

$$S_{I\to 0}(\omega) = \frac{\frac{I}{G}\frac{dR}{dT}}{1 + i\omega\tau_0} \tag{1.8}$$

with $\tau_0 = C/G$. We can define an effective thermal conductance $G_{eff} = G - I^2[dR/dT]$ and an effective time constant $\tau_{eff} = C/G_{eff}$ such that equation (1.7) has the same form as equation (1.8),

$$S(\omega) = \frac{\frac{I}{G_{eff}}\frac{dR}{dT}}{1 + i\omega\tau_{eff}}. \tag{1.9}$$

We see that the effect of the bias current is to modify the time constant and the responsivity, an effect known as electrothermal feedback. For a device with a positive *dR/dT*, as is the case for a superconducting bolometer, the effect of a current bias is to decrease the effective thermal conductance and hence increase the effective time constant and the responsivity. We note that this requires a current bias at all frequencies relevant to the device response. For a negative *dR/dT*, as is typical for a semiconducting bolometer, a current bias has the opposite effect. The same procedure can be employed to solve for the responsivity in the case of a voltage bias. In this case, we find $G_{eff} = G + I^2[dR/dT]$. Hence the superconducting bolometer has a faster response (shorter τ_{eff}) for the case of a voltage bias. If the device impedance is matched to the impedance of the readout circuit, we are exactly intermediate between a current bias and a voltage bias, and there is no electrothermal feedback.

For bolometers operated as heterodyne mixers rather than direct detectors, it is customary to specify a conversion efficiency instead of a responsivity. The mixer conversion efficiency $\eta_m(\omega)$ is defined as the ratio of the IF power to the RF power, $\eta_m(\omega) = P_{IF}/P_{RF}$. We define the input as the sum of two signals $V_{LO} = V_{LO,0}\cos(\omega_{LO}t)$ and $V_{RF} = V_{RF,0}\cos(\omega_{RF}t)$. The corresponding power at frequency $\omega_{IF} = |\omega_{RF}-\omega_{LO}|$ at the detector input is $P_{IF,in} = V_{LO,0}V_{RF,0}\cos(\omega_{IF}t)/R$. The output voltage at frequency ω_{IF} is given by $V_{IF} = S(\omega)P_{IF,in}$, with $S(\omega)$ the responsivity defined in equation (1.9). The output power at ω_{IF} is $P_{IF} = (1/2)|V_{IF}|^2/R$. The input power at ω_{RF} is $P_{RF} = (1/2)|V_{RF}|^2/R$. Taking

the ratio of the time-average values of P_{IF} to P_{RF}, we get

$$\eta_m(\omega) = \frac{|S(\omega)|^2 P_{LO,0}}{2R} = \frac{I^2 P_{LO,0} \left[\frac{dR}{dT}\right]^2}{2RG_{eff}{}^2 \left[1+\left\{\omega\tau_{eff}\right\}^2\right]}. \quad (1.10)$$

We note that $\eta_m(\omega)$ is a Lorentzian function that decreases to half its zero-frequency value at an angular frequency $\omega = 2\pi f = 1/\tau_{eff}$. This frequency is commonly referred to as the 3 dB bandwidth, or f_{3dB}, as 3 dB is approximately one half in linear units. The 3 dB bandwidth is a measure of the frequency window around the LO frequency that the device can detect with good efficiency.

1.4.2 Sensitivity

A standard for defining the sensitivity of a direct detector is the noise equivalent power (*NEP*), defined as the signal power required to achieve a signal-to-noise ratio of one per unit output bandwidth, in units of W/(Hz)$^{1/2}$. The measured NEP will have contributions from source noise, from intrinsic device noise, and from the noise of the readout electronics.

In a bolometric detector, the intrinsic device noise has contributions from current fluctuations (NEP_I) and from thermal fluctuations (NEP_{th}). The source noise is due to photon shot noise (NEP_{photon}). In a well-designed experiment, the noise from the readout electronics is dominated by the input noise of the first stage amplifier (NEP_{amp}). These noise sources are assumed to be uncorrelated and hence the noise amplitudes add in quadrature. Thus the total *NEP* is given by

$$NEP = \sqrt{NEP_I{}^2 + NEP_{th}{}^2 + NEP_{photon}{}^2 + NEP_{amp}{}^2}\ . \quad (1.11)$$

1.4.2a Current fluctuation noise

The statistics of the current passing through a conductor are a source of noise. For a voltage-biased tunnel junction with resistance R, it was shown by Rogovin and Scalapino (1974) that the current noise spectral density is given by

$$S_I = (2eV/R)\coth(eV/2k_BT) \tag{1.12}$$

in units of A^2/Hz. For a detailed derivation of this result, the reader is referred to Spietz (2006). If we assume a current bias instead of a voltage bias, we have instead the voltage noise spectral density $S_V = S_I R^2$. In the limit $eV << k_BT$, we obtain Johnson noise, $S_I = 4k_BT/R$, a general result that applies to any conductor with resistance R at a temperature T. In the limit $eV >> k_BT$, we obtain the shot noise result from Poisson statistics, $S_I = 2eI$. For a diffusive wire of length L, it has been shown (Nagaev 1995, Steinbach 1996) that for $L_{e\text{-}e} < L < L_{e\text{-}ph}$, where $L_{e\text{-}e}$ is the electron-electron inelastic scattering length and $L_{e\text{-}ph}$ is the electron-phonon inelastic scattering length, the shot noise deviates from the Poisson result by a factor of $\sqrt{3}/4$. For $L >> L_{e\text{-}ph}$, the shot noise is negligible as a result of electron-phonon inelastic scattering. This latter situation is the case for most of the devices measured in this work.

1.4.2b Thermal fluctuation noise

The temperature of a device fluctuates due to the random exchange of energy between the device and its environment. For a device in thermal equilibrium with its environment, we assume a Gaussian distribution for the fluctuation probability, and the resulting thermodynamic mean square temperature fluctuations can be shown to be (see e.g. Landau and Lifshitz (1980), chapter 12)

$$\left\langle \delta T^2 \right\rangle = \frac{k_B T^2}{C} \tag{1.13}$$

where <…> denotes a time average.

The mean square temperature fluctuations can be related to the mean square power fluctuations through the thermal conductance, $<\delta P^2> = G^2 <\delta T^2>$, and hence $<\delta P^2> = k_B T^2 G/\tau$, with $\tau = \tau_0 = C/G$ the intrinsic thermal time constant. The time constant is related to the bandwidth $B = 4/\tau$,[1] and the mean square power fluctuations are $<\delta P^2> = 4k_B T^2 GB$. We can account for electrothermal feedback as we did in section 1.4.1, by replacing G with $G_{eff} = G \pm I^2[dR/dT]$, where, as before, addition corresponds to the case of a voltage bias and subtraction to the case of a current bias.

Fluctuations in the output voltage V are related to the mean square power fluctuations through the responsivity, $<\delta V^2> = S^2 <\delta P^2>$. We can then express this as a noise temperature $T_{th} = <\delta V^2>/Rk_B B$, or, with electrothermal feedback,

$$T_{th} = \frac{4S^2 T^2 G_{eff}}{R}, \tag{1.14}$$

which, expressed as a thermal fluctuation NEP_{th} (see section 1.4.2e), is

$$NEP_{th}^2 = 4k_B T^2 G. \tag{1.15}$$

[1] The factor of 4 can be understood as follows. The device responsivity is described by a Lorentzian function. If we integrate a Lorentzian from $\omega = -\infty$ to $+\infty$, we obtain 4 times the value that we would get from integrating from 0 to $1/\tau$. Positive and negative frequencies correspond to the absorption and emission, respectively, of phonons, photons, or whatever is contributing to the thermal conductance. In the experiments described in this work, the photon thermal conductance is always negligible compared to the phonon thermal conductance. However, if one is working at ultra-low temperatures (< 100 mK), this may no longer be the case.

Note that while T_{th} is modified by electrothermal feedback, NEP_{th} is not. This is because thermal fluctuation noise and the device responsivity arise from the same physical mechanism, and hence both are affected in the same way by electrothermal feedback.

Equation (1.15) is frequently quoted in the bolometer literature. However, this result was derived in the isothermal regime, in which we assume that the device and the environment are at the same average temperature. If we relax the isothermal assumption and allow for the device to be at a different temperature from the environment, we must modify equation (1.15). Physically, thermal fluctuation noise arises from the random exchange of energy between a device and its environment, in our case in the form of phonons. A factor of 2 in equation (1.15) arises from considering both absorption and emission. The emission of phonons will depend on the device temperature, but the absorption of phonons will depend on the temperature of the environment. As an example, consider a zero temperature environment, in which case there are no phonons emitted by the environment. In this case, the factor of 4 in equation (1.15) should be replaced by a 2.

The non-isothermal case of a device coupled to the environment through a diffusive phonon link has been treated by Mather (1982). To the best of our knowledge, the case of a device with a ballistic phonon link to its environment is lacking a rigorous theoretical treatment. This is the case for all of the devices studied in this work, which exchange phonons directly with the insulating substrate on which they sit, and indeed for the majority of bolometers. In the absence of a rigorous theory, we approximate equation (1.15) in the non-isothermal regime as

$$NEP_{th}^{\ 2} = 2k_B\left[G(T)T^2 + G(T_{bath})T_{bath}^{\ 2}\right] \tag{1.16}$$

where T is the device temperature and T_{bath} is the temperature of the environment. Noise due to superconducting effects at temperatures near T_c is typically less than the thermal fluctuation noise, as evidenced by our experimental results, discussed later.

1.4.2c Photon shot noise

The arrival statistics of photons is another source of noise, known as photon shot noise. Here we consider a blackbody photon source and a single mode detector, such as a device at the end of a coaxial cable or at the feed of a planar antenna. The case of a multi-mode detector is treated in Richards (1994). The mean square energy fluctuation in the source is given by

$$<(\delta E)^2> = (hf)^2 <(\Delta n)^2>. \tag{1.17}$$

The average variance of the photon number per mode for a blackbody is

$$<(\Delta n)^2> = n + n^2 \tag{1.18}$$

where the photon density per mode is given by the Planck distribution, $n = (e^{hf/k_BT} - 1)^{-1}$. For low mode occupancy ($n << 1$), the average variance is n and we recover Poisson statistics. For high mode occupancy ($n >> 1$), the average variance is n^2 due to photon bunching.

We then associate the *NEP* with the mean square power fluctuations per unit bandwidth

$$(NEP_{photon})^2 = \frac{<(\delta P)^2>}{B} = 2\int_{f_1}^{f_2} \eta (hf)^2 \left[(e^{hf/k_BT} - 1)^{-1} + (e^{hf/k_BT} - 1)^{-2} \right] df \tag{1.19}$$

where the factor of 2 is because a one second average corresponds to a bandwidth of ½ Hz (Richards 1994). The coupling efficiency η appears because only the coupled power

contributes to NEP_{photon}. In the Rayleigh-Jeans limit ($hf << k_BT$ and hence $n >> 1$), equation (1.19) simplifies to

$$NEP_{photon} = \eta k_B T \sqrt{2(f_2 - f_1)}\,. \tag{1.20}$$

1.4.2d Amplifier noise

Amplifiers have a noise temperature that, in general, must be determined experimentally. The standard experimental technique for determining the noise temperature of a microwave frequency amplifier is the Y-factor technique, in which the Johnson noise of a matched load at two different temperatures is used as a known source of noise. Typical microwave amplifier noise temperatures range from as low as a few Kelvin for the best cryogenic semiconductor amplifiers (e.g. (Weinreb 2009)) to hundreds of Kelvin for more conventional room temperature amplifiers.

1.4.2e Converting between different noise quantities

Noise quantities are alternatively expressed as a noise temperature (T_N), a current noise spectral density (S_I), and a noise equivalent power (*NEP*). It is important to be able to convert between these different but related measures. Note that noise temperature and noise spectral density are measures of noise, while the *NEP* is a measure of sensitivity.

The noise temperature T_N is defined as the physical temperature of a resistor that would couple an equivalent Johnson noise power into a matched load, thus

$$T_N = P_N / [k_B B] = S_I R / [4k_B] \tag{1.21}$$

where P_N is the noise power measured in a matched load and B is the measurement bandwidth. The noise temperature is related to the *NEP* by

$$NEP = \sqrt{k_B T_N R} \big/ S \tag{1.22}$$

where S is the responsivity.

For heterodyne mixers, the sensitivity is commonly expressed as a mixer noise temperature rather than an *NEP*. The mixer noise temperature is defined as the power per unit frequency at the RF required to give unity signal-to-noise at the IF, divided by k_B. If one considers only RF input in a single side-band, one obtains the single-sideband mixer noise temperature, $T_{mix,SSB} = T_N/\eta_m$, where T_N is the noise temperature at the mixer output and η_m is the mixer conversion efficiency. The double-sideband mixer noise temperature considers RF input from both the upper and lower sidebands, and hence is smaller than the single-sideband mixer noise temperature by a factor of two. This assumes that the system responds symmetrically to both sidebands, which is true for most detectors.

For direct detectors, one must be careful to distinguish between the electrical *NEP* and the optical *NEP*. The electrical *NEP* is the signal power *absorbed in the device* required to get a signal-to-noise of one per unit output bandwidth. All previous uses of the term *NEP* in this chapter have referred to the electrical *NEP*. The optical *NEP* is the signal power *incident on the system* required to get a signal-to-noise of one per unit output bandwidth. Hence the optical *NEP* is obtained by dividing the electrical *NEP* by the system coupling efficiency η.

For a bolometric calorimeter, the sensitivity is typically expressed in terms of the energy resolution δE, which is related to the *NEP* by (Moseley 1984)

$$\delta E_{FWHM} = 2\sqrt{2\ln 2}\,\delta E_{rms} = 2\sqrt{2\ln 2}\left(\int_0^\infty \frac{4df}{NEP^2}\right)^{-1/2} \tag{1.23}$$

where FWHM denotes full-width at half-maximum and rms denotes root mean square. If we consider only the thermal fluctuation NEP_{th} of equation (1.15), equation (1.23) yields an energy resolution $\delta E_{FWHM} = 0$. This surprising result arises because the device responsivity and the thermal fluctuation noise both roll off with the same characteristic timescale, and so the signal-to-noise ratio is constant with frequency (and hence NEP_{th} is frequency-independent). In practice, as we move to higher frequency, other noise sources, such as amplifier noise and Johnson noise, will become larger than the signal and the thermal fluctuation noise. As we move beyond this crossover frequency, the integral in equation (1.23) will approach some constant value. These other noise sources, along with the finite bandwidth of our amplifier, prevent us from getting continuously better energy resolution by arbitrarily increasing the measurement bandwidth. In practice, the best energy resolution is obtained by comparing the frequency spectrum of thermal fluctuation noise with the other sources of noise and using this to determine the optimum measurement bandwidth.

1.4.3 Dynamic range

The minimum detectable signal is specified by the *NEP*. To determine the dynamic range, we must also consider the maximum detectable signal. For a superconducting bolometer, we can define the total saturation power

$$P_{sat} = \int_{T_{bath}}^{T_c} G(T')dT' \tag{1.24}$$

where P_{sat} includes the power from both the input signal and the dc bias, and T_c is the superconducting transition temperature. In practice, a dc bias is typically used to hold the

device on the superconducting transition, which has some finite temperature width ΔT_c. We can then estimate the size of the input signal power that will saturate the device as $P_{sat,signal} \sim G(T_c)\Delta T_c$. As the device is biased mostly in the non-superconducting state, the actual saturation power is likely somewhat smaller than (but still order-of-magnitude consistent with) the value estimated in this way.

Chapter 2

Antenna-Coupled Niobium Bolometers for Time-Resolved THz Spectroscopy

2.1 Introduction

Terahertz (THz), or far-infrared (FIR), spectroscopy is an important tool for molecular characterization, as this spectral range corresponds to vibrational and torsional modes in many molecules, as well as rotational modes in many light molecules (Blake 2001). Additionally, FIR spectroscopy is a sensitive probe of solid state materials, as it can be used to measure lattice modes and the motion of mobile charges (Schmuttenmaer 2004). It is especially useful as a non-contact probe for studies of nanoscale systems, where attaching electrical leads is difficult or causes perturbations to the system. Biological systems are also amenable to FIR studies, from measuring the low frequency motion of proteins to imaging plant and animal material (Sherwin 2004).

The two standard techniques for these types of studies are THz time-domain spectroscopy (TDS) and FIR Fourier transform spectroscopy (FTS). TDS was developed in the late 1980s following the discovery that a coplanar stripline on a semiconducting

substrate, when excited with an ultra-fast laser pulse, will radiate into free space with a spectral output bandwidth limited by the envelope of the laser pulse and the dynamical current response of the semiconductor (Smith 1988). A similar coplanar stripline device can be used as a detector, which is synchronized with the same optical pulse used to drive the emitter (van Exter 1990). The detector measures the electric field of the transmitted pulse, preserving both amplitude and phase. This allows, for example, determination of the frequency-dependent complex index of refraction of a sample in the signal path. This technique and its variants are now utilized by many research groups and can achieve bandwidths of several THz with high signal-to-noise ratios and peak power ~ mW (Han 2001).

By using portions of the same optical pulse to excite the sample and the detector, and by varying the time delay between the excitation pulse and the pulse on the detector, one can perform time-resolved measurements of the transmitted electric field with sub-ps resolution (Beard 2002). This is a powerful tool for studying the dynamics of ultra-fast systems, such as intermolecular charge transfer and charge trapping. This technique is often referred to as time-resolved THz spectroscopy (TRTS) to distinguish it from standard THz TDS. The upper time limit of this technique is set by the length of the optical delay line, which typically corresponds to a maximum timescale of order a nanosecond. Longer delay lines are possible, but they pose a significant challenge for alignment and are rarely used.

FTS uses a blackbody source such as a mercury arc lamp or a heated filament. These sources are more broadband than the sources of TDS but have much lower peak power. The time resolution in FTS is set by the response time of the detector. The most

common detector type is the silicon (Si) bolometer, which has a thermal time constant $\tau \sim$ ms and an optical noise equivalent power (*NEP*) of 2 x 10^{-12} W/(Hz)$^{1/2}$ at 4.2 K. Faster options include the gallium doped germanium photoconductive detector ($\tau \sim$ 1 μs, *NEP* ~ 10^{-12} W/(Hz)$^{1/2}$) and the indium antimonide bolometer ($\tau \sim$ 100 ns, *NEP* ~ 10^{-12} W/(Hz)$^{1/2}$).[1] These have a more limited input bandwidth than the slower Si bolometer. All of these detectors measure power, unlike TDS, which measures electric field. They are typically large area, multi-mode detectors. Because of their slow time constant, these detectors are usually used in FTS to study samples whose properties are constant in time. An optical chopper is usually used to avoid *1/f* noise of the detector.

We have developed an antenna-coupled superconducting microbolometer that is orders of magnitude faster than conventional bolometers. This device is designed to bridge the gap in time resolution available with TRTS ($\lesssim$ ns) and conventional FTS ($\gtrsim$ μs). Our niobium (Nb) device, operating at 4.2 K, achieves greater sensitivity than any of the commercially-available semiconductor bolometers at the same operating temperature. If the Si or Ge detectors are operated at much lower temperature, their sensitivity improves significantly, but their response time becomes slower, > ms.

The antenna-coupled superconducting microbolometer has been developed extensively over the past decade as a heterodyne mixer for submillimeter wavelength astronomy (Zmuidzinas 2004). These heterodyne detectors are designed to have high sensitivity and a large intermediate frequency bandwidth, typically several GHz. We have adapted this technology to develop direct detectors for applications in laboratory-based

[1] Specifications for silicon, germanium, and indium antimonide detectors are from QMC Instruments (Cardiff, Wales). Similar detectors are also available commercially from Infrared Labs (Tucson, AZ).

THz spectroscopy of room temperature samples. These applications can make use of the high sensitivity and fast response time of the superconducting microbolometer, but they may require greater power handling than radioastronomy applications. We have fabricated devices with geometries optimized for these laboratory-based spectroscopy applications. We characterize the device performance in detail at both microwave and THz frequencies. These experiments have previously been discussed in Santavicca *et al*. (*IEEE* 2007, *Supercond. Sci. Technol.* 2007).

2.2 Device overview

Devices are fabricated from dc magnetron sputtered niobium (Nb) and thermally evaporated aluminum (Al) on high-resistivity silicon substrates using a lift-off process. The bolometric element is a 12 nm thick Nb microbridge spanning contacts that consist of a bilayer of 12 nm of Nb and 200 nm of Al. Al is used because it is a high conductivity metal (we typically operate above the superconducting critical temperature of Al, $T_{c,Al}$ = 1.2 - 2 K), and the bilayer has a sheet resistance of < 0.1 Ω/square. The bilayer forms an antenna geometry for THz coupling as well as leads for electrical (dc-GHz) coupling. The first generation of antenna-coupled devices was patterned using electron-beam lithography, and this process is described in Reese (2006). These first-generation devices were fabricated at Yale by Matthew Reese and Dr. Luigi Frunzio. They were designed with a 38 μm double-dipole antenna, as seen in figure 2.1. Subsequent devices with different planar antenna geometries were fabricated with Anthony Annunziata and Dr. Luigi Frunzio. These devices were patterned with optical lithography; the details of this process are described in appendix A.

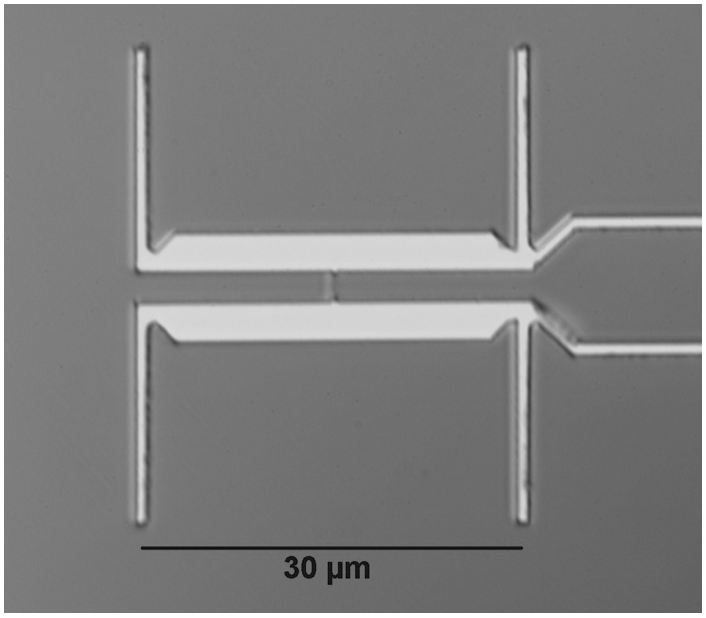

Figure 2.1. Optical image of first-generation Nb microbolometer with 38 μm double-dipole antenna. The Nb microbridge (dark gray) is oriented vertically between the U-arms of the Al antenna (light gray). Electrical leads extend to the right of the antenna.

The Nb microbridge has a superconducting critical temperature $T_c \approx 6$ K and a transition width $\Delta T_c \approx 1$ K. The first generation of Nb devices has microbridge dimensions of 2.5 μm long by 1.0 μm wide. Subsequent optically-patterned devices maintain the same aspect ratio in order to maintain the same resistance, with microbridge dimensions of 5 μm by 2 μm. A typical plot of dc resistance as a function of temperature is presented in figure 2.2. Also shown is a typical plot of dc current as a function of voltage measured at several different bath temperatures.

The thermal time constant of a Nb microbridge at $T \approx 6$ K has been shown to be equal to the electron-phonon inelastic scattering time provided that the film thickness is $\lesssim 10$ nm (Gershenzon 1990) and the length is > 2 μm (Burke 1996). For thicker films,

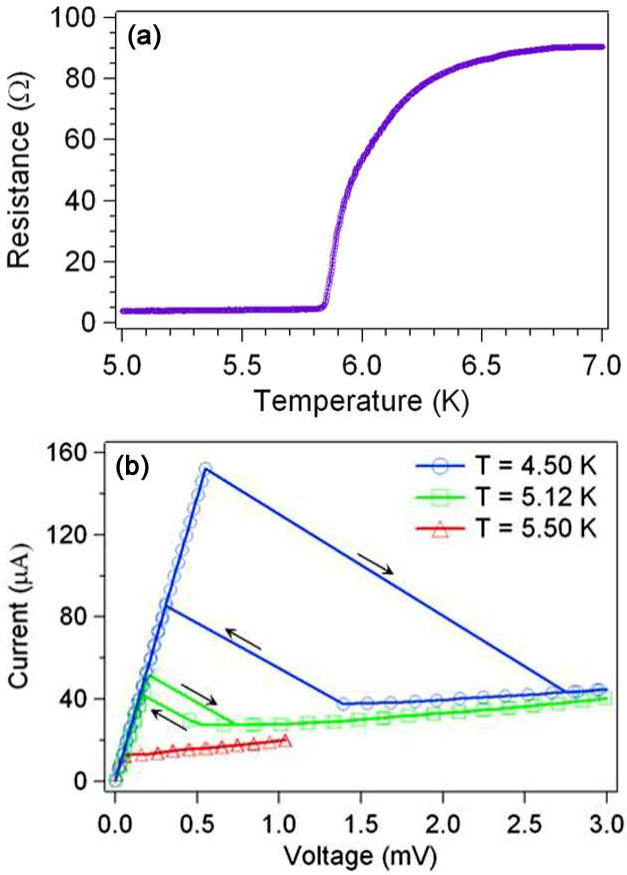

Figure 2.2. Typical dc characteristics of Nb microbolometer. (a) Resistance as a function of temperature measured with 1 μA bias current. The resistance below T_c is from the leads. (b) Current as a function of voltage at different bath temperatures, measured with a 20 Ω load line. Hysteresis due to self-heating appears at lower temperatures (Skocpol 1974), and the direction of the sweep for hysteretic curves is indicated with arrows.

the phonon interface resistance between the Nb and the substrate increases the cooling time. For shorter microbridges, the contribution to the cooling from the outdiffusion of hot electrons becomes significant (Prober 1993, Burke 1996). All of the devices studied in this chapter are in the phonon-cooled regime, in which we can safely neglect both the phonon interface resistance and the contribution of hot electron outdiffusion to the cooling.

At low temperature, the electron-phonon inelastic scattering time $\tau_{e\text{-}ph}$ has been found experimentally to be proportional to T^{-2} for thin film Nb, where T is the film temperature (Gershenzon 1990, Burke 1996). From Fermi-Dirac statistics, the electronic heat capacity C_e is proportional to T. The electron-phonon thermal conductance $G_{e\text{-}ph} = C_e/\tau_{e\text{-}ph}$ is thus proportional to T^3. $G_{e\text{-}ph}$ is also proportional to the microbridge volume V, as C_e is proportional to V and $\tau_{e\text{-}ph}$ is volume-independent.

We recall from chapter 1 that the thermal fluctuation NEP_{th} is proportional to $(T^2G)^{1/2}$, and hence for thin film Nb it is proportional to $T^{5/2}$ and $V^{1/2}$. Finally, we found that the saturation power is $\sim G\Delta T_c$, and hence is proportional to V. The volume and temperature dependencies of the detector time constant, NEP_{th}, and saturation power are summarized in table 2.1. We have assumed that the device temperature $T = T_c$, as the superconducting bolometer is always operated on its superconducting transition.

We see that there is a fundamental tradeoff between the device sensitivity and both speed and power handling. The goal of the work described in this chapter is to develop a detector with T_c and V chosen to achieve the greatest possible sensitivity while having sufficient power handling to avoid saturation when viewing a room temperature background and sufficient speed to measure at timescales as fast as ~ ns.

$NEP_{th} \propto V^{1/2}, T_c^{5/2}$
saturation power $\propto V$
time constant $\propto T_c^{-2}$

Table 2.1 Summary of the dependencies of key figures of merit for a thin film Nb bolometer on the superconducting critical temperature T_c and the microbridge volume V.

2.3 Microwave characterization

Microwave frequency device characterizations were performed in a liquid helium-4 (^{4}He) cryostat, illustrated in figure 2.3. By pumping on the liquid helium, the bath temperature can be lowered from 4.2 K to 1.5 K. The sample is located in an inner vacuum can (IVC) with a heater and thermometer, and is thermally isolated from the bath by a short (≈ 1") length of stainless steel coaxial cable. The sample temperature can be adjusted from the bath temperature to 10 K or higher. The coaxial lines from the helium bath to room temperature have stainless steel outer conductors and copper inner conductors, a compromise between low electrical loss and low heat conduction.

The high frequency input is sent into the coupled port of a cryogenic -20 dB directional coupler, which connects to the RF port of a cryogenic bias-tee (see figure 2.3). The bias-tee is mounted directly above the IVC, and the dc port of the bias-tee connects to room temperature biasing electronics via a coaxial cable with a homemade copper powder low-pass filter (Martinis 1987) to attenuate high frequency noise. The transmitted port of the directional coupler connects to a cryogenic microwave low-pass filter, which leads to a room temperature amplifier. This microwave low-pass filter is designed to have a passband that extends to ~GHz and to dissipate rather than reflect higher frequency signals (Santavicca *Meas. Sci. Technol.* 2008). This prevents signals that are in the filter stopband from saturating the amplifier chain while simultaneously preventing reflections at the coupler transmitted port from generating standing wave interference. For more on this type of filter, see appendix C. The output of the room temperature amplifier is coupled to a spectrum analyzer or a diode, depending on the measurement being performed.

The device is mounted in a homemade copper (Cu) sample holder with a coaxial SMA-to-pin adapter, as seen in the inset of figure 2.4. Inside the sample holder, the pin is soldered to a 50 Ω microstrip that has been etched from Rogers Duroid 6010 high frequency laminate. The laminate dielectric constant, $\varepsilon_{lam} = 10.2$, is close to the dielectric constant of the silicon substrate, $\varepsilon_{Si} = 11.9$, which is positioned at the end of the microstrip and secured with GE varnish. The end of the microstrip is wirebonded to the device, and the other side of the device is wirebonded to the body of the Cu sample holder, which is ground. To minimize the inductance from the wirebonds (~ 1 nH/mm), several bonds are used in parallel and the bond length is kept as short as possible.

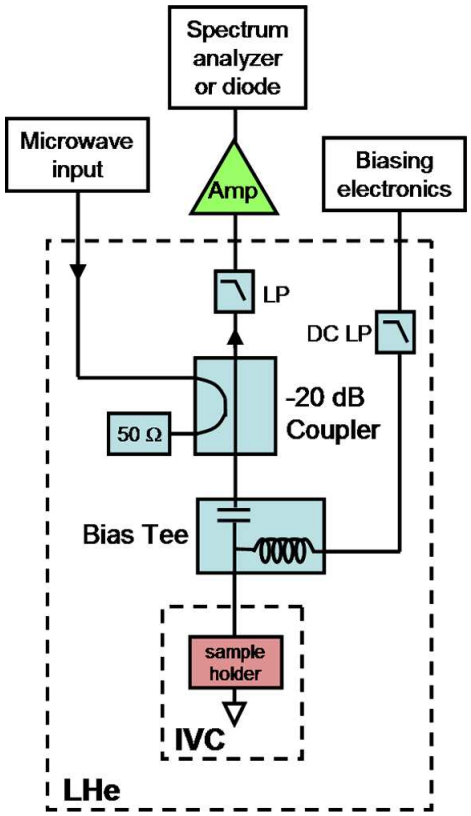

Figure 2.3. Schematic of experimental setup for microwave frequency characterization of Nb devices. LP stands for low-pass filter, and solid lines represent coaxial cables.

To test the coupling efficiency of this sample holder, we mounted a small form factor (0402) 50 Ω chip resistor in place of the sample, making electrical contact with wirebonds of similar length to those used for real samples. In figure 2.4 we plot the measured return loss – defined as $-10\log(P_{ref}/P_{inc})$, where P_{ref}/P_{inc} is the ratio of reflected to incident power – as a function of frequency from 50 MHz to 40 GHz. We see there is better than 90% coupling efficiency (return loss > 10 dB) up to approximately 20 GHz, and better than 70% coupling efficiency (return loss > 5 dB) up to 40 GHz. Some of the reflected power at higher frequencies may be due to parasitic reactance in the chip resistor rather than in the sample holder.

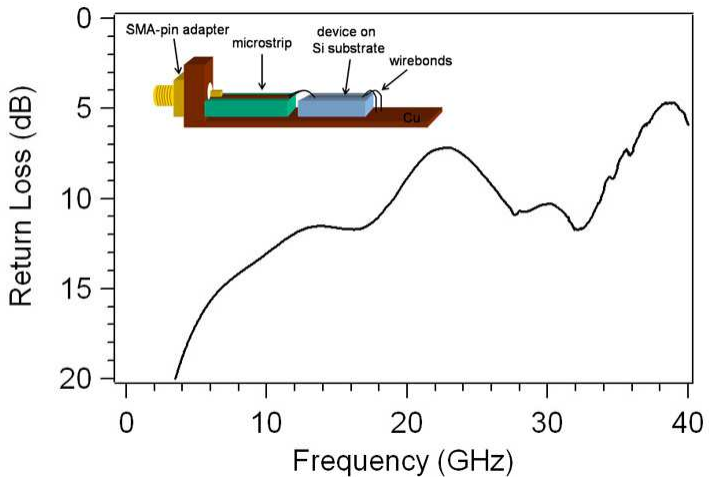

Figure 2.4. Measured return loss of 50 Ω chip resistor wirebonded in the microwave sample holder. Inset: schematic of device mounted in sample holder. Top and sides of the copper enclosure are not shown.

2.3.1 Time constant

The detector time constant was found from a heterodyne mixing measurement (Burke 1996). The sum of two high frequency signals (f_{RF} = 1.4 GHz and f_{LO} = 1.5-2.4 GHz) was coupled to the device, and the device response at the difference frequency f_{IF} =

$|f_{LO} - f_{RF}|$ was amplified (amplifier bandwidth = 0.1-8 GHz) and measured on a spectrum analyzer. The device is biased with a dc voltage bias with a load line resistance of 20 Ω, like the data in figure 2.2(b). A dc voltage bias creates a stable bias point on the superconducting transition via passive electrothermal feedback. If a fluctuation increases the device temperature and hence the resistance R, the Joule power from the bias voltage V^2/R will decrease, facilitating the return to equilibrium. The optimum dc bias point for detection is on the non-superconducting branch of the current-voltage curve, just before the device switches back to the superconducting state. To illustrate the optimum bias point, we plot in figure 2.5 the measured power at f_{IF} as a function of the bias voltage.

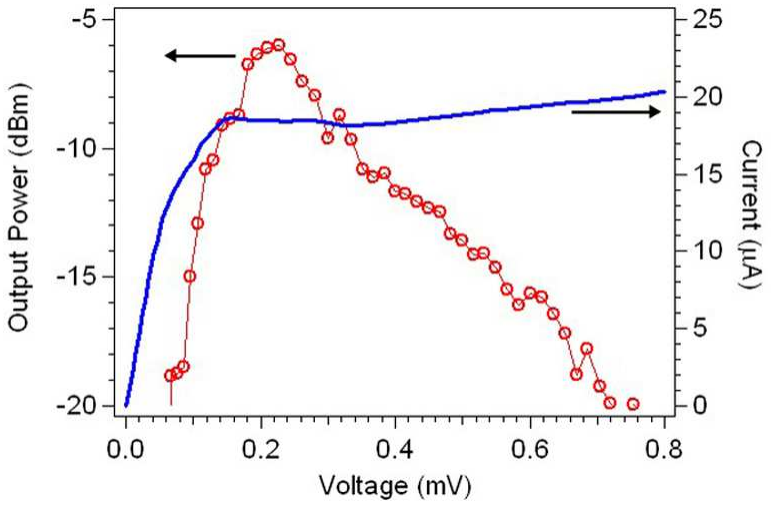

Figure 2.5. Measured intermediate frequency output power and dc current as a function of bias voltage at T_{bath} = 5.2 K.

With the device at the optimum bias point (approximately 0.2 mV at T_{bath} = 5.2 K), we measure the device response as a function of f_{IF}. The measured output power is converted to a conversion efficiency, which is plotted in figure 2.6 using a log scale. The

data are fit to the expression from chapter 1 for the frequency-dependent conversion efficiency $\eta_m(f) = P_{IF}/P_{RF}$,

$$\eta_m(f) = \frac{\eta_m(0)}{1+(2\pi f \tau)^2}. \qquad (2.1)$$

The frequency at which $\eta_m(f) = \eta_m(0)/2$, commonly called the 3 dB point, is $f_{3dB} = 1/(2\pi\tau) = 240$ MHz. This corresponds to a time constant $\tau = 0.7$ ns. This is consistent with previous measurements of the electron-phonon inelastic scattering time in thin Nb films (Gershenzon 1990, Burke 1996). The device and the load (amplifier) impedance at f_{IF} are both $\approx 50\ \Omega$, so the measured time constant should not be significantly affected by electrothermal feedback.

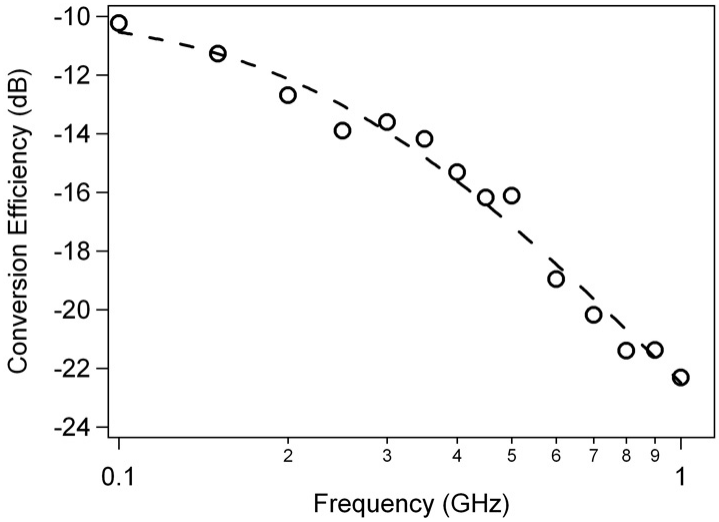

Figure 2.6. Measured conversion efficiency as a function of the intermediate frequency. Dashed line is a fit to equation (2.1) to determine $f_{3dB} = 240$ MHz and hence $\tau = 0.7$ ns.

2.3.2 Responsivity

Next we examine the dependence of the device response on the signal power and the bath temperature. Because we are interested in the device performance when operated

as a direct detector rather than as a heterodyne mixer, we simulate direct detection by using equal amplitudes for the signals at f_{RF} and f_{LO}.[2] This produces 100% amplitude modulation at f_{IF}, which is similar to a single high frequency source whose amplitude is modulated sinusoidally. The responsivity *S(f)* is then the ratio of the measured IF voltage to the input power. We measure at f_{IF} = 80 MHz, where $S(f) \approx S(0)$.[3] In figure 2.7 we plot the measured responsivity as a function of modulated signal power for bath temperatures of 3.2 K, 4.2 K, and 5.2 K. This device has T_c = 5.8 K. We note that we have defined the responsivity here in terms of the voltage coupled to a 50 Ω amplifier. For our case, with approximately matched device and amplifier impedances, this is a factor of 2 smaller than the responsivity defined in chapter 1.

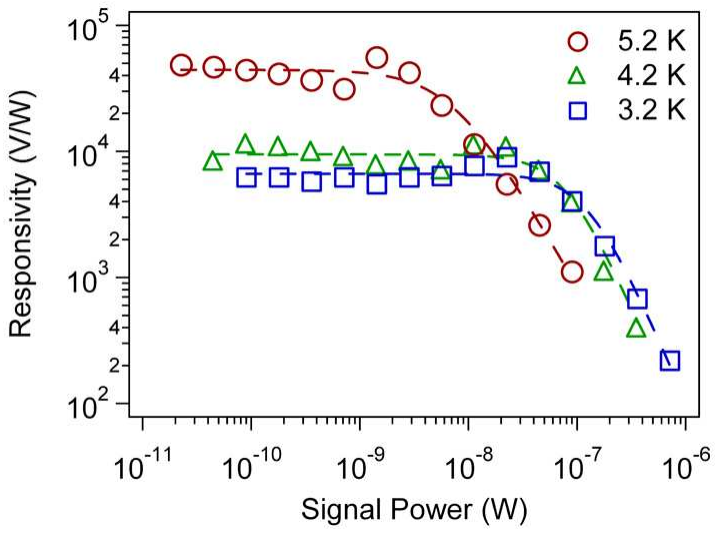

Figure 2.7. Measured responsivity as a function of signal power at different bath temperatures.

[2] For heterodyne mixers, the amplitude at f_{LO} is typically much greater than the amplitude at f_{RF}, as this maximizes the conversion efficiency when detecting weak RF signals.
[3] This frequency is chosen in part because it matches the repetition rate of a Ti:Sapphire laser used for THz generation in the Schmuttenmaer lab (Yale chemistry).

We see that the largest responsivity is obtained for higher bath temperatures, while the largest saturation power is obtained for lower bath temperatures. This is in contrast to similar devices operated as conventional heterodyne mixers, for which a lower bath temperature permits a greater LO power, which increases the mixer conversion efficiency. We define the saturation power P_{sat} as the signal power at which the responsivity decreases by a factor of 2. The dashed lines in figure 2.7 are fits to the empirical function $S(P_{signal}) = S_0/[1+(P_{signal}/P_{sat})^{\alpha}]$, where $\alpha = 2.0$ at 3.2 K and 4.2 K and $\alpha = 1.5$ at 5.2 K. Above $T_{bath} = 5.2$ K, the saturation power quickly approaches zero.

2.3.3 Thermal conductance

The thermal conductance of the electron system in the microbridge is determined using Johnson noise thermometry. As we saw in chapter 1, the noise power emitted by a resistor at temperature T into a matched resistive load is $k_B TB$, where B is the coupling bandwidth. With the device above T_c, we heat the device with a dc bias current, and we measure the average temperature inferred from the emitted Johnson noise power as a function of the dc Joule power P_{bias}. The noise is measured with a 50 Ω amplifier at a frequency of approximately 1 GHz with a 50 MHz bandwidth on the diode input. The results are plotted in figure 2.8. The device is longer than the electron-phonon coupling length (Burke 1996), so the contribution from shot noise is negligible (Steinbach 1996). We fit the measured data to the function

$$P_{bias} = A\left(T^n - {T_{bath}}^n\right)V \qquad (2.2)$$

where A and n are constants and V is the microbridge volume. From the fit, we determine $n = 4$ and $A = 8.2 \times 10^9$ WK^{-4}m^{-3}. These values are consistent with previous measurements of thin Nb films (Burke 1997). The thermal conductance is then $G_{e\text{-}ph} = dP_{bias}/dT = AVnT^{n-1}$. For the microbridge geometry in figure 2.1, this is $G_{e\text{-}ph} = (9.8 \times 10^{-10}\ T^3)$ W/K, or (2.1×10^{-7}) W/K at $T = T_c = 6$ K.

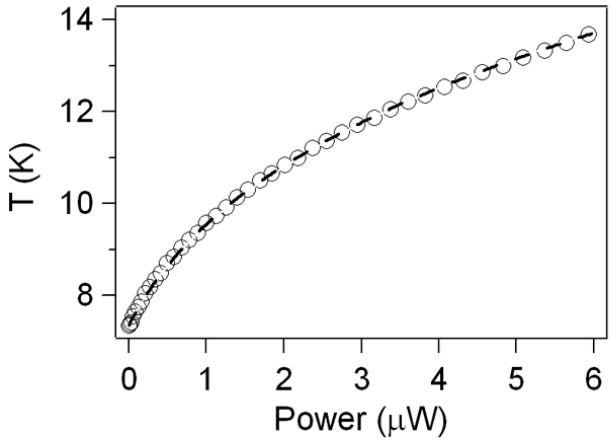

Figure 2.8. Temperature inferred from measured Johnson noise as a function of dc Joule power. Dashed line is a fit to equation (2.2).

2.3.4 Noise

The thermal fluctuation NEP_{th} is approximately $(4k_BT^2G_{e\text{-}ph})^{1/2}$, were we use equation (1.15) instead of (1.16) because $T_{bath} = 5.2$ K is close to $T_c = 5.8$ K. Using the experimental value for $G_{e\text{-}ph}$ from section 2.3.3, we find $NEP_{th} = 2.0 \times 10^{-14}$ W/Hz$^{1/2}$. The photon shot noise $NEP_{ph} = \eta k_BT(2B)^{1/2}$, with B the input bandwidth and η the input coupling efficiency. If we take $\eta = 0.2$, $T = 300$ K, and $B = 1$ THz, then $NEP_{ph} = 1.2 \times 10^{-15}$ W/Hz$^{1/2}$. Finally, the Johnson noise $NEP_J = (k_BTR)^{1/2}/S = 1.6 \times 10^{-15}$ for $T = 6$ K, $R = 50\ \Omega$, and $S(0) = 4 \times 10^4$ V/W. Hence we conclude that thermal fluctuation noise

should be the dominant source of intrinsic device noise within the device output bandwidth.

We measure the output noise as a function of frequency at T_{bath} = 5.2 K with the device at the optimum bias point for detection. The results are plotted in figure 2.9. At low frequency (30 Hz to 2 kHz), the output noise is measured using a low-noise voltage preamplifier (Stanford Research SR560) with a 1:60 transformer at the preamp input to step up the device impedance for optimum noise performance of the preamp. The transformer makes the measurement particularly susceptible to pickup of the 60 Hz power line frequency and its harmonics. Each low frequency data point in figure 2.9 was obtained by averaging the noise measured between 60 Hz pickup peaks. The amplifier noise has been measured separately using the Y-factor technique using a resistor with the same resistance as the device in the normal state, and the contribution from the amplifier noise has been subtracted from the data in figure 2.9. The low frequency output noise has been corrected for the signal lost to the load line, and also reduced by a factor of 4 to make it consistent with what would be measured with a 50 Ω amplifier. At high frequency (100 MHz – 1 GHz), the measurement was performed with a 50 Ω microwave amplifier. The noise of this amplifier was also measured separately and subtracted from the data.

The output noise is approximately white from 100 Hz to 100 MHz. Below 100 Hz, *1/f* noise becomes significant. We note that the relatively small *1/f* contribution is favorable, as it permits measurements with a mechanical chopper to be performed with similar sensitivity to higher frequency measurements. Above 100 MHz, the output noise rolls off with a frequency dependence that is similar to the signal power, as expected. At

frequencies beyond the response bandwidth, the dominant contribution to intrinsic device noise is Johnson noise. Photon shot noise is negligible because the device is looking at a 4 K environment.

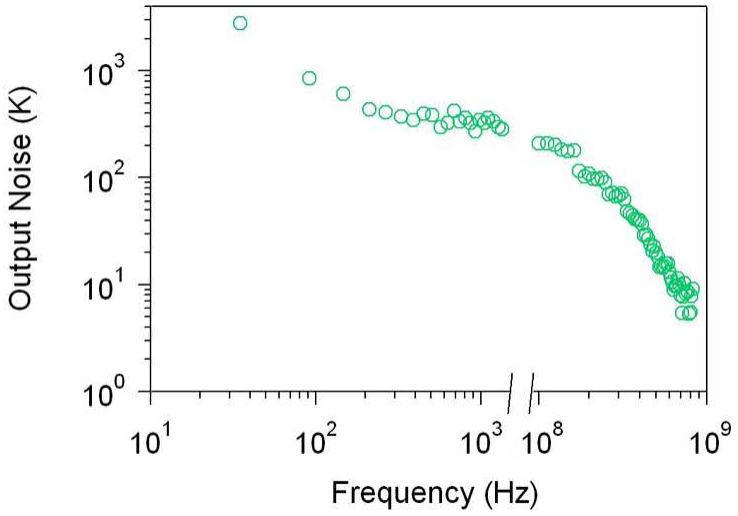

Figure 2.9. Measured noise referred to the device output as a function of frequency with T_{bath} = 5.2 K and the device at the optimum bias point for detection. Note the discontinuity in the frequency axis. The low frequency noise and high frequency noise were measured separately, as described in the text. The amplifier noise has been measured separately and subtracted.

For the frequency range 100 Hz – 100 MHz, the measured device noise referred to the device output is $T_N \approx 400$ K. Using $S(0) = 4.4 \times 10^4$ V/W, this corresponds to $NEP = 1.9 \times 10^{-14}$ W/(Hz$^{1/2}$). This is consistent with the calculated NEP_{th} using the measured thermal conductance. Hence we conclude that the device achieves a measured noise performance that is consistent with the predicted noise due to statistical thermal fluctuations.

2.3.5 Saturation power

We can also use the measured thermal conductance to estimate the expected saturation power, $P_{sat} \sim G\Delta T_c \sim 10^{-7}$ W. This is consistent with the measured saturation powers for lower bath temperatures. For the device to be useful for broadband spectroscopy of room temperature samples, it must have sufficient power handling to avoid saturation when viewing a 300 K background. For a single-mode detector such as an antenna-coupled microbridge, the available power from a blackbody source at temperature T is given by the 1D Planck distribution,

$$P_{bb} = \int_{f_1}^{f_2} \frac{hf\,df}{e^{hf/k_BT} - 1}. \qquad (2.3)$$

In the Rayleigh-Jeans limit ($k_BT >> hf$), this simplifies to the Johnson noise result, $P_{bb} = k_BT(f_2-f_1)$. If we assume an input bandwidth from f_1 = 1 THz to f_2 = 2 THz and T = 300 K, from equation (2.3) we find P_{bb} = 3.7 nW. If the coupling efficiency is η = 0.2, this becomes 0.7 nW. This is much less than the estimated P_{sat} above. If we have excess power handling, we can exchange some of this for increased sensitivity by reducing the microbridge volume. However, it was found experimentally that an increased responsivity comes at the cost of reduced saturation power (figure 2.7). The 7 nW saturation power measured at T_{bath} = 5.2 K is still sufficient for the proposed applications, but at this bath temperature any significant reduction in device volume will likely result in a device that is saturated by a room temperature background.

2.4 Terahertz characterization

To efficiently couple a free-space THz signal to an antenna-coupled device, we use a 6 mm diameter silicon hyperhemispherical lens mounted on the back of the substrate. This takes advantage of the preferential coupling to the antenna through the high dielectric substrate (Rutledge 1983). The lenses were machined by Kadco Ceramics (Easton, PA) using high-resistivity single-crystal silicon. Ray tracing shows that the focal point for a plane wave incident on a silicon sphere (ε_{Si} = 11.9) is approximately 1.10 mm beyond the center of the sphere.[4] This is consistent with the optimal extension length calculated from physical optics (Filipovic 1993, Semenov 2007). The lenses were machined with an extension 0.70 mm beyond the back of the hemisphere. The device substrate is 0.20 mm thick, double-side polished, high-resistivity silicon. We used a second piece of Si from the same batch of 0.20 mm thick wafers as an alignment piece to facilitate the positioning of the device at the center of the lens, as illustrated in figure 2.10.

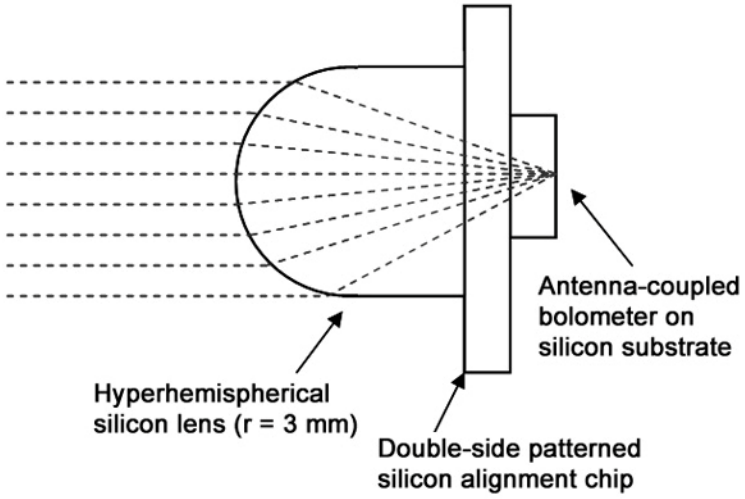

Figure 2.10. THz coupling schematic (not to scale).

[4] Spherical aberration results in rays far from the optic axis having a slightly closer focal point than rays close to the optic axis. This effect can be avoided by using an ellipsoidal lens rather than a spherical lens, but an ellipsoidal lens is more difficult to machine.

The alignment piece was patterned on both sides with alignment marks, with the markings on each side aligned relative to each other. The process for producing these pieces is described in appendix B. The lens is aligned by hand under an optical microscope to a circle of the same diameter on one side of the alignment piece. Once aligned, the lens is secured with UV-curable adhesive. The device substrate chips are 5 mm x 5 mm and are fabricated with orthogonal lines on each side that point to the position of each microbridge. These lines on the device substrate are aligned with corresponding marks on the alignment piece before the substrate is glued into place. Glue is carefully applied to the edge after the pieces have been placed together and aligned; the un-cured glue wicks around the edge. Earlier it was found that placing a layer of glue between the pieces had a non-negligible contribution to the total thickness, and also added a layer of unknown optical properties. Hence we apply glue only at the edges. With this technique, we estimate that we can achieve an alignment accuracy of ± 10 μm.

Once a device is attached to a lens, it is mounted in a homemade Cu sample holder. Electrical contact is made in the same way as the microwave sample holders described in section 2.3. However, the size of the device substrate and the alignment piece requires significantly longer wirebonds than are used in the microwave sample holder, and the resulting inductance limits efficient coupling is to below ≈ 1 GHz, which is still well beyond the response bandwidth. A photograph of a lens-coupled device in a sample holder is shown in figure 2.11.

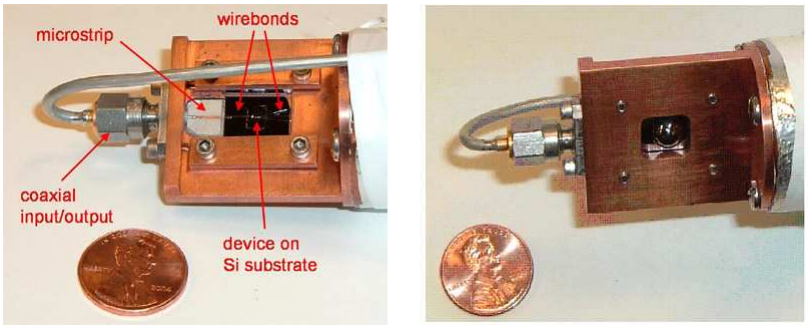

Figure 2.11. Device side (left) and lens side (right) of THz sample holder with lens-mounted device.

2.4.1 Spectrometer

To test the input bandwidth and coupling efficiency of our antenna-coupled detectors, we designed and built a THz Fourier-transform spectrometer (FTS) based on a Michelson interferometer with a broadband blackbody source. A schematic of the spectrometer is shown in figure 2.12. The device is mounted on the cold plate of an optical-access liquid ^{4}He cryostat. Initially, we used a continuous-flow Janis cryostat that was borrowed from the Schmuttenmaer lab (Yale chemistry). Later, this was replaced with an IR Labs cryostat. The cryostat window consists of a 25 μm thick Mylar (polyethylene terephthalate) sheet. An expanded Telfon (polytetrafluoroethylene) sheet is used on the cold shield as an infrared and visible filter. Teflon attenuates strongly above 4 THz. An expanded material is used because it has a lower dielectric constant, which minimizes reflection loss. For this filter material we used both a Zitex G110 membrane (ε_{Zitex} = 1.4, used in the Janis cryostat) as well as a sheet of Gore-GR (ε_{Gore} = 1.2 - 1.3, used in the IR Labs cryostat), which have similar properties (Benford 2003, Koller 2007).

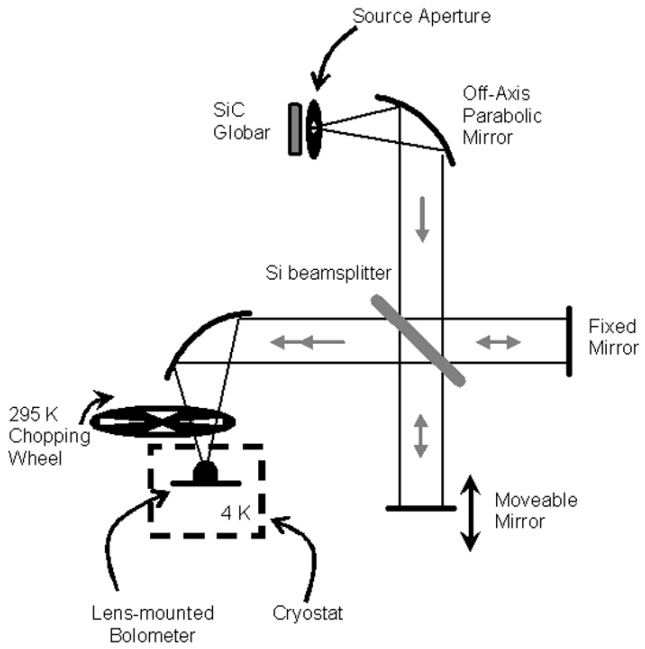

Figure 2.12. Schematic of THz Fourier transform spectrometer.

The THz source is a silicon carbide (SiC) globar,[5] which reaches a temperature of approximately 10^3 K at a bias voltage of 20 V. The temperature can be adjusted by adjusting the bias voltage. The power available to a single-mode detector from this source is given by equation (2.3). We use a 6 mm diameter iris to define the size of source. This sets a lower frequency limit of ≈ 100 GHz. The blackbody signal from the globar is collimated with a 63.5 mm diameter, 90^0 off-axis parabolic mirror.[6] The beamsplitter consists of a 6 mm thick, 100 mm diameter high-resistivity silicon wafer. This has better efficiency and broader spectral coverage than a typical Mylar beamsplitter. The Fabry-Perot resonances in the Si have a spacing of 7 GHz, and the resonances are averaged for frequency resolutions larger than approximately twice this spacing (Evans 2007). A plot

[5] Surfaceigniter Corp., model 1034K
[6] Melles Griot, part number POA-63.5-59.7

of the calculated power transmission versus frequency for normal incidence for the Si beamsplitter is presented in figure 2.13, along with a plot of the calculated power transmission for 50 μm thick Mylar (ε_{Mylar} = 3.1) for comparison. These calculations assume no loss in the beamsplitter.

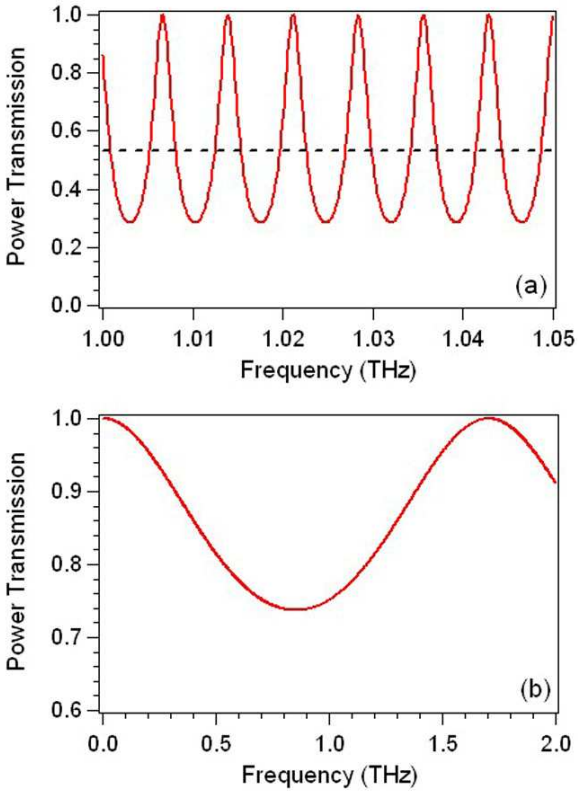

Figure 2.13. Calculated power transmission as a function of frequency for (a) 6 mm thick Si (ε_{Si} = 11.9) and (b) 50 μm thick Mylar (ε_{Mylar} = 3.1). Note the difference in scale on the frequency axes. The dashed line in (a) is the frequency-averaged power transmission, which is the result if the spectrometer resolution Δf is larger than twice the resonance spacing.

The scanning mirror is mounted on a linear translation stage controlled by an Ealing EncoderDriver linear actuator. It has a range of motion of 10 mm with a specified linear resolution of 0.02 μm and a repeatability of 0.1 μm. The combined signal from the two arms is focused onto the detector with a second parabolic mirror. The device lens is

positioned at the focal point of this parabolic mirror. The beam waist at the focal point is approximately a plane wave, and hence the focal length determined with the assumption of an incident plane wave should be valid.

The spectrometer frequency resolution is $\Delta f = c/(2 \times \text{scan length})$, and the stage range of 10 mm corresponds to a resolution of 15 GHz. The maximum frequency is $f_{max} = c/(4 \times \text{step size})$.[7] A typical step size of 10 μm corresponds to f_{max} = 7.5 THz. A mechanical chopper with a maximum chopping rate of 400 Hz is positioned in front of the cryostat window. The entire system sits inside a homemade nitrogen drybox to minimize absorption from atmospheric water. Flushing with dry nitrogen gas overnight yields a relative humidity of < 4%, measured with a commercial hygrometer. While using the spectrometer, the nitrogen drybox is maintained slightly above atmospheric pressure.

The device response at the chopping frequency is amplified by an SR560 low noise voltage preamplifier. A 1:60 transformer at the preamp input steps up the device impedance to achieve optimum noise performance of the preamp. The device is biased with a 20 Ω dc load line. A large inductor is used on the dc biasing line to minimize noise from the biasing circuit. The output of the preamp is coupled to a lock-in amplifier, which is synchronized to the chopping frequency.

To align the spectrometer, we first used a near-IR viewer to see the signal from the globar through the Si beamsplitter. A key advantage of reflective rather than refractive optics is that they have frequency-independent performance. The signals from the two arms of the interferometer are aligned and the focal point is noted. The cryostat is

[7] In the expression for f_{max}, one factor of 2 is due to the Nyquist-Shannon sampling theorem. The other factor of 2 is because the change in the optical path length is twice the mirror displacement.

then put in place, with the device located at the focal point. Final adjustments to the alignment are made using the device response at the chopping frequency.

The measured device response as a function of the mirror displacement, known as an interferogram, should always have a maximum at zero path length difference and should be symmetric about this maximum. If it is not, this indicates an alignment problem. With perfect alignment, the maximum in the interferogram is twice the baseline. A typical inteferogram is seen in figure 2.14. This is a single scan with a step size of 10 μm and a total scan length of 6 mm, corresponding to a frequency resolution Δf = 25 GHz. The measurement used a lock-in time constant of 300 ms and a time per step of 0.8 s. The total scan duration is 8 minutes, and the baseline has been subtracted. The spectral response is found by taking the Fourier transform of the measured interferogram, discussed in the next section.

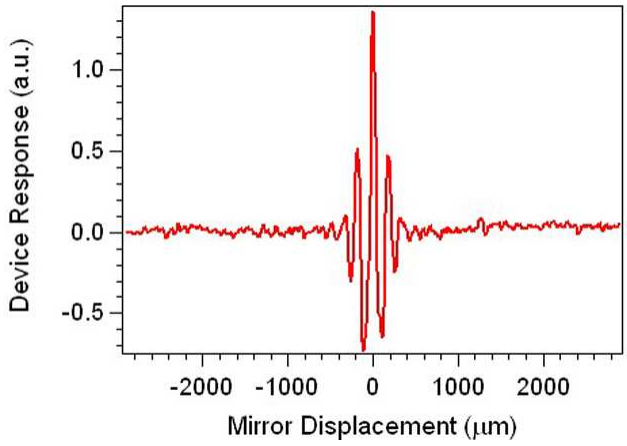

Figure 2.14. Measured interferogram of device with 79 μm double-dipole antenna.

2.4.2 Antenna characterization

The double-dipole antenna is designed such that the two half-wave dipole elements radiate in-phase in the direction perpendicular to the substrate but out-of-phase in the

direction parallel to the substrate (Skalare 1991). It is linearly polarized with approximately an octave of bandwidth. A dipole in a dielectric half-space radiates power preferentially into the high dielectric medium approximately in proportion to $\varepsilon^{3/2}$ (Rutledge 1983). This results in highly directional coupling through the hyperhemispherical silicon lens. In addition to the 38 μm double-dipole antenna seen in figure 2.1, the second generation of optically-patterned devices included double-dipole antennas with dipole lengths of 59 μm and 79 μm. Optical images of all three double-dipole geometries are seen in figure 2.15.

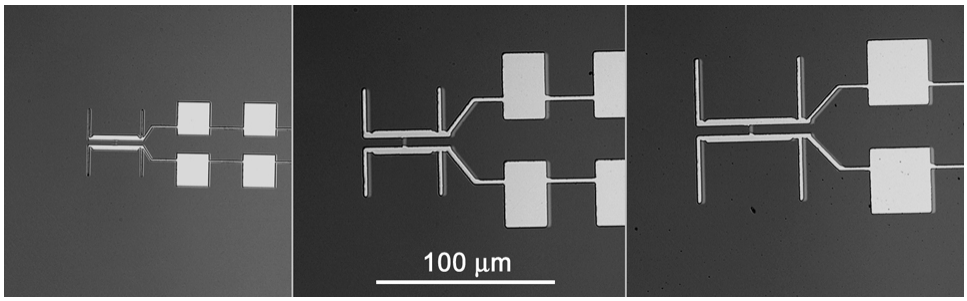

Figure 2.15. Optical images of devices with 38 μm, 59 μm, and 79 μm double-dipole antennas. Electrical leads with THz choke structure are seen to the right of each antenna. All three devices are at the same magnification.

The alternating narrow-wide structures to the right of each antenna are the electrical leads. These are designed to be an ≈ 100 Ω coplanar strip transmission line at microwave frequencies, but to be a quarter wave choke at the $\lambda/2$ antenna resonance, which prevents coupling of the THz signal to the leads. The device with the 38 μm antenna has a 2.5 μm x 1 μm microbridge and was patterned with electron-beam lithography, and is the same geometry seen in figure 2.1. The devices with the 59 μm and

79 μm antennas have 5 μm x 2 μm microbridges and were patterned with optical lithography (see appendix A).

The parallel lines on either side of the microbridge that connect the two dipoles also form a coplanar strip transmission line. The impedance of this transmission line should be matched to the microbridge impedance to avoid standing wave interference at the input frequency. Our design has an impedance of approximately 100 Ω. Conveniently, a coplanar strip transmission line on a Si substrate does not deviate more than a factor of 2 from 100 Ω for any line width and spacing that are within an order of magnitude of each other (Gupta 1979).

The power spectra obtained from taking the Fourier transform of the measured interferograms are presented in figure 2.16 for the three double-dipole geometries. We use the fast Fourier transform (FFT) algorithm in the Igor 5.0 software package. Each spectrum is from a single-scan interferogram. The structure in each spectrum is highly reproducible from scan to scan, and thus does not appear to be dominated by noise. Each spectrum displays a clear main response peak, and there is evidence for some higher frequency coupling beyond the main response peak in the 59 μm and 79 μm double-dipole spectra.

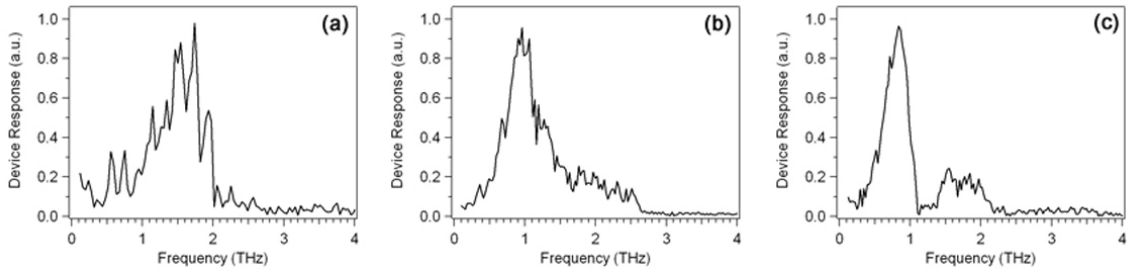

Figure 2.16. Normalized spectra for devices with (a) 38 μm, (b) 59 μm, and (c) 79 μm double-dipole antennas.

We fit the main response peak to a Gaussian function to estimate the center frequency and the bandwidth. The resonant frequency of a dipole in a dielectric half-space has been shown to be approximately equal to the resonance of a dipole in an effective dielectric equal to the mean of the actual dielectric and free space (Rutledge 1983). In table 2.2, we compare the calculated resonant frequencies to the values extracted from Gaussian fits to the measured data. There is good agreement between the calculated and the fitted results.

Double-dipole length (μm)	Calculated center frequency (THz)	Fitted center frequency (THz)
38	1.55	1.57
59	1.00	0.98
79	0.75	0.80

Table 2.2. Comparison of calculated and fitted dipole resonances.

The double-dipole antenna has about an octave of bandwidth. For many spectroscopy applications, greater bandwidth is desired. We thus fabricated and tested a more broadband antenna geometry, the log spiral (Dyson 1959). The log spiral is one of a class of antennas known as frequency independent, whose shape is completely specified by angles. The shape of the log spiral is defined in polar coordinates by the equation $\rho(\phi) = ke^{a(\phi-\phi_0)}$, where *k*, *a*, and ϕ_0 are positive constants (Balanis 2005). If we extend ϕ to $\pm\infty$, the resulting structure looks the same at any magnification up to some rotation.

For real antennas, ϕ, and hence the bandwidth, are finite. The lower frequency bound corresponds approximately to the wavelength equal to the total arm length, while the upper bound is set by the finite size of the load (in our case, the Nb microbridge). The

log spiral is circularly polarized at higher frequencies, but is linearly polarized at the low end of its bandwidth, where its response is dipole-like. Each arm in the log spiral antenna is formed by the space between two curves shifted by some angle ϕ_0. Our design is self-complimentary, in which the shift defining each arm is $\pi/2$ and the shift between arms is π. We first fabricated a design with a = 0.15, and subsequently fabricated a modified design with a = 0.50, as seen in figure 2.17. The measured spectra for these two antennas are presented in figure 2.18.

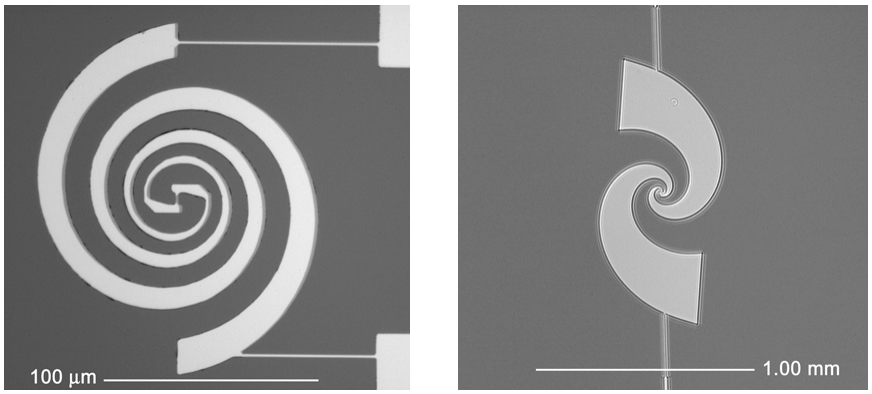

Figure 2.17. Optical images of devices with log spiral antennas with a = 0.15 (left) and a = 0.5 (right).

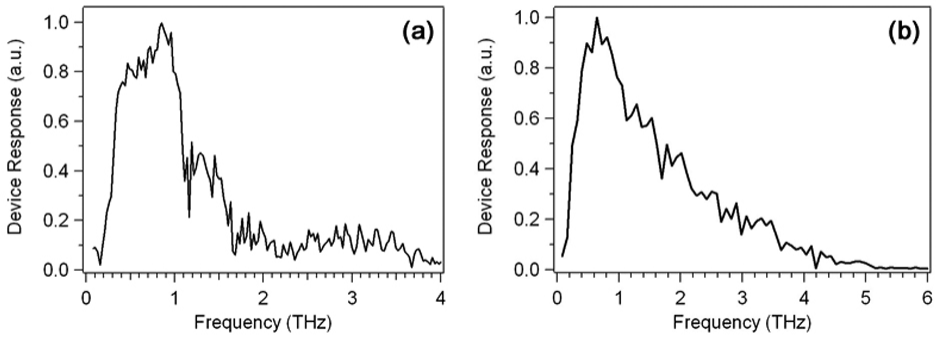

Figure 2.18. Normalized spectra of devices with log spiral antennas with a = 0.15 (a) and a = 0.5 (b).

Both log spiral antennas have a roll-on at ≈ 0.3 THz, consistent with the guideline that the largest wavelength will correspond approximately to the arm length, where the wavelength is assumed to be in an effective dielectric that is the mean of the dielectric constants of silicon and air, as before. If a 5 μm microbridge can be assumed to look point-like for wavelengths larger than 8 times its length, the upper bound of the antenna response should be ≈ 3 THz. At these frequencies, the inductance of the bridge should also be considered. The microbridge inductance of the optically-patterned devices is approximately 5 pH, which contributes to the device impedance about $j30\ \Omega$/THz. The decrease of power coupling efficiency at 3 THz due to this inductance is approximately 25%. Additionally, the skin depth scales as one over the square root of the frequency. The skin depth in the Al decreases from approximately 70 nm at 1 THz to 40 nm at 3 THz, resulting in an increase in the dissipation in the antenna by a factor of approximately 1.75.

The sharp drop in the measured $a = 0.15$ log spiral response above 1 THz is greater than the predicted loss due to the device inductance or dissipation in the Al. We believe this additional attenuation may be caused by distortion of the antenna geometry due to the thin film shadowing effect from our angled deposition process, which is described in appendix A. In figure 2.19, we show higher magnification images of the center of each log spiral antenna to illustrate this effect. The darker grey band to the right of the Al is the Nb, which is much lossier than the Al at THz frequencies. The minimum shadow size is equal to the width of the microbridge, in this case 2 μm. This shadowing becomes a greater fraction of the total arm width closer to the microbridge, causing increasing distortion at higher frequencies.

A second version of the log spiral antenna was fabricated with a = 0.5. This geometry is less compact than the previous version, but the wider arms are less susceptible to the problem of shadowing. This new design was also modified to account for shadowing, which was not done in the original design. We can see in the spectrum in figure 2.18 that the new log spiral has much better coupling above 1 THz. The gradual decrease in the signal above 1 THz is likely related to losses in the antenna and possibly also to imperfect alignment. There is also a contribution from the inductance of the microbridge, as discussed previously. This device has usable bandwidth to over 3 THz.

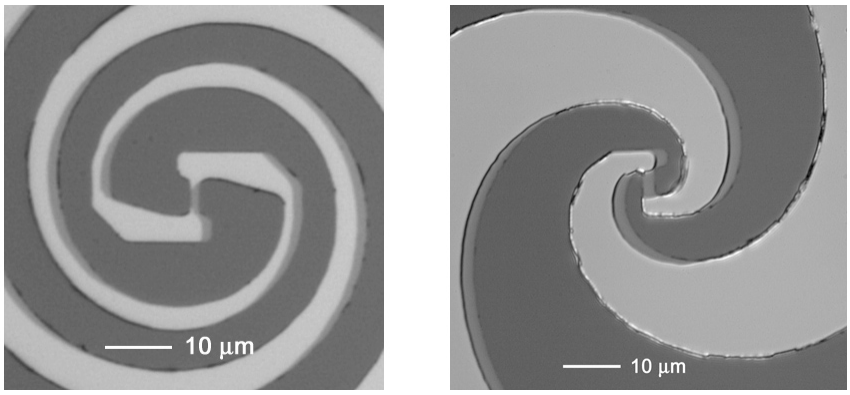

Figure 2.19. Higher magnification images of log spiral antennas with a = 0.15 (left) and a = 0.5 (right) to illustrate the shadowing effect from the angled deposition process. Lighter gray is Al and darker gray is Nb.

2.4.3 Coupling efficiency and optical NEP

We can estimate the coupling efficiency from the FTS data, but we are limited by the globar temperature, which is not precisely known. To get a better determination of the coupling efficiency, we performed a hot-cold load measurement using two blackbody sources at well-defined temperatures. This measurement used a device with a 38 μm

double-dipole antenna, which has a measured bandwidth of approximately 1.2 – 2.0 THz. A piece of Eccosorb carbon-loaded foam (Emmerson & Cuming Microwave Products) submerged in liquid nitrogen served as a cold source at 77 K, and the surface of a mechanical chopping wheel served as a hot source at 295 K. The chopping wheel surface was coated with a layer of carbon-loaded Stycast 2850FT epoxy to ensure an emissivity close to unity (Diez 2000). The chopping wheel and Eccosorb foam are positioned approximately 1 cm from the cryostat window, filling almost the entire field of view of the device lens. No focusing mirrors were used. The power difference in the antenna bandwidth, found from equation (2.3), is 2.4 nW.

The measured response for chopping at 330 Hz is seen in figure 2.20. Harmonics of 60 Hz can be seen, which are pronounced due to the use of an audio-frequency transformer. A smaller response at 275 Hz can also be seen; this is due to the inner set of openings on the chopping wheel. For comparison, we also placed a piece of room temperature Eccosorb behind the chopping wheel. A small signal is still seen, likely because the chopping wheel is not a perfect blackbody. To ensure that the signal at the chopping frequency was not due to electrical pickup, we also measured the device response with the chopping wheel blocked by metal foil.

From the measured response and the responsivity determined from microwave characterization at the same bath temperature (4.2 K), we estimate a coupling efficiency of ≈ 20%. Approximately 40% of the lost coupling efficiency is due to impedance mismatches from the Si lens (ε_{Si} = 11.9) and the Mylar window (ε_{Mylar} = 3.1). Imperfect alignment, spherical aberration, and optical losses likely account for the remaining 40%.

The noise was also measured in this experiment, determined from the noise floor of an averaged spectrum analyzer trace, similar to figure 2.20. (When measuring noise, however, the peak detect function on the spectrum analyzer is turned off.) The amplifier noise contribution was measured separately and subtracted from the total measured noise. Converting to an *NEP* using the responsivity from the microwave characterization, we find $NEP_{det} \approx 20$ fW/(Hz$^{1/2}$), consistent with the microwave noise measurements. As discussed in section 1.3.2, this is the electrical NEP, and the optical NEP is the electrical NEP divided by the input coupling efficiency. Hence we find $NEP_{optical} = NEP_{det}/\eta \approx 0.1$ pW/(Hz$^{1/2}$). This is the sensitivity that can be achieved with this experimental setup in an actual THz spectroscopy experiment.

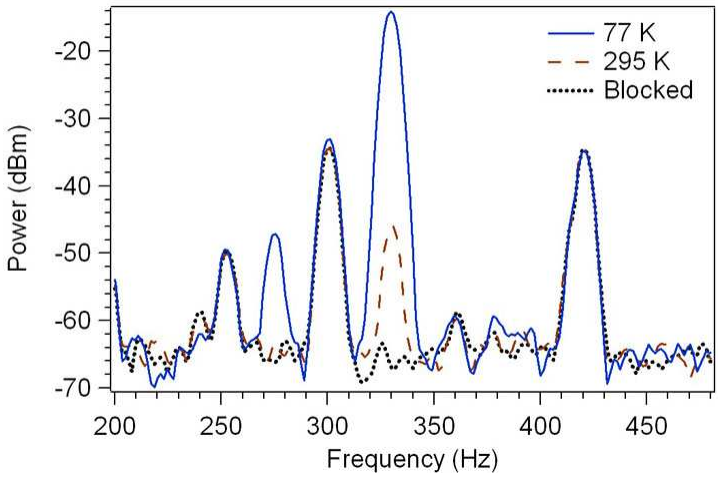

Figure 2.20. Output signal from hot-cold load measurement with sources at different known temperatures placed behind a room temperature chopping wheel. Also shown is the signal with the chopping wheel blocked. The chopping frequency is 330 Hz.

2.4.4 Antenna simulations

We performed electromagnetic simulations of the same antenna geometries in a silicon dielectric half-space in order to better understand the antenna behavior. Several

commercial software packages exist for performing fully three dimensional electromagnetic simulations. We used the software package FEKO from EM Software & Systems. This software package utilizes the method of moments (MoM) technique. In this technique, one begins by defining a geometry of interest, including both conductors and dielectrics, as well as any desired voltage sources. A grid is defined on the surface of the geometry, where the grid size should be small compared to the smallest wavelength of interest. The program then numerically solves for the charge distribution on this grid. With a known charge distribution, Coulomb's law is used to find the potential everywhere in space. This approach is particularly useful when the geometry is small compared to the region of space over which one is interested in finding the field distribution, as is often the case for antenna simulations. For more details on the MoM technique, see van der Vorst (1999).

The relatively large Si lens posed a challenge for our simulations. Using the full lens dimensions results in a simulation that takes weeks to run. We chose instead to use a feature that allows us to solve for a metallic geometry in an infinite dielectric half-space, which requires only the metallic geometry to be meshed and hence is much faster (~ minutes). This feature, however, has the restriction that losses in the metal must be neglected. We show in figure 2.21 the measured spectral response along with the simulated result for the fraction of power that is emitted when driving the antenna from a 50 Ω port at the antenna feed for the three double-dipole antennas, as well as the a = 0.5 log spiral antenna.

We see reasonable agreement between the simulation and the measured spectra for the fundamental resonance of each double-dipole antenna. Beyond the fundamental

resonance, the agreement is not as good, which is due in part to the omission of losses in the simulation. In the log spiral data, the slightly higher roll-on frequency in the measured data is likely due to the size of the globar iris and the Si lens, and the steeper roll-off at higher frequency is likely due to losses.

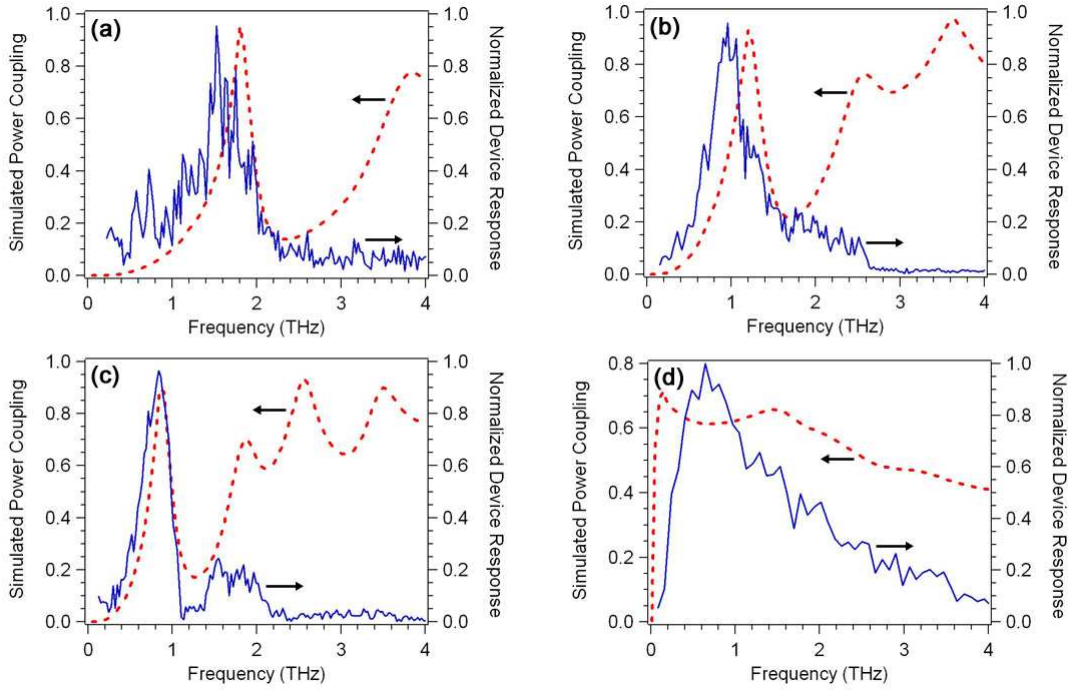

Figure 2.21. Measured response spectra and simulated power ratio of coupled power to incident power from a 50 Ω port at the antenna feed for (a) 38 μm double-dipole, (b) 59 μm double-dipole, (c) 79 μm double dipole, and (d) log spiral with a = 0.5.

We can also simulate the far-field electric field distribution from our antennas. We simulate driving the antennas with a 1 V signal across the feed, and we look at the resulting emitted electric field in the far-field (at a distance >> λ). By reciprocity, the field pattern for emission is equivalent to the field pattern for absorption (Balanis 2005). For coupling to our spectrometer, we would like an antenna with an approximately

Gaussian field distribution and without strong emission at angles far from the optic axis. As an example, in figure 2.22 we present the simulated far-field electric field distribution in both a polar plot and a full 3D plot for the 79 μm double-dipole antenna and the log spiral antenna (a = 0.5) at 1 THz. We see that both antenna geometries have reasonable beam profiles and should couple efficiently to the spectrometer at this frequency. The log spiral antenna maintains a reasonable beam profile across its entire usable bandwidth. For the double-dipole antenna, we find that the beam profile becomes irregular and hence poorly coupled at frequencies well beyond the main response peak.

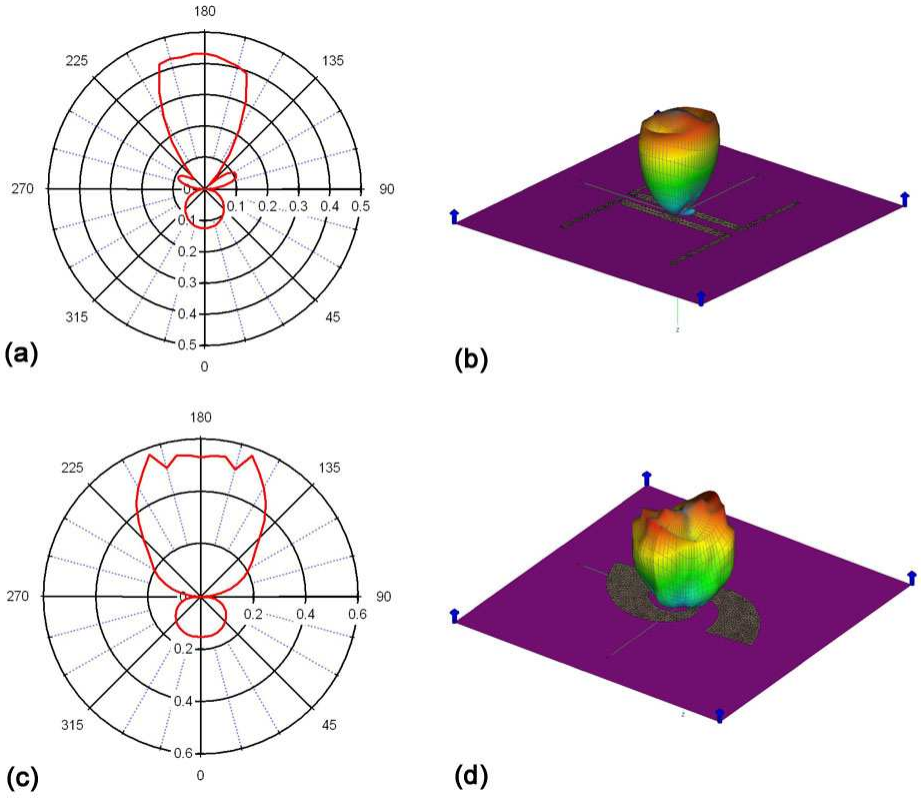

Figure 2.22. Simulated electric field distributions at 1 THz for 79 μm double-dipole (a,b) and a = 0.5 log spiral (c,d) antennas driven with 1 V across the antenna feed. The polar plots show a planar cut perpendicular to the direction of the microbridge, and 180^0 is the direction into the silicon substrate. The radial scale is in volts. In the 3D plots, the silicon side is facing up, and the electric field amplitude has been normalized in each plot.

2.4.5 Time-resolved THz spectroscopy

Measurements of these devices were also performed using the THz spectroscopy facilities in the Schmuttenmaer lab in the Chemistry Department at Yale. This included initial demonstrations of this detector in a time-resolved THz spectroscopy experiment. The Schmuttenmaer lab utilizes several fast pulsed 800 nm Ti:Sapphire lasers. These lasers have a repetition rate of 80 MHz with a pulse width of approximately 100 fs and an energy per pulse of approximately 6 nJ. For much greater pulse intensity, one of the Ti:Sapphire lasers is used to seed a regenerative amplifier that has a pulsed 800 nm output with a 1 kHz repetition rate, a pulse width of 100 fs, and a pulse energy of 1 mJ (True 2008).

A Ti:Sapphire laser is used to drive a photoconductive switch on a semiconductor substrate, which emits a broadband THz output with a bandwidth that is determined by the pulse width and the dynamical current response of the semiconductor (Smith 1988). Another photoconductive switch can be used as a detector, with part of the same optical pulse used to gate the detector (van Exter 1990, Beard 2002). We replaced this photoconductive switch detector with a niobium bolometer with a 38 μm double-dipole antenna, and we measured the device response to the emitted THz power at the 80 MHz repetition rate. The response measured on a spectrum analyzer is shown in figure 2.23. This experimental configuration could be used to perform measurements of dynamic systems with timescales much slower than the 80 MHz sampling rate. Using the measured response and the previously determined responsivity and optical coupling efficiency, we estimate that there is ≈ 1 nW of incident THz power within the device bandwidth.

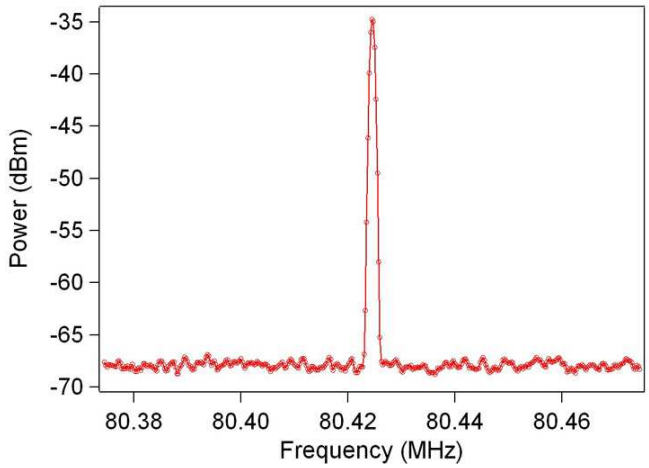

Figure 2.23. Measured device response to the THz output from a photoconductive switch driven by a pulsed Ti:Sapphire laser with an 80 MHz repetition rate. The frequency bin width is 580 Hz.

To measure at faster timescales, we can instead use a constant THz source. This approach was used to measure the free carrier lifetime in photoexcited silicon (Si) and gallium arsenide (GaAs). In these experiments, we used a detector with the a = 0.5 log spiral antenna. As a THz source, we used the same model of SiC globar used in the spectrometer described in section 2.4.1. The source signal is focused to a point and subsequently focused onto the detector using parabolic mirrors. First we placed a 200 μm thick, undoped, single-crystal Si wafer at the THz focal point. The wafer is excited with the regeneratively amplified Ti:Sapphire laser at a 1 kHz repetition rate. The laser pulse excites charge carriers in the Si from the valence band into the conduction band (Si has a bandgap of 1.12 eV = 1,107 nm), and these free charges attenuate the THz signal. The free charges return to the valence band via electron-hole recombination, and the THz signal returns to its equilibrium value. Because of the relatively slow recombination time in Si, we used a low frequency ($\leq$ 1 MHz), high-impedance preamplifier coupled to an

oscilloscope. An averaged response is shown in figure 2.24. The slight undershoot of the pulse return is due to the high-pass filter on the preamplifier. We fit the averaged response to an exponential function to determine the time constant, which is approximately 50 μs. This is consistent with previous measurements of the free carrier lifetime in undoped, single-crystal Si (Kurtz 1956).

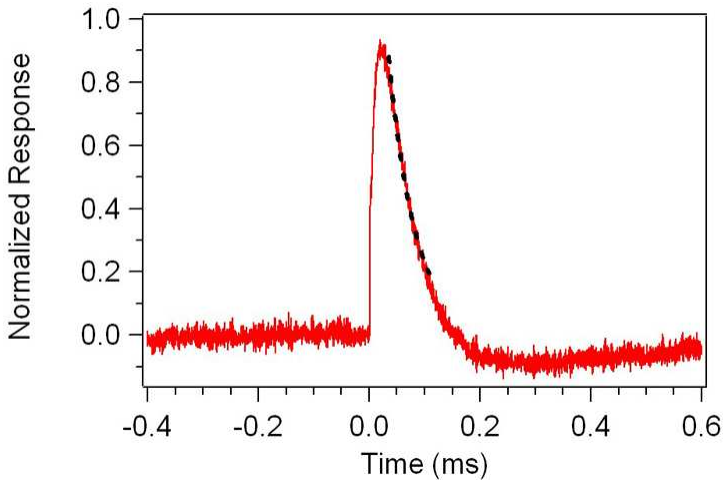

Figure 2.24. Normalized THz transmission as a function of time following photoexcitation of an undoped Si wafer. The fitted time constant is 50 μs.

We performed a similar measurement using a 500 μm thick, undoped, single-crystal GaAs wafer. The bandgap of GaAs is 1.42 eV = 870 nm. Previous measurements of the free carrier lifetime in undoped, single-crystal GaAs found a fast component due to surface recombination (< 0.5 ns) and a slower component for bulk recombination: 2.1 ns (Beard 2000) and 15 ns (Lloyd-Hughs 2006). These were optical pump-THz probe measurements using an optical delay line with a maximum delay of less than 1 ns. The discrepancy between these two reported values may be due to fitting only the beginning of the longer decay, which is complicated by the presence of a faster response at short

timescales. Our detector, although not fast enough to see the sub-ns surface response, is useful for systems with timescales > 1 ns, as it can measure the entire return to equilibrium.

Because the recombination time in GaAs is close to the detector time constant, we first determined the response time of the detector. To do this, we measured the device response to a fast (~ps) THz pulse. The fast THz pulse was generated with the 1 kHz amplified Ti:Sapphire laser driving a nonlinear zinc telluride (ZnTe) crystal. The ZnTe responds to the envelope of the excitation pulse via optical rectification, with frequency components from approximately 0.1 to several THz (Schmuttenmaer 2004). The laser required attenuation by at least 80% to prevent the resulting THz pulse from saturating the detector. The device response was measured with a 50 Ω microwave amplifier coupled to an oscilloscope. The averaged response is plotted in figure 2.25. The fitted exponential time constant is 4.4 ns. This is significantly larger than the 0.7 ns measured on a similar device (figure 2.6). The device used in this measurement has a lower T_c (4.5 K instead of 5.8 K), but this can only account for part of the difference. Further measurements are needed to resolve this discrepancy.

We also measured the response to the photoexcitation of the GaAs wafer using the constant THz signal from the globar. An average of this response is also seen in figure 2.25. We fit this response to an exponential decay with a time constant that is equal to the sum of two times, one of which is fixed at the measured device response time of 4.4 ns. The other time determined from the fit is 1.4 ± 0.5 ns. While the relatively slow detector response time prevents a precise determination of the free carrier lifetime in this measurement, our results are consistent with the 2 ns time constant for bulk electron-hole

recombination reported in Beard *et al.* (2000) and clearly inconsistent with the 15 ns reported by Lloyd-Hughs *et al*. (2006).

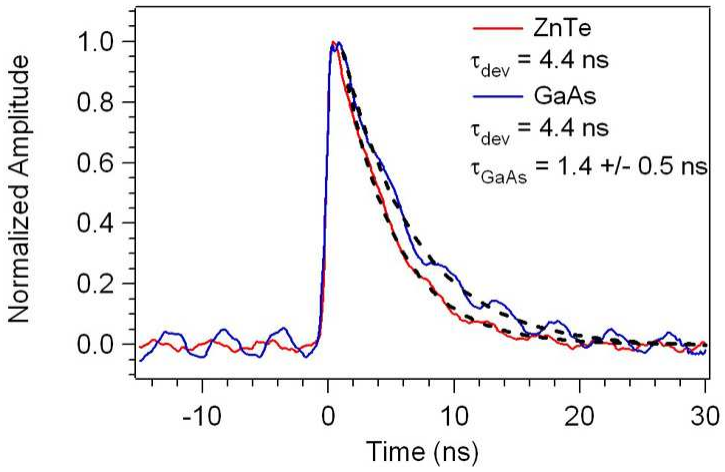

Figure 2.25. Time-resolved measurement of THz transmission through photoexcited GaAs, as well as a measurement of the device response to a fast THz pulse generated by optical rectification in ZnTe. Dashed lines are exponential fits.

2.5 Conclusion

We have developed Nb microbolometers with a sensitivity as good as the best commercially-available semiconductor bolometers and, unlike those detectors, with sufficient speed to complement existing time-resolved THz spectroscopy systems based on an optical delay line. The device performance, characterized at both microwave and THz frequencies, is consistent with theoretical predictions. In order to determine the input coupling, a THz spectrometer was designed and built. Devices with several planar THz antenna geometries were fabricated and tested, and the measured spectral response is consistent with electromagnetic simulations.

The detector has been demonstrated in an initial time-resolved spectroscopy application, in which we measured the free carrier recombination time in bulk Si and GaAs. In the future, we hope to use this system to study free carrier lifetime in other solid state systems, such as titanium dioxide and zinc oxide nanocrystals (Turner 2002, Baxter 2006), which have applications in dye-sensitized solar cells. Additionally, a spectrometer like the one described in section 2.4.2 can be added to this time-resolved spectroscopy system. This would enable measurements of the time evolution of each spectral component in the device bandwidth.

Chapter 3

Toward THz Single-Photon Detection with a Titanium Bolometric Calorimeter

3.1 Introduction

Terahertz (THz) detectors have been an active area of research during the past decade, but an energy-resolving THz single-photon detector – i.e., a THz calorimeter – has remained elusive. Previous work on semiconductor quantum dot detectors demonstrated the first THz single-photon detection (Komiyama 2000, Astafiev 2002, Ikushima 2006), but with a complex device geometry, poor quantum efficiency (≈ 1%), and without the ability to resolve the photon energy.

One candidate to achieve energy-resolved THz single-photon sensitivity is the transition edge sensor (TES). As discussed in section 1.2, this is a bolometric device with the same principle of operation described in previous chapters. However, the term TES usually refers to a large-area detector ($> \lambda^2$) operating with strong negative electrothermal feedback via a low-impedance readout. The most sensitive TES detectors operate at very

low temperatures (typically < 100 mK) and are relatively slow (typically ~ ms). For a detailed discussion of TES detectors, see the article by Irwin and Hilton (2005).

An alternative to the conventional TES was proposed by Karasik *et al.* in 1999. This approach combines an antenna-coupled nanoscale superconducting bolometric element with higher T_c contacts to achieve quasiparticle confinement in the bolometric element via Andreev reflection. In the Andreev reflection process (Andreev 1964, Tinkham 1996), quasiparticles with energies less than the superconducting energy gap of the contact material must join with another quasiparticle located symmetrically on the other side of the Fermi energy in order to form a Cooper pair and pass into the superconducting contact, as illustrated in figure 3.1. This permits an electrical current but prevents the flow of energy. A quasiparticle system with energies within the superconducting gap of the contact can only lose energy via phonon emission, and hence the thermal conductance of the electron system in the bolometric element is equal to the electron-phonon thermal conductance.

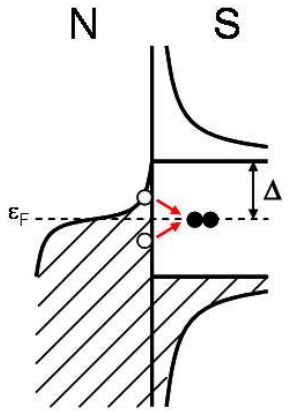

Figure 3.1. Sketch of the Andreev reflection process for passing current through a normal metal-superconductor (NS) junction at energies less than the superconducting gap energy Δ. An electron incident on the interface from the normal metal side must pair with another electron located symmetrically about the Fermi energy ε_F to pass into the superconductor as a Cooper pair. Open circles represent holes and filled circles represent electrons.

The combination of these design elements – a very small active device volume and the confinement of excited quasiparticles – increases the device sensitivity by decreasing the electronic heat capacity and the thermal conductance. This approach is predicted to be capable of THz single-photon sensitivity using a nanoscale titanium (Ti) superconducting bolometric element with the relatively high operating temperature of 300 mK and with a relatively fast time constant ~ μs (Karasik 1999), where relative refers to the most sensitive TES detectors. In this chapter, we describe our characterization of this type of Ti nanobolometer using a new experimental technique. We perform the first direct measurements of the energy resolution of this type of device and find that its performance is consistent with theoretical predictions.

3.1.1 Space-based mid-infrared and THz astronomy

A single-photon-sensitive THz detector with high quantum efficiency is critical for proposed next-generation space-based far-infrared telescopes. These missions – including NASA's Single Aperture Far Infrared Observatory (SAFIR) and Submillimeter Probe of the Evolution of Cosmic Structure (SPECS), as well as the European and Japanese collaboration Space Infrared Telescope for Cosmology and Astrophysics (SPICA) – propose to achieve a sensitivity that is limited by the astronomical background photon flux using reflectors that are actively cooled to ~ 4 K (Leisawitz 2004, Swinyard 2009).

Moderate resolution spectroscopy ($\lambda/\delta\lambda \sim 1000$) using direct detectors with an external frequency-selective element (e.g., a grating) are proposed for studies of star and galaxy formation. For space-based detection at frequencies below 1 THz, the background photon arrival rate increases rapidly with decreasing frequency due to the exponential tail

of the cosmic microwave background spectrum. Above 1 THz, the background photon arrival rate is dominated by emission from interstellar dust and the galactic core. As seen in figure 3.2, the calculated background photon arrival rate between 1 and 10 THz is ~10^2 photons per second for a single-mode, single-polarization detector with 25% coupling efficiency and a resolution $\lambda/\delta\lambda = 10^3$ (Wei 2008).

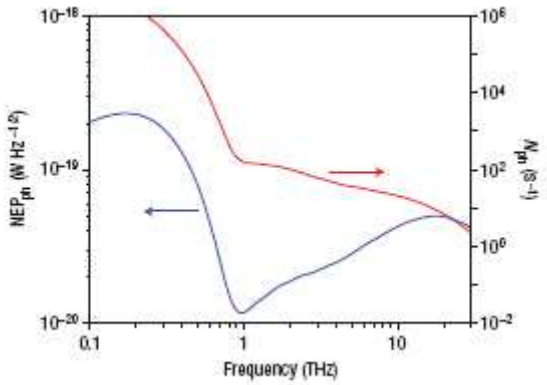

Figure 3.2. Calculated background photon arrival rate N_{ph} and background-limited noise equivalent power NEP_{ph} for a space-based single-polarization, single-mode detector with 25% coupling efficiency and a spectral resolution $\lambda/\delta\lambda = 10^3$, from (Wei 2008).

To efficiently resolve randomly arriving photons, one needs a detector with an exponential time constant that is approximately an order of magnitude faster than the arrival rate. As astronomers are searching for signals that are above the background, a useful single-photon detector will be at least 2-3 orders of magnitude faster than the background photon arrival rate. At present, the most sensitive TES detectors do not meet this count rate requirement, nor do they have single-photon sensitivity for photon energies $E_{ph} < 0.1$ eV. With the Ti nanobolometer described in this chapter, however, counting individual THz photons (E_{ph} ~ 1-10 meV) in space becomes feasible. With such

a device, low resolution spectroscopy ($\lambda/\delta\lambda \sim 10$) in the mid-infrared and THz can be performed without an external spectral dispersion element using the detector energy resolution (Karasik 2005). Applications of such a spectrometer-on-chip include studies of interstellar dust composition and the search for Earth-like exoplanets (Lawson 2006).

3.1.2 THz single-photon spectroscopy in the laboratory

An ultra-sensitive detector as described above would also create new possibilities for laboratory-based THz spectroscopy at the single-photon level. Many electronic nanosystems have excitations in the THz range (~1-10 meV). The THz emission from an individual nanosystem is in general extremely weak, and ensemble measurements tend to average out properties that are of particular interest, such as geometric- or conformation-specific resonances. A detector with single-photon sensitivity would thus create new possibilities for studying the excitation spectra of individual nanosystems in the THz regime. One example is the thermal radiation from an individual single-walled carbon nanotube. The nanotube is predicted to act as a dipole antenna with THz resonant modes that are determined by the propagation of plasmon waves along the length of the nanotube (Nemilentsau 2007). Another example is the recent proposals by Ryzhii *et al*. (2007) and Rana (2008) to achieve THz emission via electron-hole recombination in optically- or electrically-pumped graphene. This behavior has also been predicted for a metallic carbon nanotube (Kibis 2007).

3.2 Detector overview

The devices we have studied consist of a superconducting titanium (Ti) nanobridge approximately 4 μm long, 350 nm wide, and 70 nm thick, with T_c = 0.3 K, as seen in figure 3.3. The dimensions of the Ti nanobridge were chosen to have an impedance close to 50 Ω in the normal (non-superconducting) state to facilitate efficient high-frequency coupling. The Ti nanobridge spans contacts consisting of thick niobium (Nb) with T_c = 8 K. It was found that effective quasiparticle confinement by the Nb contacts is only achieved if the Ti volume does not extend far underneath the Nb (Wei 2008). This was determined by comparing the measured time constant of nanobridge devices with the time constant of large-area films with the same T_c. If the Ti extends far underneath the Nb, the effective Ti volume is much larger than the volume of the Ti in the nanobridge. This leads to a time constant that is faster than the electron-phonon time due to enhanced cooling via the outdiffusion of excited quasiparticles, as well as a larger thermal conductance and heat capacity due to the increased effective Ti volume. This results in a reduced sensitivity, and hence we employ devices in which the Ti extends only slightly underneath the Nb, as seen in figure 3.3(a).

We measured two devices with nominally identical geometries from a single chip. The dc properties of these two devices were nearly indistinguishable. All of the energy resolution data presented in this chapter are from a single device. The devices were fabricated by David Olaya in the group of Prof. Michael Gershenson at Rutgers University. The fabrication process utilized electron-beam deposition of both metals with an angled shadow mask technique on a high-resistivity silicon substrate. A detailed description of the fabrication process can be found in (Wei 2008).

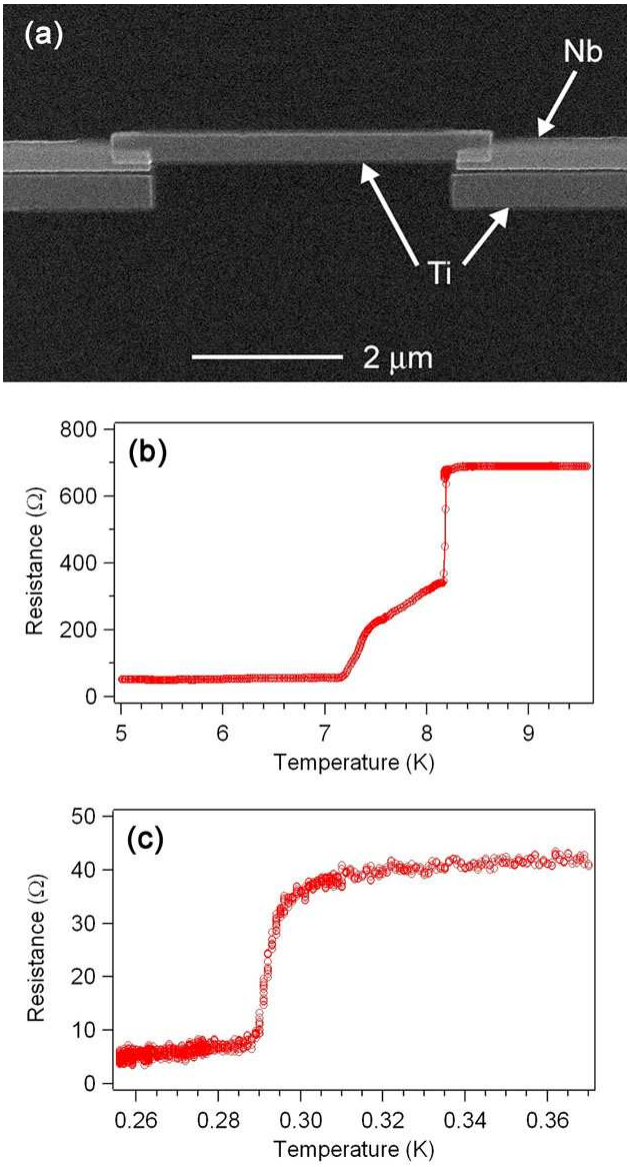

Figure 3.3. (a) Scanning electron micrograph of Ti nanobolometer device with Nb contacts. The strips of Ti seen below each Nb contact are not electrically connected and are an artifact of the fabrication process. (b) Resistance as a function of temperature, measured with a bias current of 100 nA, showing the superconducting transition of the Nb contacts. (c) Resistance as a function of temperature, measured with a bias current of 10 nA, showing the superconducting transition of the Ti nanobridge.

For photons with a frequency greater than the upper frequency scale for superconductivity in the Ti, $f_{Ti} = 3.53k_BT_c/h = 22$ GHz, the nanobridge impedance is approximately equal to the normal state resistance $R_n \approx 45\ \Omega$. In practice, the

superconducting energy gap in the Ti is suppressed by the temperature and the bias current, so the relevant frequency scale is well below 22 GHz. The much larger superconducting energy gap in the Nb contacts, $\Delta_{Nb} = 1.76 k_B T_c \approx 1.2$ meV, creates Andreev mirrors that prevent the outdiffusion of heat from the Ti nanobridge if the excitations in the Ti have energy less than Δ_{Nb}. When detecting a THz photon, the time for the initially excited photoelectron to share its energy with other electrons in the Ti and relax below the Nb gap energy is $\tau_{e\text{-}e} \sim (10^8 R_{sq} E/k_B)^{-1} \sim 0.1$ ns (Abrahams 1981, Santhanam 1984), where E is the electron energy and R_{sq} is the sheet resistance. The initial hot spot will spread a distance $\sim (D \tau_{e\text{-}e})^{1/2} \sim 0.1$ μm, where D is the diffusion constant, while the excitations cool to below Δ_{Nb}. This is much less than the device length, so energy loss by diffusion to the Nb contacts should be negligible. The energy loss of the electron system is set by electron-phonon coupling within the Ti, with an electron-phonon thermal time constant of a few μs (Karasik 1999, Wei 2008).

The initial temperature rise of the electron system due to an absorbed photon is $\Delta T = hf/C_e$, where f is the photon frequency and C_e is the electronic heat capacity of the Ti nanobridge. This assumes that the electron-electron energy sharing is fast compared to electron-phonon coupling, which is a realistic assumption. The corresponding resistance increase changes the microwave reflection coefficient at frequencies well below f_{Ti}. In the absence of electrothermal feedback, the thermal relaxation time is $\tau_0 = C_e/G_{e\text{-}ph}$, where $G_{e\text{-}ph}$ is the electron-phonon thermal conductance.

DC properties of similar Ti devices were studied in Wei *et al.* (2008) to determine $G_{e\text{-}ph}$ as a function of temperature. In that work, they report a thermal conductance per unit volume $g(T) = (3.3 \times 10^9 T^4)$ $WK^{-1}m^{-3}$. The thermal conductance was determined by

measuring the superconducting critical temperature with various dc bias currents and using the relationship $I^2R = G[T_c(0)-T_c(I)]$, where $T_c(0)$ is the critical temperature measured with negligible bias current and $T_c(I)$ is the critical temperature measured with a dc bias current I. This technique requires a device with a uniform shift in the $R(T)$ curve at the superconducting transition with increasing bias current.

Wei *et al*. (2008) also determined τ_0 by measuring the response to near-IR photons. A relatively large Ti volume, ~1.5 μm^3, was used to avoid saturation. The measured time constant was consistent with the time constant found from the measured $G_{e\text{-}ph}$ and the calculated value of the electronic heat capacity C_e for bulk Ti, $C_e = (310\ Jm^{-3}K^{-2})TV$, where V is the Ti volume.

3.3 Characterization technique

A test system to study the detector response to single THz photons is feasible but presents significant technical challenges. A THz source coupled from outside the cryostat must be highly attenuated due to room temperature blackbody photons. The radiation power absorbed in the device should not exceed ~fW to avoid exceeding the detector count rate. This requires carefully tuned attenuation of the source and filtering of the out-of-band photon flux. To date, no one has made such a system. Use of a photon source internal to the cryostat avoids uncontrolled emission by a warm coupling structure but still requires carefully calibrated filtering. Collaborators at JPL are presently implementing such a system, but the engineering challenges are significant.

To facilitate rapid device characterization, we have developed an alternative testing technique that is easier to implement (figure 3.4). This technique avoids the

problem of unwanted background photons and allows for a precise determination of the coupling efficiency, as well as trivial adjustment of the input energy. The device is mounted in the light-tight inner vacuum can of a ^{3}He cryostat with a base temperature of 230 mK. Absorption of a single THz photon is simulated by absorption of a 20 GHz microwave pulse with a duration of 200 ns, which is much shorter than τ_0. The absorbed energy of the 20 GHz pulse is equivalent to the energy of a single higher frequency photon. We call this pulse a faux photon, or fauxton.

The fauxton pulse is generated with a commercial microwave source, and is highly attenuated using cryogenic attenuators. The fauxton frequency is adjusted simply by changing the amplitude of the microwave signal. Since 20 GHz is greater than the frequency scale for superconductivity in the biased Ti nanobridge, the device appears resistive at 20 GHz, with the device impedance approximately equal to R_n, as it does for an actual THz photon. The pulsed microwave source provides an external trigger for detection. This is very useful in cases where the signal-to-noise ratio (S/N) of the detector is low. Low S/N is typical during the early stages of detector development. As the S/N is improved, the photon signal itself can be used to trigger.

The impedance change when a fauxton is detected is recorded by measuring the change in the reflected power at 1.4 GHz. The ratio of reflected power to incident power is $|\Gamma|^2$, where Γ is the voltage reflection coefficient, defined as $\Gamma = (Z-Z_0)/(Z+Z_0)$. Here Z is the time-dependent device impedance, approximately resistive and near in magnitude to R_n, and Z_0 is the characteristic impedance of the coupling circuit, in this case 50 Ω. The nanobridge geometry has negligible stray capacitance, and the dominant source of inductance is the self-inductance of the nanobridge itself, which is ≈ 1 pH/μm. Thus a 4

μm nanobridge has an inductive contribution to its impedance $j\omega L$ of approximately $j0.03$ Ω at the 1.4 GHz probe frequency and approximately $j0.5$ Ω at the 20 GHz fauxton frequency. At 1 THz, however, this becomes $j25$ Ω. We see that the inductive contribution to the device impedance can be neglected at microwave frequencies, but at THz frequencies it should be taken into account.

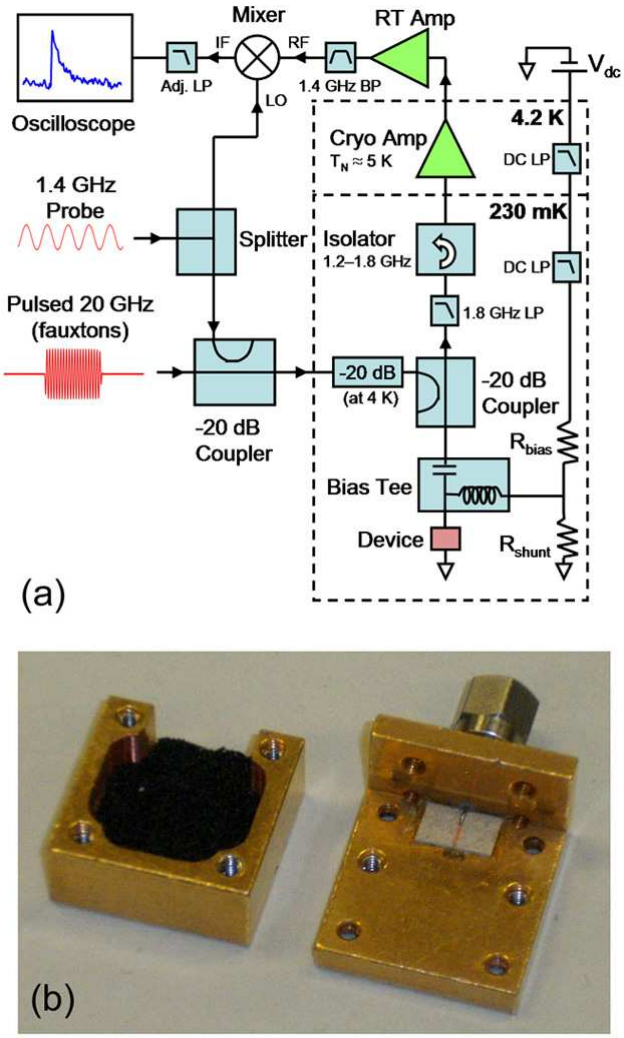

Figure 3.4. (a) Schematic of experimental setup for fauxton testing. LP stands for low-pass filter and BP stands for band-pass filter. Some attenuators have been omitted for clarity. (b) Photograph of device in single-port microwave sample holder. The device is wirebonded to a 50 Ω microstrip on one side and to the body of the gold-plated copper sample holder (ground) on the other. Carbon-loaded foam attached to the inside top of the sample holder is used to attenuate unwanted cavity modes.

The 1.4 GHz probe signal reflected by the device is amplified using a low noise cryogenic amplifier ($T_{amp} \approx 5$ K). An impedance-matched 1.8 GHz low pass filter, designed to be dissipative rather than reflective in its stop-band, prevents saturation of the amplifiers by the 20 GHz fauxton signal and also maintains a matched termination at the output of the directional coupler, which avoids spurious resonances. (For more on this type of filter, see appendix C.) The probe signal is amplified further at room temperature, narrow bandpass filtered at 1.4 GHz, and coupled to the RF port of a commercial heterodyne mixer. A portion of the original probe signal is used as the mixer LO input, which is phase-matched to the RF signal. For fauxton detection, the IF output is low-pass filtered and coupled to an oscilloscope. As an example, we plot in figure 3.5 the reflected probe power (measured with a diode power detector in place of the mixer) as a function of temperature with zero dc bias current, and also as a function of dc bias current at a bath temperature of 240 mK.

In considering the effect of the 1.4 GHz bandpass filter, it is helpful to sketch the frequency spectrum at the RF input of the mixer. In figure 3.6, we sketch a representation of this spectrum, where for simplicity we consider only a discrete set of frequencies with a uniform spacing Δf. We have a carrier frequency (the 1.4 GHz probe signal) that is modulated by the device response and the thermal fluctuation noise, producing sidebands. We assume a time constant $\tau = 1/\Delta f$, so the sidebands are each represented by a single frequency component. We also assume that the amplifier noise is frequency-independent. The RF input bandwidth B is set by external filters.

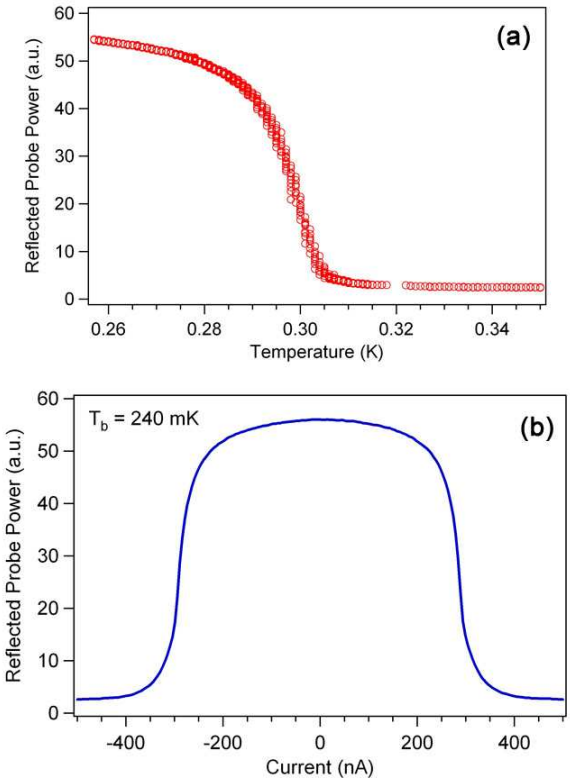

Figure 3.5. Reflected 1.4 GHz CW probe power (a) as a function of temperature, with no dc bias current, and (b) as a function of dc bias current at a bath temperature of 240 mK.

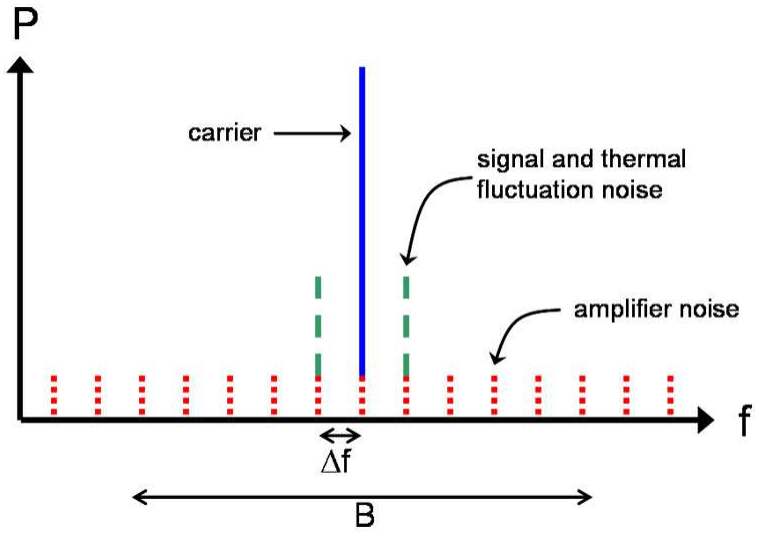

Figure 3.6. Schematic representation of frequency spectrum at RF input of the heterodyne mixer. Typical values are Δf = 100 kHz and $B \approx 10$ MHz.

The mixer multiplies the different frequency components, and we assume that the IF output is filtered so that only components with a difference frequency Δf are recorded. We can readily see that the ideal RF input bandwidth is $B = 2\Delta f$, centered on the carrier tone, as this would encompass both signal sidebands. A larger input bandwidth only increases the contribution from amplifier noise. However, if we assume that the carrier signal is much larger than the signal and noise amplitudes, as is generally the case, then the dominant source of amplifier noise at the filtered diode output will be from the noise spectral components that mix with the carrier tone. In this case, the additional noise at the IF output due to an RF input bandwidth that is somewhat larger than optimum will be small. Hence the precise value of the bandwidth B of the bandpass filter on the RF input does not have a large effect on the measured energy resolution, as long as $B > 2/\tau$.

The IF output is coupled to a low-noise preamplifier with adjustable high- and low-pass filters, and the preamplifier output is coupled to an oscilloscope. The passband of the low-pass filter is chosen to maximum the signal-to-noise. The bandwidth of this filter *does* have a significant effect on the measured energy resolution and should be $\approx \Delta f$, as we will see in section 3.4. The high-pass filter is useful to minimize jumps in the baseline, which are occasionally observed, although setting it too high will create ringing in the pulse decay.

A microwave measurement of the device impedance takes advantage of the low noise amplifiers available at these frequencies and avoids problems with electromagnetic pickup at lower frequencies. We also note that this microwave reflection readout technique could be employed for frequency division multiplexing of a large-format detector array. In this technique, a frequency comb is applied to an array of detectors,

with each frequency coupling to a particular detector via a resonant circuit, which can be fabricated on-chip along with the detectors. The reflection of the entire frequency comb can then by amplified by a single cryogenic microwave amplifier with a bandwidth $B >> 1/\tau$. At room temperature, the amplified signal can be mixed down to a lower frequency range and then coupled to a sufficiently fast analog-to-digital converter for processing. For more on frequency division multiplexing of superconducting detector arrays, see e.g. Mazin *et al.* (2006).

The fauxton pulse has statistical variations in the number of microwave photons equal to $N^{1/2}$ for a pulse with an average of N photons, resulting in a root-mean-square (rms) energy uncertainty of $hf(N^{1/2})$, with f the microwave frequency. A 20 THz fauxton will have $10^3 \pm 32$ photons at 20 GHz. This corresponds to an rms energy uncertainty of 0.63 THz, which is well below the energy resolution of present devices.

The 20 GHz coupling efficiency is calibrated *in situ* using Johnson noise thermometry. With the device above T_c, we apply on the dc line a square wave audio frequency signal that switches between zero and finite voltage, and we measure the corresponding change in noise on the diode (with no probe signal). Then we apply a square-wave-modulated (on-off) 20 GHz signal, adjusting the amplitude to achieve the same noise signal on the diode. We know the power dissipated in the device by the signal from the dc line, and we use this to directly determine the coupled power at 20 GHz.

The biasing condition is set by resistors mounted at the base temperature, R_{bias} and R_{shunt} in figure 3.4. Copper powder filters mounted at 4.2 K and 240 mK are used to provide additional attenuation of high frequency noise (Martinis 1987). The biasing line connects to the device through the dc port of a bias-tee, which has a bandwidth from dc -

5 MHz. We used R_{shunt} = 50 Ω and R_{shunt} = 3 Ω. (R_{shunt} = 50 Ω was a standard 50 Ω load; R_{shunt} = 3 Ω was a 1 dB cryogenic attenuator with a shorting cap.) R_{shunt} determines both the dc biasing condition and the load line seen at all frequencies relevant to the thermal response, since $R_{shunt} << R_{bias}$ = 1 MΩ. The optimum dc bias point is the same as the Nb bolometers discussed in chapter 2.

3.4 Results

The fauxton characterization technique allows us to directly measure the detector time constant. It also permits us to study the detection statistics, from which we can determine the experimental energy resolution. These results have previously been reported in Santavicca *et al.* (2009).

3.4.1 Detector time constant

The time constant is defined as the time for the signal to decay by a factor of e^{-1} from the peak excursion following a detection event. Averaged detected waveforms for both values of R_{shunt} are presented in figure 3.7. The rise time is limited by the low-pass filter on the preamplifier at the mixer IF output, which in the data of figure 3.7 was 100 kHz for R_{shunt} = 50 Ω and 300 kHz for R_{shunt} = 3 Ω. The fall time is exponential, and we fit this to find the time constant. R_{shunt} = 50 Ω corresponds approximately to the case of matched source and load impedances, which is intermediate between a current bias and a voltage bias and hence there is no electrothermal feedback. In this case we should measure the intrinsic time constant, $\tau_0 = C_e/G$. We find τ_0 = 7 μs, in good agreement with (Wei 2008) for T = 0.30 K.

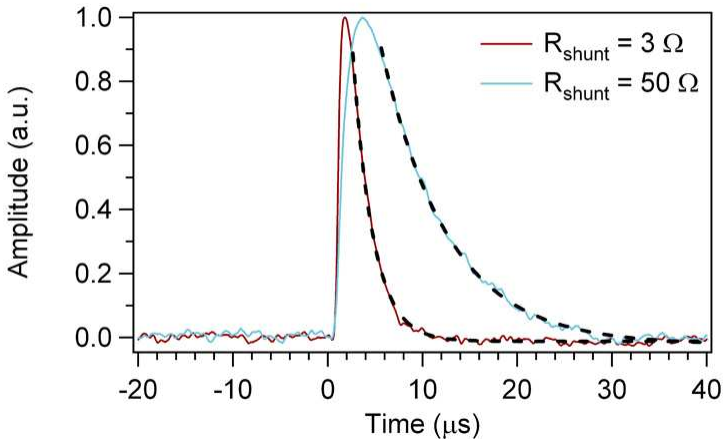

Figure 3.7. Normalized averages of 10^3 measured pulses for fauxton detection with R_{shunt} = 50 Ω and 3 Ω. Dashed lines are exponential fits with time constants of 7 μs (R_{shunt} = 50 Ω) and 2 μs (R_{shunt} = 3 Ω).

Next we calculate the time constant with electrothermal feedback. We start from the one-dimensional heat flow equation

$$C\frac{dT}{dt} = P_{in} - P_{out}\,. \tag{3.1}$$

Because R_{shunt} = 3 Ω is much less than the device impedance, we have a voltage bias, and the input power due to Joule heating is $P_{in} = V^2/R(T)$. The power output is due to cooling via phonon emission, with $P_{out} = P_{e\text{-}ph} = A(T^n - T_{bath}^{\ n})$, with a corresponding thermal conductance $G = dP_{e\text{-}ph}/dT = nAT^{n-1}$. We use n = 5 based on the determination of the temperature-dependent thermal conductance from (Wei 2008). If we assume a small temperature rise ΔT, we can expand equation (3.1) to first order,

$$C\frac{d\Delta T}{dt} = \frac{-V^2}{R_0^{\ 2}}\frac{dR}{dT}\Delta T - G\Delta T \tag{3.2}$$

where R_0 is the equilibrium resistance. The solution to equation (3.2) is an exponential with a time constant

$$\tau_{eff} = \frac{\tau_0}{1 + \frac{\alpha}{n}\left[1 - \frac{T_{bath}{}^n}{T^n}\right]} \tag{3.3}$$

where $\tau_o = C/G$ is the intrinsic time constant and $\alpha = (T/R)(dR/dT)$, which serves as a measure of the strength of electrothermal feedback. If we had assumed a current bias (positive electrothermal feedback), the addition sign in the denominator would instead become a subtraction sign. We note that equation (3.3) is equivalent to the τ_{eff} found in section 1.4.1. For a substrate temperature T_{bath} = 0.24 K and a device temperature $T \approx T_c$ = 0.30 K, we find good agreement between the calculated value of τ_{eff} using equation (3.3) and the measured value τ_{eff} = 2 μs with α = 20.

3.4.2 Energy resolution

At different absorbed fauxton energies E_{abs}, we measure a sequence of 10^3 pulses with R_{shunt} = 3 Ω and record each single-shot waveform. In the linear response regime, the average peak height is proportional to the fauxton frequency, $f_{fauxton} = E_{abs}/h$. As an example, we plot in figure 3.8 a single-shot measurement and an averaged measurement for $f_{fauxton}$ = 50 THz. These data were taken with a 100 kHz low-pass filter on the mixer IF output. The time constant found from fitting to the averaged measurement is 3.7 μs. This is longer than the 2 μs for R_{shunt} = 3 Ω found in section 3.4.1 because of the dependence of the parameter α on the dc bias point, which has been carefully chosen for optimum signal-to-noise in this measurement. The bias-dependent time constant τ_{eff} can also be calculated directly from the dc I-V curve, as it can be shown that, for a voltage bias, $(\alpha/n)(T_{bath}{}^n/T^n - 1) = (I^2/G)(dR/dT) = (dV/dI - V/I)/(dV/dI + V/I)$ (Karasik 1996).

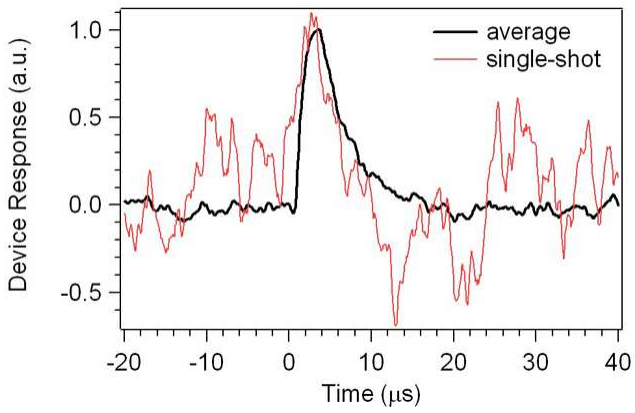

Figure 3.8. Single-shot measurement of device response to a 50 THz fauxton, along with an average of 10^3 single-shot measurements for the same fauxton frequency.

We determine the peak height at a fixed time after the trigger for each single-shot pulse using an average over a 2 μs window. We then make a histogram of the heights of all 10^3 measurements for each fauxton energy. The histograms are fit to a Gaussian function to extract the average peak height and the full-width at half-maximum (FWHM). In figure 3.9, we plot the histograms for measurements of fauxton energies of 50 THz and 25 THz, as well as a measurement with no fauxtons with the same bias point and probe power. We observe that the response is linear with fauxton energy, and the total measured FWHM energy resolution is $\delta E_{total} = 49 \pm 1$ THz. We also plot the histogram of the signal amplitude measured in the same 2 μs time window with the device biased well above the superconducting critical current I_c, where the device should be, to a good approximation, a temperature-independent resistor. In this case the width of the histogram is due primarily to amplifier noise, and we find $\delta E_{amp} = 43$ THz FWHM. We can then estimate the intrinsic device energy resolution $\delta E_{intrinsic}$ by assuming that the device noise and

amplifier noise are uncorrelated, and hence $\delta E_{total}^2 = \delta E_{amp}^2 + \delta E_{intrinsic}^2$. We find $\delta E_{intrinsic} \approx 23$ THz FWHM.

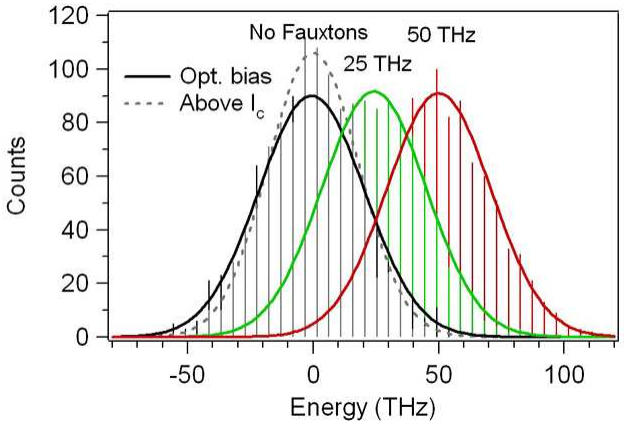

Figure 3.9. Histograms of single-shot device response to 50 THz fauxtons, 25 THz fauxtons, and no fauxtons. Also shown is the energy resolution measured with the device above I_c.

To calculate the theoretical energy resolution, we start by expressing the mean square temperature fluctuations of equation (1.13) as energy fluctuations, $\langle \delta E^2 \rangle = k_B T^2 C$. Assuming that we are in the isothermal regime with no electrothermal feedback and the only source of noise is the statistics of energy exchange between the device and the environment, we get an rms energy resolution

$$\delta E_{rms} = \sqrt{k_B T^2 C} \,. \tag{3.4}$$

This is sometimes referred to as the "thermodynamic limit," although it does not represent an actual limit on the attainable energy resolution. To find the energy resolution of a real device, we must account for electrothermal feedback and the contribution of other noise sources in addition to thermal fluctuation noise.

As we saw in chapter 1, the FWHM energy resolution is related to the *NEP* by

$$\delta E = 2\sqrt{2\ln 2}\left[\int_0^\infty \frac{4df}{NEP^2(f)}\right]^{-1/2} \tag{3.5}$$

where the factor $2(2\ln 2)^{1/2}$ is from the conversion from rms to FWHM (Moseley 1984). The integration over all (positive) frequencies requires that we consider all relevant contributions to the total NEP. It is instructive to consider here the frequency spectrum of the signal and the relevant sources of noise. In figure 3.10, we show an example of such a spectrum for a device with a time constant of 7 μs. We see that the value of the integral in equation (3.5) will increase – and hence δE will decrease – as we increase the upper limit of integration up to some frequency that is determined by the crossover between the thermal fluctuation NEP_{th} and the amplifier NEP_{amp}. Beyond this point, the contribution to the integral from further increasing the upper integration limit will diminish to zero.

The effect of negative electrothermal feedback is to shorten the time constant, which moves the crossover between the thermal fluctuation noise and the amplifier noise to higher frequency. This improves the energy resolution by increasing the frequency range over which the integral in equation (3.5) contributes to a decreased δE. Hence, provided we have access to sufficient measurement bandwidth, negative electrothermal feedback will improve the energy resolution of a superconducting bolometric calorimeter.

In chapter 1, we found that the noise equivalent power due to thermal fluctuation noise (NEP_{th}) in the isothermal regime is given by

$$NEP_{th}^{\ 2} = 4k_B T^2 G\,, \tag{3.6}$$

a result that is independent of electrothermal feedback. We compared different low-pass filters on the mixer IF output and selected 100 kHz as the bandwidth that gave the best

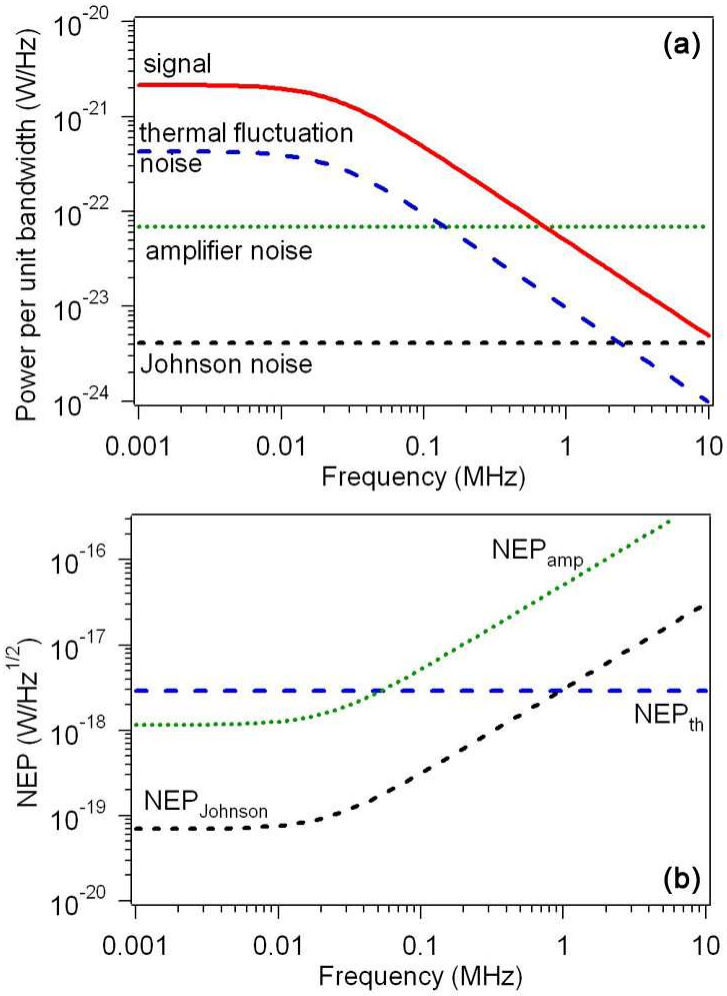

Figure 3.10. (a) Example of device signal and relevant noise contributions as a function of frequency for a device with τ = 7 μs. (b) Corresponding noise equivalent power as a function of frequency.

signal-to-noise. This frequency is approximately the crossover between NEP_{th} and NEP_{amp} for τ_{eff} = 3.7 μs. We can then estimate the predicted energy resolution by using the predicted thermal fluctuation NEP_{th} over the measurement bandwidth of 100 kHz. Using T = 0.30 K and G = 2.6 x 10^{-12} W/K based on (Wei 2008), we find from equation (3.6) NEP_{th} = 3.6 x 10^{-18} W/Hz$^{1/2}$. Using this in equation (3.5) and integrating from 0 to 100 kHz, we get a predicted energy resolution δE_{th} = 20 THz. This is close to the

experimental determination of the intrinsic energy resolution, $\delta E_{intrinsic} \approx 23$ THz, and hence we conclude that the intrinsic device performance is consistent with that expected from thermal fluctuation noise.

To approach the intrinsic device energy resolution in an experiment, the amplifier noise contribution must be decreased from its present value. If the total white noise contribution (amplifier noise plus Johnson noise) were decreased to 1 K, this would reduce δE_{amp} to 18 THz, which would yield $\delta E_{total} = 27$ THz for $\delta E_{intrinsic} = 20$ THz. In this case, the dominant contribution to the total energy resolution is the intrinsic device noise. This may seem difficult to achieve, but recent research in the area of parametric amplification (Castellanos-Beltran 2008, Bergeal 2008) makes a sub-Kelvin amplifier noise temperature a real possibility for future experiments.

The devices we have studied have a spectral resolution $\lambda/\delta\lambda \approx 1$ at 50 THz. To improve the resolution in future devices, we can reduce the Ti nanobridge volume or decrease T_c. A significant reduction in T_c would require the use of a different experimental system, so for the next generation of devices we plan to reduce the size of the Ti nanobridge. From equation (3.4), the energy resolution should scale as the square root of the active device volume. For a device with reduced Ti dimensions of 0.5 μm x 0.1 μm x 50 nm, the same values of T_c and dR/dT as the present device, and using the same 100 kHz measurement bandwidth, the expected intrinsic energy resolution is $\delta E_{intrinsic} = 3$ THz FWHM.

We next consider the effect of amplifier noise on the *total* energy resolution for this smaller volume device. We assume the device is voltage-biased, which is appropriate for $R_{shunt} = 3\ \Omega$. A change in resistance δR will result in a change in current δI given by

$\delta I/I = \delta R/R$, where I and R are the steady state values of the device current and resistance, respectively. We define the current responsivity as the change in current δI divided by the absorbed energy δE. For a hot electron bolometric detector, the current responsivity is given by

$$\frac{dI}{dE} = \frac{\left(\frac{\delta R}{R} I\right)}{\left(C_e \, \delta T\right)} = \frac{I}{R}\left(\frac{dR}{dT}\right)\frac{1}{C_e}. \qquad (3.7)$$

The electronic heat capacity C_e is proportional to the active device volume V. We assume R and dR/dT are independent of V. The Joule power I^2R from the bias current must heat the device to the same temperature (for a fixed T_c) and so should scale as V, and hence the bias current I should scale as $V^{1/2}$. Thus the responsivity dI/dE is proportional to $V^{-1/2}$.

The energy width due to amplifier current noise δI_{amp} is given by $\delta E_{amp} = \delta I_{amp}/(dI/dE)$. δI_{amp} is constant for a given device impedance (R_n is fixed at ≈ 50 Ω for efficient high frequency coupling). Hence δE_{amp} is proportional to $V^{1/2}$. From equation (3.1) we see that $\delta E_{intrinsic}$ is also proportional to $V^{1/2}$. Thus, if we achieve $\delta E_{amp} < \delta E_{intrinsic}$ for the present device, this will also hold for a smaller device with the same T_c using the same readout system. We conclude that amplifier noise should not prevent the experimental realization of a significantly improved energy resolution through the use of a smaller volume Ti device.

3.5 Conclusion

Using the fauxton characterization technique, we have demonstrated the feasibility of THz single-photon detection with a nanoscale Ti bolometric device. There remains,

however, a great deal of parameter space yet to be explored in these device characterizations. For example, we have not yet studied the dependence of the device performance on the bath temperature or the probe frequency. Future work will also include the characterization of devices with a reduced Ti volume, which are predicted to have a significantly improved total energy resolution.

Eventually, the goal is to compare fauxton detection to real photon detection. In fact, it is possible to perform both measurements in the same experimental system. This would allow for optimization of the device response using fauxtons prior to measurements with real photons. There are several reasons why the energy resolution for optical detection of real photons may not match that obtained with fauxtons. For example, photons might couple to the Nb contact near the Ti device. Hot electrons in the Nb could diffuse into the Ti, generating a signal that is smaller than would be obtained for direct photon absorption in the Ti. There is also a small probability that an excited photoelectron, or the energetic excitations that result in the Ti, will diffuse into the contacts before they can share their energy with other electrons and relax below the energy gap of the Nb. Hence the fauxton data represent an upper bound on the performance (lower bound on the energy resolution) of a real optical detector. In this way, the fauxton technique can be a useful tool not only for preliminary device characterization and optimization, but also for understanding detector non-idealities in real optical experiments.

Chapter 4

Bolometric Response of Individual Single-Walled Carbon Nanotubes

4.1 Introduction

With a diameter of ~nm and a length that can exceed 1 cm, the carbon nanotube is a highly one-dimensional (1D) material. Conceptually, it can be though of as a rolled-up sheet of graphene, a planar hexagonal lattice of sp^2-bonded carbon atoms. The geometry of this rolling is specified by two vectors, or chiral indices, which completely determine the intrinsic properties of the nanotube.

The nanotube band structure can be found by taking the band structure of graphene and applying appropriate periodic boundary conditions. Graphene is a semi-metal, with a dispersion relation that crosses the Fermi energy at only two inequivalent momentum points in the Brillouin zone (Charlier 2007). The application of periodic boundary conditions, known as the zone-folding scheme, quantizes the momentum of electrons in the circumferential direction, resulting in a discrete set of available momentum states. Depending on the chiral indices, the allowed momentum states of a

nanotube will either cross the Fermi energy, resulting in a metallic nanotube, or will miss the Fermi energy, resulting in a semiconducting nanotube. Two-thirds of all possible chiral indices produce semiconducting nanotubes, and one-third produce metallic nanotubes.

Semiconducting nanotubes are predicted to have a band gap ~eV that scales as d^{-1}, where d is the tube diameter. Metallic nanotubes have a linear dispersion relation of energy versus momentum at low energies (<< eV). The two allowed momentum points at the Fermi energy, combined with spin degeneracy, result in four quantum channels. From the Landauer-Büttiker formalism, ballistic transport through a single quantum channel has a two-terminal resistance $R_q = h/e^2 \approx 25.8$ kΩ (McEuen 2002). For ballistic transport through a nanotube with ideal contacts, the resistance is thus $R_q/4 \approx 6.4$ kΩ. The presence of scattering within the nanotube or imperfect contacts results in a higher resistance. In this case, the resistance is $R = (h/4e^2)(L/\ell_e) + R_c$, where L is the nanotube length, ℓ_e is the electron mean free path, and R_c is the total contact resistance, equal to $R_q/4$ plus any additional resistance due to non-ideal contacts (Park 2004, Purewal 2007).

Strain induced by the curvature of a nanotube can create a small bandgap in what was predicted in the zone-folding scheme to be metallic. These are sometimes known as quasi-metallic nanotubes, whose small bandgap (< 100 meV) is predicted to be proportional to d^{-2}. Nanotubes with equivalent chiral indices are protected from this strain-induced gap by symmetry, and are predicted to be truly metallic (Charlier 2007).

Since its discovery in multi-walled form in 1991 (Iijima) and single-walled form in 1993 (Bethune, Iijima), the carbon nanotube has been the subject of a tremendous body of research, which we will not attempt to summarize here. For further background on

carbon nanotubes, the reader is referred to the book edited by Dresselhaus, Dresselhaus, and Avouris (2001) and the review article by Charlier, Blase, and Roche (2007).

In the present work, we are interested in Joule heating in individual single-walled carbon nanotubes (SWNT). Nanotubes can support extremely large current densities – in excess of 10^9 A/cm^2 (Yao 2000), which is significantly larger than a copper wire – which makes them attractive for electronic device applications. These large current densities lead to significant Joule heating. As a result, self-heating effects are important in determining the performance of nanotube-based devices. These self-heating effects also provide a tool for studying the non-equilibrium electron properties of this unique one-dimensional conductor. We demonstrate how the nanotube's temperature-dependent resistance, which gives its bolometric response, can be used as an electrical probe of the nanotube electron temperature. Measurements of the electron temperature as a function of dissipated power are used to study the inelastic processes by which the electron system loses energy to the environment.

Several previous works have studied Joule heating in individual SWNT, both on-substrate and suspended, at room temperature and above (Park 2004, Pop 2005, Pop 2006, Pop 2007, Deshpande 2009). We focus on a high-quality individual SWNT on an electrically insulating substrate in the low temperature regime (4 - 250 K). Lower temperatures result in greater thermal decoupling of the electron and phonon systems, facilitating the study of low energy inelastic processes of the electron system. By studying nanotube sections of different lengths, we are able to distinguish the contributions to the energy relaxation of the electron system from electron-phonon coupling and from hot electron outdiffusion.

4.2 DC characterization

The nanotubes studied in this work were grown and patterned by Meninder Purewal in the group of Prof. Philip Kim at Columbia University. The sample we have studied is the same sample referred to as M1 in Purewal *et al.* (2007). The nanotubes are grown using chemical vapor deposition on a degenerately doped silicon (Si) substrate with a 500 nm thick oxide (SiO_2). The doped Si substrate is used as a global back gate. The growth procedure produces nanotubes that are up to millimeters in length (Hong 2005). Palladium (Pd) electrodes are fabricated at various separations along an individual nanotube. Pd is used because its work function is closely matched to that of the nanotube, and experimentally it has been found to produce high quality (low resistance) contacts (Javey 2003, Mann 2003). Further details on sample growth and fabrication can be found in Purewal (2008).

We report two-terminal electrical measurements of nanotube samples with lengths of 2, 5, 20 and 50 μm, all of which are separately-contacted sections of the same nanotube (figure 4.1). The diameter of this nanotube is 2.0 +/- 0.2 nm, measured with an atomic force microscope, and the saturation current was measured to be < 30 μA, ensuring that it is an individual single-walled tube (Purewal 2007). The nanotube chirality is not known.

The dependence of the dc resistance on the back gate voltage is shown in figure 4.2 for the 20 μm nanotube at bath temperatures of 4 K, 77 K, and 295 K. We see that this is a quasi-metallic nanotube with a small bandgap. The hysteresis in the gate-dependent resistance has been attributed to charge trapping in the SiO_2 dielectric (Fuhrer 2002, Radosavljevic 2002). The resistance is a minimum for large negative gate voltages,

indicating slight p-type behavior. This p-type behavior is attributed to the mismatch between the work functions of the nanotube and the Pd contacts (Nosho 2006). All subsequent measurements described in this chapter were conducted at a back gate voltage of -30 V, where the two-terminal conductance is a maximum and is insensitive to small variations in the gate potential.

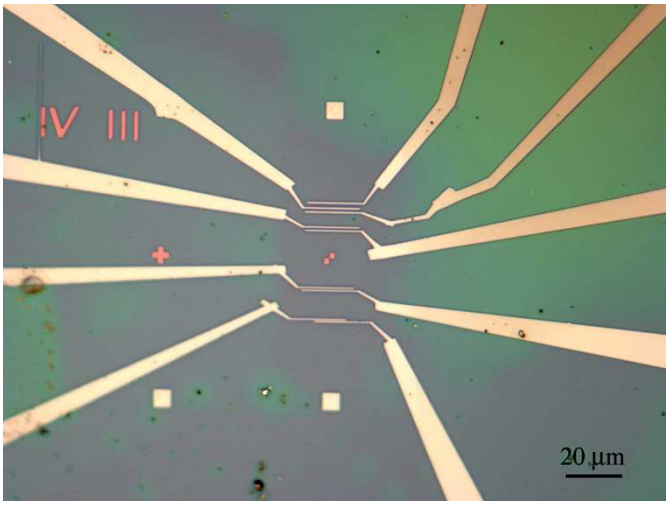

Figure 4.1. Optical image of one section of the nanotube sample showing the Pd leads. The nanotube (not visible) is oriented vertically in the center of the image.

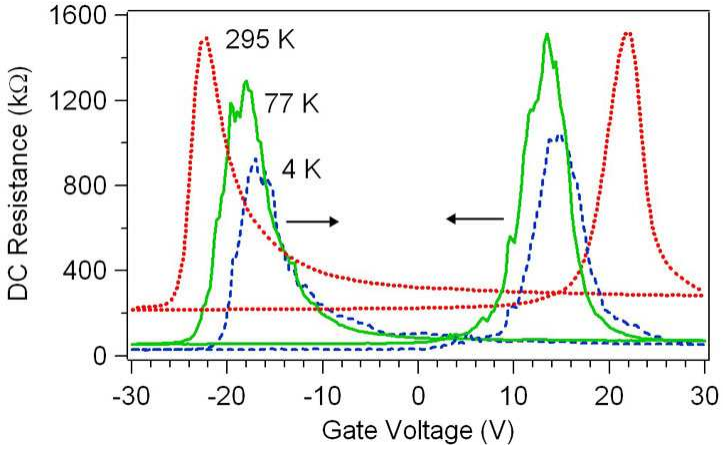

Figure 4.2. Two-terminal resistance of 20 µm nanotube as a function of backgate voltage at different bath temperatures. The gate voltage is swept in both directions, as indicated by the arrows, to show hysteresis.

The dc resistance as a function of temperature for all four nanotube lengths measured with a small dc bias current I = 300 nA is presented in figure 4.3. These measurements indicate a temperature-independent contact resistance $R_c \approx 8$ kΩ, close to the quantum-limited contact resistance of $R_q/4 = h/4e^2 \approx 6.4$ kΩ, and an internal resistance $R_{int} \approx 1$ kΩ/μm at 4 K that increases to ≈ 12 kΩ/μm at 300 K, consistent with the results of Purewal *et al*. (2007).

In the insets of figure 4.3 we plot the measured dc resistance $R = V/I$ as a function of the dc bias current I at a bath temperature T_{bath} = 4.2 K. For measurements at $T_{bath} < 20$ K, a local maximum in R is seen at zero bias current. This zero-bias anomaly (ZBA) has been discussed in a number of previous works, and has alternatively been described in terms of a reduced density of states for tunneling into a Luttinger liquid (Yao 2000, Gao 2004) or Coulomb blockade (Kanda 2004, Dayen 2005). In either case, the ZBA is related to non-ideal contacts. At T_{bath} = 4.2 K, as the bias current is increased above 0.5 μA, the contacts recover ohmic behavior and R displays a monotonic increase with increasing bias current. We measure up to I = 5 μA, which is high enough to show significant heating effects but still well below the saturation current of ≈ 25 μA (Yao 2000).

The increase in R with increasing I is attributed to Joule heating of the electron system in the nanotube. We assume that, away from the ZBA, the non-equilibrium dc resistance (finite bias current) and the equivalent equilibrium dc resistance (small bias current) correspond to the same average electron temperature. Hence the *R(T)* data can be used to assign a temperature to the electron system in the *R(I)* data. To test this

assumption, we use Johnson noise to directly determine the electron temperature as a function of the bias current, as described in the next section.

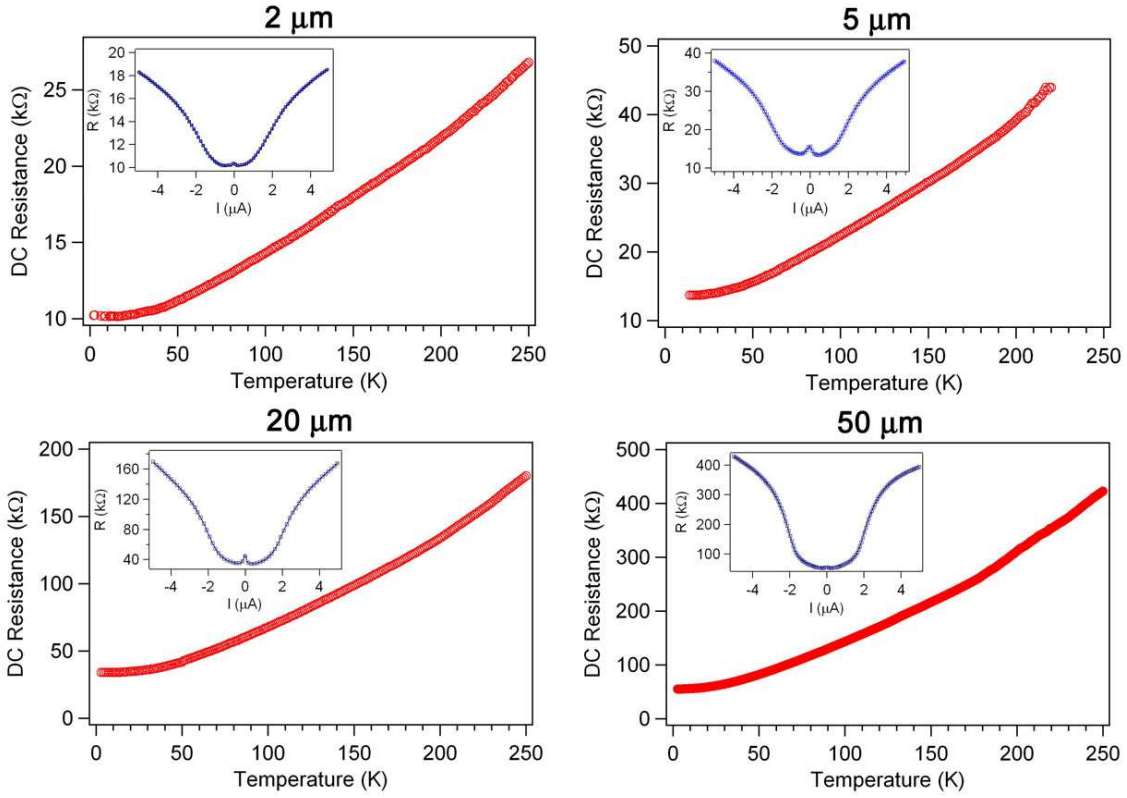

Fig. 4.3. DC resistance of as a function of temperature measured with a dc bias current of 300 nA for each of the four nanotube lengths. Insets show dc resistance as a function of bias current at a bath temperature of 4.2 K.

4.3 Johnson noise

The Johnson noise temperature T_J for a device with a non-uniform temperature is given by $T_J = \int_0^L T_e(x)R(x)dx \Big/ (R_{int}L)$, where $T_e(x)$ and $R(x)$ are the position-dependent electron temperature and resistance, respectively, L is the nanotube length, and R_{int} is the

total internal resistance of the nanotube. For a uniform temperature and no contact resistance, this becomes $T_J = T_e$.

To determine the electron temperature profile in the nanotube, we use the one-dimensional steady-state heat flow equation,

$$V \frac{\partial}{\partial x} \kappa_{diff} \frac{\partial T_e}{\partial x} + P_{dc} - \beta (T_e^{\,p} - T_b^{\,p}) = 0 . \tag{4.1}$$

The first term is due to electron diffusion, with κ_{diff} the thermal conductivity due to diffusion, V the nanotube volume, and x the position along the axial direction of the nanotube. P_{dc} is the Joule power dissipated by the dc bias current. The third term is the cooling power due to electron-phonon coupling, where β and p are constants determined experimentally using the data from the longest nanotubes, for which end effects should be negligible (discussed in the next section). The contact resistance is incorporated via the boundary condition

$$\kappa_{diff} A \frac{\partial T_e}{\partial x}\bigg|_{x=\pm L/2} = G_c \left(T_e\big|_{x=\pm L/2} - T_{bath} \right) \tag{4.2}$$

where G_c is the thermal conductance at the contacts, given by the Wiedemann-Franz law, $G_c = \mathscr{L} T_{con}/R_c$, with $\mathscr{L}$ the Lorenz number; R_c the contact resistance at each contact, ≈ 4 kΩ; and T_{con} the effective contact temperature. We assume for now that $T_{con} = T_{bath}$.

We determine $\kappa_{diff} = G_{diff}(L/A)$, with A the nanotube cross-sectional area and L the length, using the Wiedemann-Franz law, $G_{diff} = \mathscr{L} T_e/R_{int}$, with $R_{int} = (R - 8\ \text{k}\Omega)$. In the temperature range 50 – 200 K, R is approximately linear in T, and we make the approximation $R_{int} = \alpha T$ and determine α from a fit of this function to the $R(T)$ data in this temperature range. This results in a temperature-independent κ_{diff}. The Joule power is

$P_{dc} = I^2 R_{int}$, where we assume that the power dissipated in the contacts does not heat the nanotube. Equation (4.1) can then be numerically solved for $T_e(x)$ with the boundary condition of equation (4.2).

We find that most of the temperature increase relative to the bath temperature is across the contacts. The temperature variation along the length of the nanotube is smaller than the temperature change at the contacts for all nanotube lengths. As an example, we plot in figure 4.4 the calculated temperature profile for the 20 μm nanotube with a bias current of 2 μA at T_{bath} = 4.2 K. The relatively small temperature variation along the length of the nanotube results from the thermal conductance from electron diffusion over the electron-phonon inelastic scattering length being much larger than the contact thermal conductance, as we will see in the next section. Based on this temperature profile, we make the simplifying assumption that the local temperature and the average temperature can be treated as equivalent.

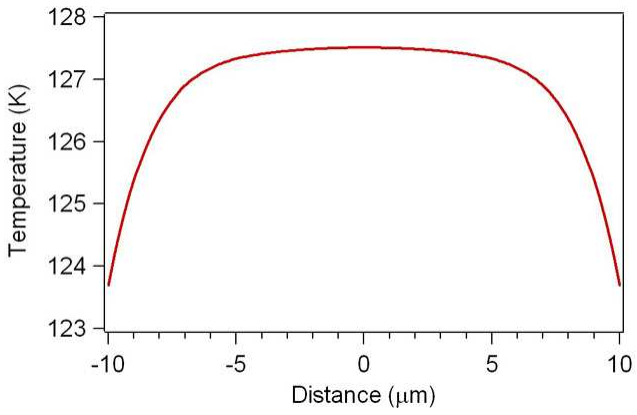

Figure 4.4. Calculated electron temperature profile for 20 μm nanotube with 2 μA bias current at T_{bath} = 4.2 K.

To measure the Johnson noise, we employ a differential measurement technique with an alternating bias current that switches between 0 μA and a finite current at 83 Hz. We measure at bath temperatures of 4.2 K and 77 K. At T_{bath} = 4.2 K, we use 1 μA rather than 0 μA in order to avoid the ZBA feature. The noise is measured with a 50 Ω microwave amplifier through a bandpass filter with a bandwidth of 10 MHz centered at approximately 50 MHz. The output is coupled to a diode, and the diode response is read on a lock-in amplifier synchronized to the 83 Hz biasing signal. In converting the measured noise power difference to a change in noise temperature, we account for the change in the device resistance with the change in bias current. This affects both the coupling efficiency and the emitted amplifier noise reflected by the device. (The noise emitted by the amplifier input is found to be slightly less than half the measured amplifier noise temperature.) We assume that only the nanotube internal resistance is heated by the bias current and that the contact resistance is temperature-independent (Purewal 2007). We also assume that the nanotube is longer than the electron-phonon inelastic scattering length, and hence the contribution from shot noise is negligible (Steinbach 2006). We will see in section 4.4 that this assumption is reasonable at least for the 5 μm and longer nanotubes.

We plot in figure 4.5 the relative temperature increase determined from the Johnson noise measurement of the 5 μm nanotube at both T_{bath} = 4.2 K and 77 K. The standard deviation is approximately the same size as the data points. Also plotted is the temperature increase inferred from the dc *R(T)* and *R(I)* data. We see good agreement between the temperature increases determined using these two approaches. We conclude

that, away from the ZBA feature, the dc resistance is a measure of the average electron temperature for both the equilibrium and the non-equilibrium cases.

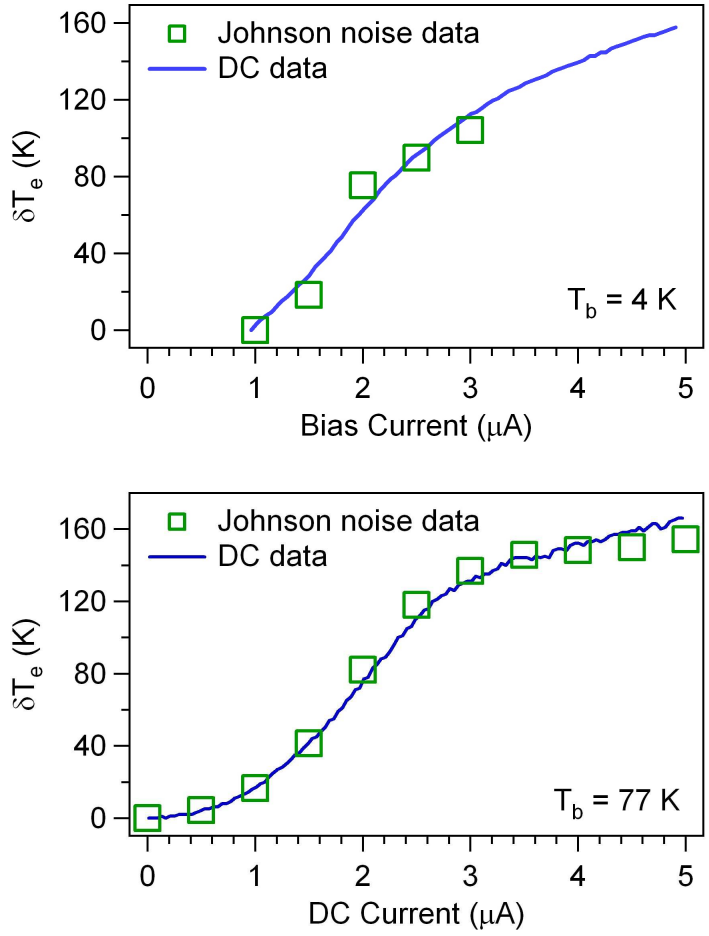

Figure 4.5. Increase in the average electron temperature δT_e of the 5 μm nanotube device at T_{bath} = 4.2 K (top) and T_{bath} = 77 K (bottom) measured via Johnson noise. Also plotted is the increase in electron temperature inferred from dc *R(T)* and *R(I)* data.

4.4 Thermal conductance

We next describe how the dc data are used to determine the thermal conductance for cooling of the electron system. The dc resistance at each value of *I* is converted to an electron temperature using the measured *R(T)*. *I* is then converted to Joule power *P* =

$I^2(R - R_c)$, where we subtract the contact resistance R_c = 8 kΩ because the power dissipated by the contact resistance is in the Pd contacts, which we assume act as thermal reservoirs. Differentiating the Joule power with respect to the electron temperature T_e yields the thermal conductance for cooling of the electron system in the nanotube, $G = dP/dT_e$. This is plotted as a function of T_e in figure 4.6 for the all four nanotube lengths. Although we measure at T_{bath} = 4.2 K, we only determine G for T_e > 20 K because of the ZBA feature.

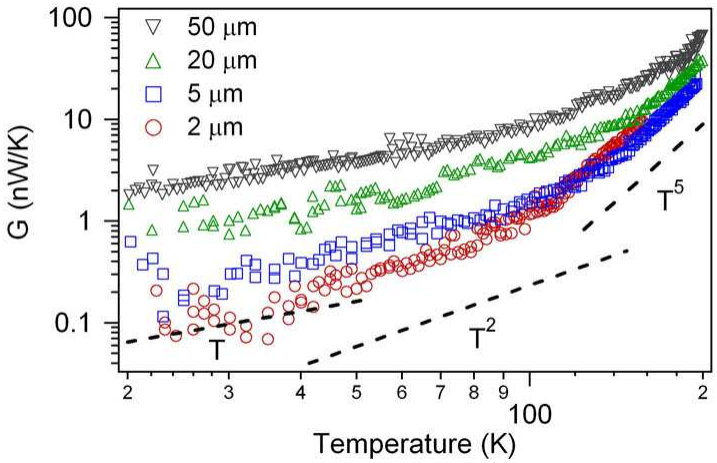

Figure 4.6. Thermal conductance as a function of average electron temperature for 2, 5, 20 and 50 μm nanotubes at a bath temperature of 4.2 K. Dashed lines illustrate T, T^2 and T^5 dependencies.

The time constant for cooling of the electron system is $\tau = C_e/G$. The electronic heat capacity C_e for a metallic nanotube with one partially filled band is calculated by Benedict *et al*. (1996) for $T_e << hv_F/(2\pi k_B r)$ as $C_e = 8\pi^2 L k_B^2 T_e/(3hv_F)$, where r is the nanotube radius. In figure 4.7, we convert the measured G into the thermal time constant using this calculated C_e. We see that the thermal time constant of the nanotube electron system is extremely fast, < 10 ps, even at low temperature.

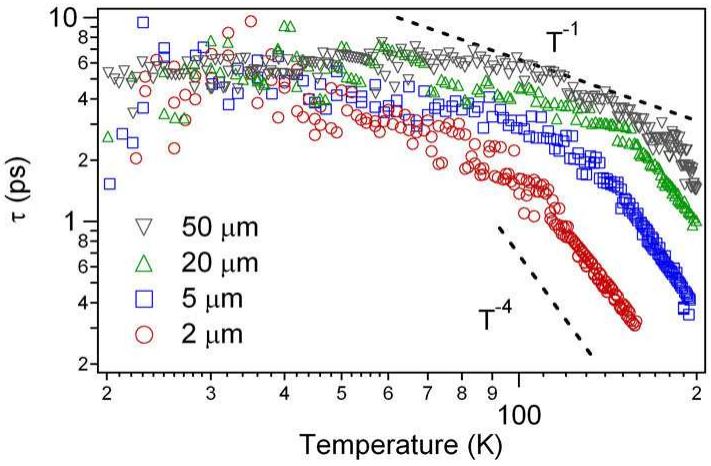

Figure 4.7. Time constant for cooling of the electron system determined from the measured thermal conductance *G* and the calculated electronic heat capacity C_e.

In order to understand the different temperature regimes observed in the thermal conductance data, we consider the thermal model for the nanotube electron system that is illustrated in figure 4.8. At low energies, there are two parallel cooling pathways for the electron system. The first is cooling via inelastic scattering with acoustic phonons, with a thermal conductance $G_{e\text{-}ph}$. If hot phonons do not leave the nanotube before they share their energy with another electron, then this will add a thermal conductance in series with $G_{e\text{-}ph}$, which we call the phonon thermal conductance G_{ph}. The parallel cooling pathway is the outdiffusion of hot electrons into the contacts. This is represented by a diffusion thermal conductance G_{diff} in series with a contact thermal conductance G_c. If electrons exceed some threshold energy, they can also emit optical phonons. We describe this as an additional parallel cooling pathway with a thermal conductance G_{op}. The total thermal conductance G is thus

$$G = \left(G_{e-ph}{}^{-1} + G_{ph}{}^{-1}\right)^{-1} + \left(G_{diff}{}^{-1} + G_c{}^{-1}\right)^{-1} + G_{op}\,. \qquad (4.3)$$

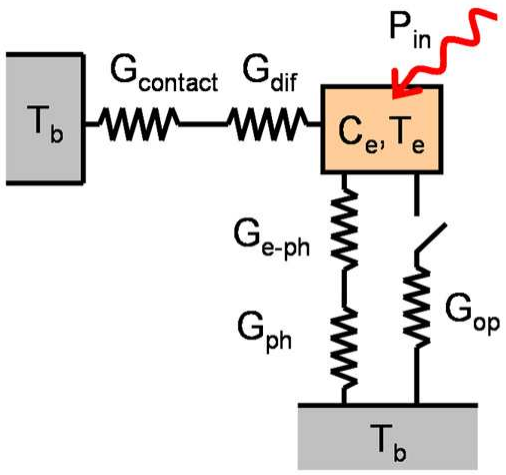

Figure 4.8. Thermal model for cooling of the nanotube electron system.

At temperatures above approximately 120 K, we observe that *G* increases rapidly with increasing temperature, approximately as T_e^5. The onset of this behavior moves out to higher temperature for longer nanotube lengths. This rapid increase in *G* at higher bias currents is consistent with the onset of scattering via surface polar phonons (SPPs), which have a predicted threshold energy of 50 meV in silicon dioxiode (Petrov 2006, Perebeinos 2009, Rotkin 2009). SPPs are collective polarization modes on the surface of a dielectric, analogous to plasmon modes on a metal surface. Once the potential difference between inelastic scattering events exceeds 50 meV, electrons have a high probability of losing energy by scattering with a SPP in the silicon dioxide substrate. The nanotube electron mean free path ℓ_e can be determined from $\ell_e = (6.5\ \text{k}\Omega)/(R_{int}/L)$ (Park 2004, Purewal 2007).The mean free path determined in this way at $T_e \approx 120$ K is approximately 2 μm. The potential drop over a length of 2 μm at the onset of the T^5 behavior is ≈ 30 mV for all four lengths. Additionally, thermal broadening of the energy

distribution is approximately $k_B T_e \approx 10$ meV at $T_e = 120$ K. By comparison, inelastic scattering within the nanotube has a predicted threshold energy of approximately 160 meV for zone boundary phonons and 200 meV for optical phonons (Park 2004). These threshold energies are too large to describe the data, and only the emission of surface polar phonons is consistent with the observed behavior above 120 K.

From 50 K to 120 K, G scales approximately as T_e^2. In this temperature and current range, optical phonons should not be excited. Acoustic phonon scattering has a contribution $G_{e\text{-}ph} \propto L$, with L the nanotube length. Outdiffusion has a contribution from one dimensional diffusion, $G_{diff} \propto L^{-1}$, in series with a contribution from the contact resistance, G_c. We use the Wiedemann-Franz law to determine G_{diff}, where the effective diffusion thermal conductance is a factor of $2^7/\pi^2 \approx 13$ larger than the end-to-end diffusion thermal conductance $\mathscr{L}T/R_{int}$ when we consider the temperature distribution along the nanotube with cooling out both ends (Burke 1997). We also assume G_c is determined by the Wiedmann-Franz law, using a resistance of 2 kΩ for the two 4 kΩ contacts in parallel, where the temperature used to determine G_c is T_{con}.

To determine the contribution of G_{ph}, we compare the measured G in this regime for the longer nanotube lengths, in which the contribution from outdiffusion is expected to be negligible, to previous experimental determinations of the phonon thermal conductance. Maune *et al.* (2006) and Pop *et al.* (2007) determine a phonon interface thermal conductance per unit length $g_{int} \approx 0.2$ - 0.3 W/Km from electrical breakdown measurements in air ($T \approx 900$ K at breakdown) on sapphire and oxidized silicon substrates, respectively. Shi *et al.* (2009) find $g_{int} \sim 0.01$ - 0.06 W/Km for a single-walled nanotube on an oxidized silicon substrate near room temperature using a scanning

thermal microscope to determine the local lattice temperature in a Joule-heated nanotube. The phonon interface thermal conductance scales linearly with the phonon specific heat and hence with the lattice temperature (Prasher 2005). If we scale these experimental values for g_{int} to a phonon temperature ≈ 10 K, we get $g_{int} \sim 10^{-3}$ W/Km. For T_e between 50 and 120 K and $L \gtrsim 5$ μm, our measurement yields $g \approx 2.4 \times 10^{-8} T_e^2$ W/Km for the longer nanotube lengths. For T_e = 50 K, this is $g \approx 6 \times 10^{-5}$ W/Km. This is significantly smaller than the estimated phonon boundary conductance per unit length g_{int}, and hence our experimentally determined thermal conductance in this regime should be dominated by electron-acoustic phonon scattering, and not by the phonon thermal conductance.

We then we fit equation (4.3) to the measured data from the four nanotube lengths at different temperatures, neglecting G_{ph} and G_{op} and using $G_{e\text{-}ph}$ and T_{con} as fitting parameters. We impose the requirements that $G_{e\text{-}ph} \propto L$ and T_{con} is independent of L. As an example, we plot in figure 4.9 the measured value of G for all four device lengths at T_e = 80 K, as well as a fit to equation (4.3). From this fit, we extract $T_{con} \approx 18$ K and $G_{e\text{-}ph} = (1.5 \times 10^{-4})L$ in units of W/K, where L is the nanotube length in meters. The fitting gives a good determination of $G_{e\text{-}ph}$, but the value of T_{con} can vary by as much as 50% while still achieving reasonable agreement with the measured data. Comparing fits at different temperatures in the range of 50 - 120 K, we find $G_{e\text{-}ph} \approx (24 \times 10^{-9} L T_e^2)$ W/K, where L is in meters.

This enables a determination of the constants β and p in equation (4.1), as $G_{e-ph} = \frac{d}{dT_e}\left[\beta(T_e^{\,p} - T_b^{\,p})\right]$. We find p = 3 and $\beta = (8L)$ nW/K^3. Similarly, the time constant determined in this regime should be the electron-acoustic phonon inelastic scattering time. Using the calculated C_e, we find $\tau_{e\text{-}ph} \approx (394/T_e)$ ns.

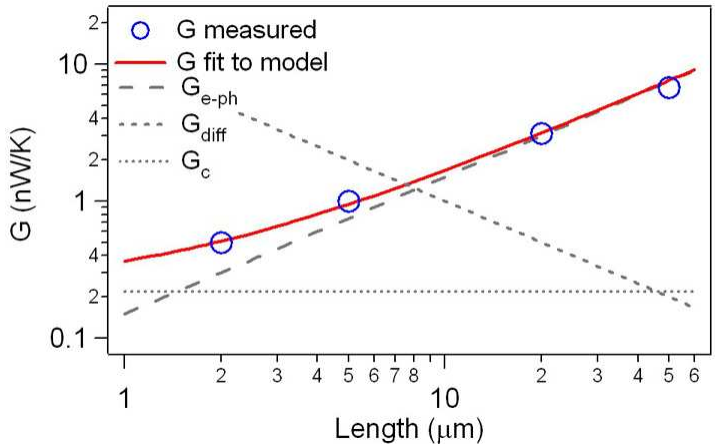

Figure 4.9. Measured G and fit to equation (4.3) for T_e = 80 K. Also shown are the values of $G_{e\text{-}ph}$, G_{diff} and G_c from the fit.

The contribution to the cooling from the outdiffusion of hot electrons becomes significant for $L \lesssim 1$ μm, although the exact crossover length depends on the electron temperature. For these shorter lengths, we find $G \approx G_c$. Thus, for short nanotube devices, the contact resistance is critical in determining the temperature rise of the electron system due to Joule heating.

For T_e below approximately 50 K, the temperature-dependence of thermal conductance becomes weaker than T^2, with $G \sim (1.6 \times 10^3\ L\ T_e)$ nW/K. This corresponds to an approximately temperature- and length-independent thermal time constant $\tau \sim 6$ ps. This may be due to G_{ph}, as the phonon interface thermal conductance is predicted to scale linearly with T (Prasher 2005). Because of the diminishing dR/dT at these lower temperatures, the signal-to-noise in the thermal conductance is also diminished.

4.5 Differential resistance

In the absence of non-thermal nonlinearities, the differential resistance *dV/dI* can be related to the dc resistance $R = V/I$ through the thermal conductance *G*. We start by differentiating Ohm's law,

$$dV = RdI + IdR = RdI + I\left(\frac{dR}{dT}\right)dT = RdI + \frac{I}{G}\left(\frac{dR}{dT}\right)dP\,, \tag{4.4}$$

where we have used the definition $G = dP/dT$. We differentiate $P = IV$ to get $dP = VdI + IdV$. Using this expression for *dP* in equation (4.4) and solving for *dV/dI*, we find

$$\frac{dV}{dI} = R\frac{1+\frac{P}{RG}\frac{dR}{dT}}{1-\frac{P}{RG}\frac{dR}{dT}}\,. \tag{4.5}$$

We can use this relationship to test our determination of *G*. In figure 4.10 we plot for the 5 μm nanotube at T_{bath} = 4.2 K the differential resistance calculated from equation (4.5) using the experimentally determined *G* as well as measured values of *R*, *P*, and *dR/dT*. *dV/dI* is only calculated for T_e > 20 K because of the ZBA feature, as discussed

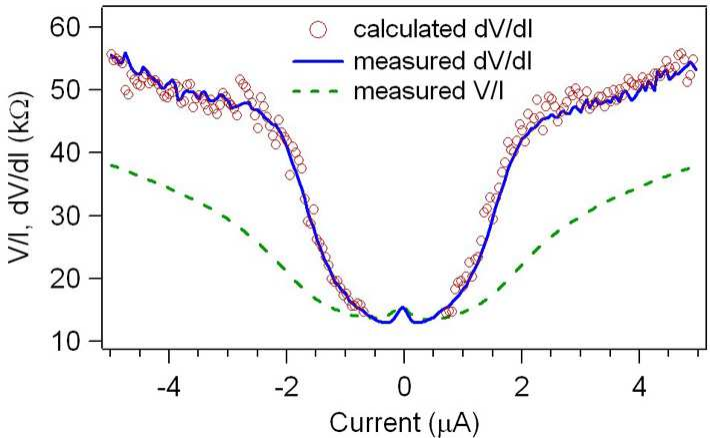

Figure 4.10. Measured and calculated differential resistance, as well as measured dc resistance, for 5 μm nanotube at T_{bath} = 4.2 K.

previously. In this calculation, we assume that only R_{int} is heated, and that R_c is a temperature-independent ohmic resistor. We also plot the measured dV/dI and $R = V/I$ as a function of the dc bias current. The excellent agreement between the measured and calculated values of dV/dI, with no adjustable parameters, supports the validity of the determination of G.

4.6 High frequency response

It has been proposed that a carbon nanotube could be used as a bolometric heterodyne mixer with a very wide IF bandwidth (Yngvesson 2005). In section 4.4, we saw that the thermal time constant for a single-walled nanotube is extremely fast, < 10 ps, consistent with that proposal. In previous studies of the microwave response of carbon nanotubes, the measured response has been dominated by the electrical (non-thermal) contact nonlinearity (Rodriguez-Morales 2006). Those experiments were performed on nanotubes with significantly higher contact resistance than the samples we have studied. Measurements of the response to THz frequency signals have seen evidence for a bolometric response in nanotube bundles with relatively high contact resistance (Tarasov 2007, Fu 2008). The contribution of the contact nonlinearity is believed to be diminished at these higher frequencies because the contact barrier has an effective parallel capacitance. There has also been a report of a purely bolometric response in a suspended large-area (~mm^2) mat of carbon nanotubes, but with a very slow time constant, $\tau \approx 50$ ms (Itkis 2006).

In order to study the high frequency response of our nanotube samples, we have performed microwave heterodyne mixing measurements using the same experimental

system described in section 2.3. Because the chip was not designed for high frequency coupling, we performed these measurements with ~100 MHz input frequencies. However, with proper coupling structures, the same measurements could be performed at GHz frequencies. The technique is similar to that described in section 2.3, although this measurement was performed with a dc current bias rather than a voltage bias.

In chapter 1, we found that the low-frequency bolometric responsivity $S(0) = I(dR/dT)/G$, where I is the dc bias current and G is the thermal conductance. With electrothermal feedback, G is replaced by $G_{eff} = G \pm I^2(dR/dT)$ for a voltage or current bias, respectively. More generally, we can define G_{eff} for a device with resistance R that sees a load resistance R_L as $G_{eff} = G + I^2(dR/dT)(R-R_L)/(R+R_L)$. For a derivation of this result, see Galeazzi and McCammon (2003). The low-frequency responsivity is then

$$S(0) = \frac{\frac{I}{G}\left(\frac{dR}{dT}\right)}{1+\left(\frac{I^2}{G}\frac{dR}{dT}\right)\left(\frac{R-R_L}{R+R_L}\right)} \tag{4.6}$$

where $R = V/I$. In this measurement, R_L is the 50 Ω amplifier input impedance. In figure 4.11 we plot the responsivity as a function of the dc bias current at T_{bath} = 4.2 K. In this data, we have corrected for the coupling loss due to the large impedance mismatch between the device and the amplifier. As before, we assume that only the internal resistance is heated, and R_c is a temperature-independent ohmic resistor. Also plotted is the measured noise floor, which is not flat because the device impedance, and hence the coupling efficiency, changes with the bias current. We also plot the responsivity calculated from equation (4.6) using the thermal conductance from section 4.4. We do not determine the calculated responsivity near zero bias current because of the ZBA, as

discussed previously. We note that there are no adjustable parameters in this calculated responsivity.

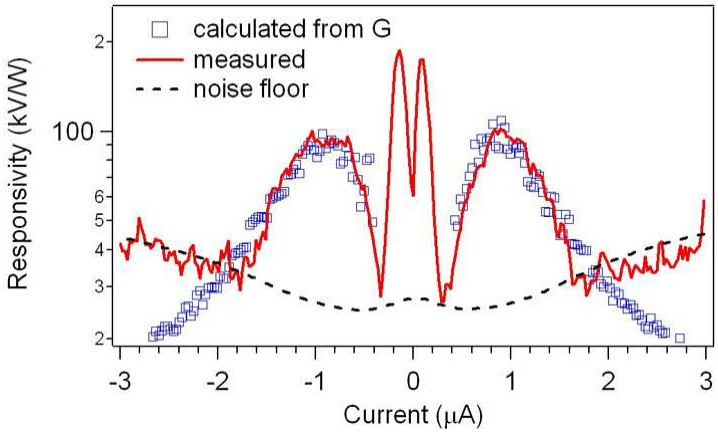

Figure 4.11. Responsivity from microwave heterodyne mixing measurement, along with responsivity calculated using equation (4.6), at T_{bath} = 4.2 K. Also plotted is the experimental noise floor.

The response is approximately symmetric between positive and negative bias current, and we observe two distinct pairs of peaks. The outer pair of peaks is in excellent agreement with the calculated bolometric responsivity using the experimentally determined thermal conductance. The inner set of peaks is aligned with the low-bias ZBA feature, and we attribute these to the contact-related electrical nonlinearity and not to a bolometric mechanism. In measurements above T_{bath} = 20 K, only the outer set of peaks are seen.

Now that we have determined the bolometric responsivity and the thermal conductance, we can calculate the predicted output noise temperature due to thermal fluctuation noise, as discussed in section 1.4. We can then determine if this noise source makes a significant contribution to the measured noise of section 4.3. The largest noise temperature due to thermal fluctuation noise corresponds to the largest bolometric

responsivity, and is found to be $T_{th} \approx 3$ K. This value is within the experimental uncertainty of the noise measurement of section 4.2, and hence the contribution from thermal fluctuation noise does not alter the results of that section.

The heterodyne response arises from the I-V nonlinearity, and hence is proportional to the second derivative of the I-V curve. This is true regardless of the physical mechanism for the nonlinearity. To calculate the responsivity from the I-V curve, we start by taking the Taylor expansion of the current as a function of voltage up to second order, $I(V_0+\delta V) = I(V_0) + (dI/dV)\delta V + (1/2)(d^2I/dV^2)(\delta V)^2$, where V_0 is the equilibrium bias voltage and δV is small voltage change from a high frequency input signal. We then take the time-average of the current change $<\delta I> = <I(V_0+\delta V)-I(V_0)> = (1/4)(d^2I/dV^2)V_{rf}^2$, where $(\delta V)^2 = V_{rf}^2/2$ with V_{rf} the high frequency input voltage. The current responsivity, in units of A/W, is then $S_I = <\delta I>/P$, where the high frequency input power $P = (V_{rf}^2/2)/(dV/dI)$, and thus

$$S_I = \frac{1}{2}\left(\frac{d^2I}{dV^2}\right)\left(\frac{dV}{dI}\right). \tag{4.7}$$

The voltage responsivity, in units of V/W, is $S_V = S_I\,(dV/dI)$, or

$$S_V = \frac{1}{2}\left(\frac{d^2I}{dV^2}\right)\left(\frac{dV}{dI}\right)^2. \tag{4.8}$$

In figure 4.12 we plot S_V determined from equation (4.8) using the measured I-V curve, along with the measured S_V for comparison. The calculated S_V clearly contains both sets of response peaks, the bolometric response at higher bias current and the contact (ZBA) response at lower bias current. The calculated contact response is consistent with the measured contact response. The bolometric response calculated from equation (4.8) is

larger than the measured response and the calculated response using equation (4.6). This is because the measured heterodyne mixing response is at ~10 MHz, where the device is approximately voltage-biased by the 50 Ω amplifier input impedance. The calculation using the current-biased dc I-V curve does not capture the electrothermal feedback that is present in the heterodyne mixing measurement. The non-thermal contact response, however, is unaffected by electrothermal feedback.

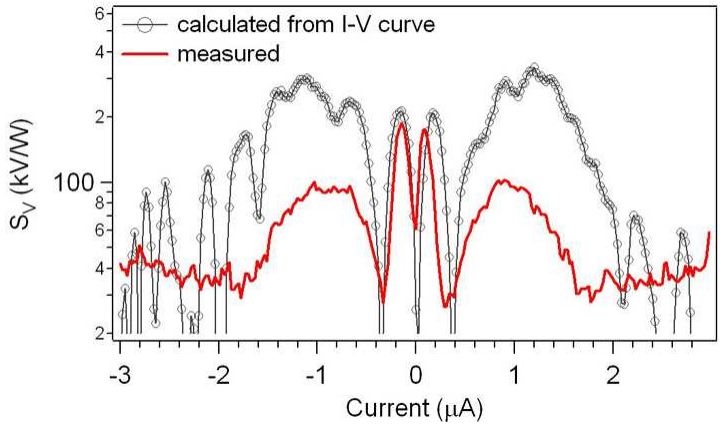

Figure 4.12. Responsivity calculated from the measured I-V curve as a function of bias current for the 5 μm nanotube at T_{bath} = 4.2 K. Also plotted is the measured responsivity for comparison.

The measured bolometric responsivity is very large, ~ 10^5 V/W. This is similar to the best responsivity obtained with the superconducting niobium microbolometers discussed in chapter 2. Taking advantage of the extremely fast thermal response, however, will require readout with a 50 Ω high frequency amplifier. In this case, the measured responsivity will be diminished by the coupling efficiency, which is ~10^{-2} for the lowest resistance (shortest) nanotube samples, and is smaller for longer nanotubes. A resonant impedance transformer could be used to avoid this coupling loss, but this is only

practical over a narrow frequency range and could not make use of the full device bandwidth. Using an array of nanotubes to decrease the device impedance can improve the coupling (Rutherglen 2008), but this will also decrease the *dR/dT* and hence the responsivity.

For these reasons, it seems unlikely that the nanotube bolometer will supplant the superconducting bolometer for high-sensitivity detection. In applications requiring very large output bandwidths, the nanotube bolometer might prove to be a competitive detector technology. There remain, in any case, significant issues involving the reproducibility and reliability of nanotube device fabrication that need to be solved before nanotube bolometers – or most other nanotube-based devices – can become a practical technology.

4.7 Conclusion

We have shown how experimental techniques developed for characterizing bolometric detectors can be employed to study inelastic processes in a single-walled carbon nanotube. In particular, we demonstrate that simple dc heating measurements can be used to determine the thermal conductance for cooling of the electron system. This technique requires a nanotube with ohmic contacts. Our nanotubes have such contacts for electron temperatures above 20 K. By comparing nanotube sections of different lengths, we are able to distinguish between the contribution to the thermal conductance from cooling due to electron-phonon coupling and from the outdiffusion of hot electrons. We also see evidence for strong cooling at higher bias currents from electrons coupling directly with surface polar phonons in the insulating silicon dioxide substrate.

A detailed understanding of the relaxation of the electron system is important for many proposed applications of nanotube electronics, including the use of nanotubes as extremely fast bolometric detectors. It is also relevant to our recent proposal to use the THz bolometric response as a tool to study high frequency charge excitations in a single-walled nanotube (Santavicca *Proc. IRMMW* 2008). If an antenna-coupled nanotube is used in place of the antenna-coupled superconducting bolometer in the THz spectrometer described in chapter 2, the power coupled to the nanotube, and hence its bolometric response, will be a maximum when the input frequency corresponds to a multiple of a half-wave resonance on the length of the nanotube. These resonances can be used to directly determine the propagation velocity for charge excitations on the nanotube. Such an experiment would help to resolve the open question of whether high frequency charge excitations in one-dimensional conductors such as a single-walled carbon nanotube are described by Fermi liquid theory or Luttinger liquid theory, as these two theories make non-trivially different predictions for the charge propagation velocity (Burke 2003). Using the results from this chapter as a scientific foundation, we hope to perform such an experiment in the near future.

Chapter 5

Conclusions and Future Work

We have performed a systematic study of the superconducting niobium microbolometer at microwave and terahertz (THz) frequencies. This device has been designed for applications in THz spectroscopy of room temperature samples. In particular, the fast response of the detector (~ ns) enables time-resolved spectroscopy measurements that complement the capabilities of existing experimental systems that achieve sub-ns time resolution with an optical delay line.

The measured detector response time agrees with previous determinations of the electron-phonon inelastic scattering time in thin-film niobium. We used Johnson noise to accurately determine the thermal conductance of the niobium electron system above T_c as a function of temperature. This enables a determination of the predicted noise at the superconducting transition due to statistical thermal fluctuations, which we find is consistent with the measured noise performance within the device response bandwidth,

with *1/f* noise becoming appreciable only below 100 Hz. We have also characterized the device response as a function of signal power and bath temperature.

To study the device response at THz frequencies, we designed and built a THz Fourier transform spectrometer using a broadband blackbody source. This enabled measurements of the input coupling, which is primarily determined by the geometry of the planar antenna structure. We fabricated and tested devices with two antenna types, the double-dipole and the log spiral. The measured spectral response is consistent with electromagnetic simulations. We also performed an initial demonstration of this device in a time-resolved terahertz spectroscopy application, in which we measured the free carrier lifetime in photoexcited silicon and gallium arsenide.

Such a detector could be employed for similar free carrier lifetime measurements in other materials, such as semiconductor nanoparticle films, which are candidate materials for next-generation photovoltaics (Turner 2002, Baxter 2006). Another interesting potential application is in studies of protein folding, as THz signals couple to molecular motion involving secondary and tertiary protein structure (Chung 2005). Such a detector would also be well suited for use in a THz version of the Balle-Flygare microwave cavity ring down spectrometer, which is a powerful tool for probing the modes of highly excited molecules (Balle 1981, Blake 2001).

These niobium detectors were designed to optimize the intrinsic tradeoff between detector speed, sensitivity, and power handling for performing time-resolved spectroscopy of room temperature samples. In related work, we have characterized a superconducting titanium bolometric detector that was designed to achieve extremely high sensitivity, but at the price of a slower response time and greatly reduced power

handling. This device has a much lower critical temperature of 0.3 K and a reduced active device volume. The goal of this work is to create the first energy-resolving THz single-photon detector. Coupling such an ultra-sensitive detector to a room temperature THz photon source, even one that is highly attenuated, poses significant technical challenges. In order to perform device characterization and optimization, we developed a new experimental technique. In this technique, the energy of a single THz photon is simulated by the absorbed energy of a short microwave pulse. We call this microwave pulse a faux photon, or fauxton. This technique allows the device to be operated in an extremely "dark" environment with input coupling that is well calibrated and input energy that is easily tunable.

In these experiments, we have demonstrated that the device response time is consistent with predictions based on electron-phonon coupling with strong negative electrothermal feedback. By studying the detection statistics, we are able to determine the energy resolution. We find that the experimental results are in good agreement with the predicted energy resolution based on the relevant sources of noise and the effect of electrothermal feedback.

In future work, we hope to demonstrate the detection of real single mid-infrared and THz photons with these devices. These experiments will be conducted in collaboration with colleagues at the Jet Propulsion Lab. The use of the fauxton characterization technique can set a benchmark for such optical measurements, and it also offers the capability for *in situ* measurement optimization using fauxtons prior to the detection of real photons. Comparison of these two tests will allow us to explore the issue of energy equilibration following the absorption of a real (~meV) photon.

A significant portion of the work described in this thesis involved the development of experimental techniques to use sensitive electrical measurements to determine the thermal state of a micro-device at cryogenic temperatures. Besides detector characterization, these techniques can also be applied to study the electrothermal properties of novel nanosystems. We have performed such a study of an individual single-walled carbon nanotube. Using Johnson noise, we established that the dc resistance is a direct probe of the nanotube electron temperature at finite bias current. This requires a nanotube with ohmic contacts, which is true for our sample at electron temperatures above approximately 20 K.

By performing measurements as a function of temperature, and by measuring nanotube sections of different lengths, we were able to develop a detailed model for the inelastic processes of the nanotube electron system. We find that, at high bias current and temperature (T_e > 120 K), the cooling of the nanotube electron systems increases rapidly with increasing temperature, with the thermal conductance scaling approximately as T_e^5. This behavior is consistent with the recently proposed mechanism of emission of surface polar phonons directly into the silicon dioxide substrate.

At intermediate temperatures and bias currents (approximately 50 K < T_e < 120 K), the thermal conductance scales linearly with the nanotube length and approximately quadratically with the electron temperature. By comparing our measured thermal conductance with previous determinations of the phonon thermal conductance, we conclude that the limiting process for removing energy is electron-acoustic phonon inelastic scattering. This also enables a determination of the electron-acoustic phonon inelastic scattering time, which is very fast, < 10 ps.

Below 50 K, the thermal conductance scales linearly with the nanotube length, but the temperature dependence becomes weaker than T_e^2, and is approximately linear in T_e. This is an unexpected result, as a thermal conductance that is linear in temperature implies a temperature-independent inelastic scattering time. The understanding of this result remains an open question, although we speculate that it may be due to the phonon interface thermal conductance.

With the experimentally determined thermal conductance, we can use the dc resistance $R = V/I$ to predict the differential resistance dV/dI with no adjustable parameters, and we find good agreement with experiment. Additionally, the measured rf heterodyne response agrees well with the calculated response using the thermal conductance data. These results are strong confirmations that our determination of the nanotube thermal conductance is correct.

The techniques used here to study the single-walled carbon nanotube could also be employed to study the electrothermal properties of other conducting nanosystems. One interesting possibility is to study the bolometric response of a carbon nanotube or a graphene sheet that exhibits proximity-induced superconductivity (Kasumov 1999, Heersche 2007). The resulting superconducting bolometric device would combine the strongly temperature-dependent resistance of a superconductor with the extremely small heat capacity of an atomically thin nanotube or graphene sheet, resulting in an exceptionally fast and sensitive bolometer. Such a device would be very interesting from both a fundamental physics perspective as well as for applications.

Appendix A:

Fabrication of Niobium Microbolometers

A.1 Fabrication process

In this section, we describe the fabrication of the optically-patterned antenna-coupled niobium (Nb) microbolometers discussed in chapter 2. The devices are fabricated on 200 μm thick, double side polished, high resistivity (> 20 kΩcm), float-zone, 2" silicon wafers (CrysTec GmbH Kristalltechnologie). The first generation of devices, with 38 μm double-dipole antennas, was patterned with electron-beam lithography. This fabrication was performed by Matthew Reese and Dr. Luigi Frunzio, and has been described in (Reese 2006, Reese 2007). Subsequent devices with different antenna geometries were patterned with optical lithography, which enables the simultaneous fabrication of > 100 devices. For this process, a photolithography mask was designed in AutoCAD, and the mask was produced by Photo Sciences, Inc. An image of the CAD file used to produce the mask, as well as a close-up showing four chips, are shown in figure A.1.

The device fabrication described here was performed with Anthony Annunziata and Dr. Luigi Frunzio using the facilities in the cleanroom of the Yale Center for

Microelectronic Materials and Structures. First the wafer is cleaned by sonicating in acetone and then methanol for 3 min. each, followed by washing in de-ionized (DI) water and blowing dry with nitrogen. We next spin on Shipley SC1827 photoresist at 4,000 rpm for 60 sec. The nominal resist thickness is 2.7 μm. The wafer is then baked at 115 ^{0}C for 120 s. The wafer is aligned to the mask and then exposed in the EVG 620 mask aligner. Exposure is for 13.8 seconds with a measured UV intensity of 4.65 mW/cm^2 at 365 nm and 13.48 mW/cm^2 at 405 nm. Following exposure, development is performed in Microposit MF-319 for 70 s.

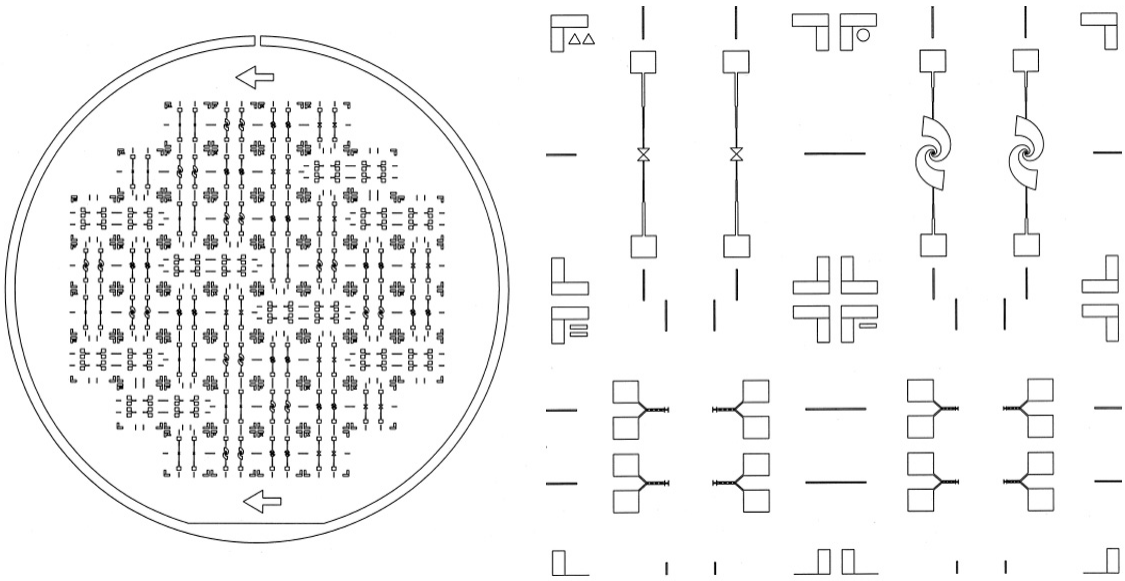

Figure A.1. Image from CAD file used to make the photolithography mask (left). On the actual mask, the enclosed areas are transparent, and non-enclosed areas are opaque. The arrows indicate the direction for the angled Al deposition, as the antenna geometries were designed to correct for the effect of shadowing by the resist. The wafer flat should be aligned with the flat on the bottom of the mask. On the right is a close-up showing four chips. Each 5 x 5 mm chip has either 2 or 4 devices, depending on the antenna geometry. The four chips seen here have bowtie, log spiral, and two sizes of double-dipole antennas. Marks for dicing each chip as well as aligning the device with a lens are visible.

The developed wafer is placed in the Kurt J. Lesker ultra-high vacuum sputter deposition system, which has a base pressure of 5×10^{-9} Torr. In the 2" wafer holder, the wafer is placed face-down with the flat of the wafer facing the back prong (the prong that faces away from you when you load the wafer holder into the load-lock), and then the wafer is rotated 78^0 clockwise relative to the wafer holder. After loading the sample into the main chamber and pumping down the main chamber for several hours, we pre-sputter the Nb target at 350 W with an argon pressure of 1.3 mTorr for 2 min. Next the wafer is cleaned with a neutralized argon ion beam with a current density of 240 $\mu A/cm^2$ for 15 s. This is followed by dc magnetron sputtering of Nb for 9 s (again at 350 W with an argon pressure of 1.3 mTorr) with the wafer directly above the Nb target. The deposition rate is approximately 1.25 nm/s. This is followed by thermal evaporation of 200 nm of aluminum (Al) at a rate of approximately 1 nm/s and at an angle of 40^0 from the substrate normal. To achieve this angle, the J-arm is positioned at 15.6^0 for depositing from Al source 4. Because of the angle, we deposit until the crystal monitor reads 250 nm, which should yield approximately 200 nm of Al on the wafer. The technique for determining the J-arm angle is detailed in (Reese 2006). This angled deposition covers the antenna and lead structure but does not cover the narrow microbridge, and produces the shadowing effect that is seen in figure A.2. The Al source is in a recessed well, and the side of this well blocks the Al from part of the wafer. This results in the two right-most columns of the wafer having no Al deposited. Even without these two columns, each 2" wafer can yield over 100 functional devices.

Liftoff is done in hot acetone at $65\ ^0C$ for several hours, followed by ~1 min. of sonication in the same acetone. A protective layer of resist is spun on the wafer, and it is

diced using a MicroAutomation 1006 dicing saw into 52 5 x 5 mm chips. In figure A.3 we show an atomic force microscope image of a completed device. Flagging is seen on the sides of the bridge, which results from the use of a liftoff process with a resist monolayer. A monolayer (i.e. no undercut) is essential to avoid spreading of the sputtered Nb. If a more uniform bridge profile is desired, one could switch to an etching process.

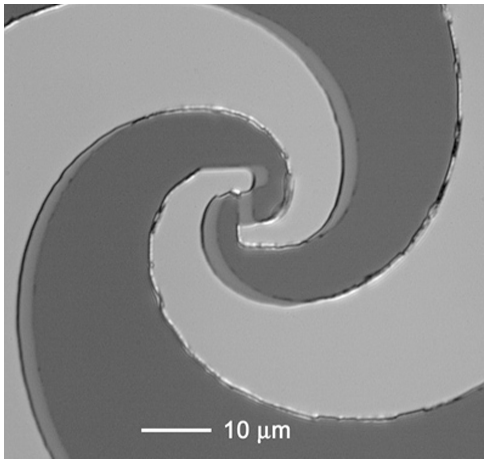

Figure A.2. Optical image of device with log spiral antenna showing the shadowing effect from the angled Al deposition. Lighter gray is Al and darker gray is Nb.

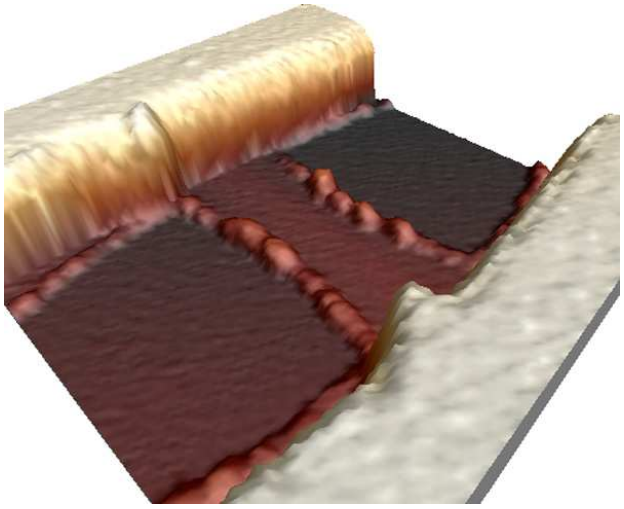

Figure A.3. Atomic force microscope image showing Nb microbridge and Al contacts. Flagging can be seen as the row of raised bumps on either side of the Nb microbridge. Image courtesy of J. Chudow.

A.2 Niobium characterizations

Devices without Al and with different thicknesses of Nb were fabricated to determine the microbridge geometry that would provide the desired normal state resistance and T_c. These samples were deposited using similar sputtering conditions to those described in the previous section, and these depositions were performed by Matthew Reese and Dr. Luigi Frunzio. The thickness was measured with a Quesant Q-Scope 250 scanning probe microscope. Each microbridge was measured in several places and the different thickness values were averaged. The estimated uncertainty in the resulting thickness determination is ± 2 nm. In figure A.4 we plot the measured T_c and sheet resistance above T_c as a function of the thickness.

The thickness-dependence of T_c in 2D disordered wires has been treated theoretically by Oreg and Finkel'stein (1999). They find that T_c is suppressed as the thickness is decreased (disorder is increased) because of an increase in the effectiveness of Coulomb interactions. They derive an expression for the dependence of T_c on the sheet resistance R_{sq},

$$\ln\left(\frac{T_c}{T_{c0}}\right) = \frac{1}{\gamma} - \frac{1}{\sqrt{2t}} \ln \frac{\gamma + \sqrt{t/2}}{\gamma - \sqrt{t/2}} \qquad \text{(A.1)}$$

where T_{c0} is the bulk critical temperature, 9.3 K for Nb; $t = (e^2/\pi\hbar)R_{sq}$; and γ is a fitting parameter related to the scattering time. We fit an empirical function to the measured R_{sq} as a function of thickness, and then use this relationship to fit equation (A.1) to the measured T_c as a function of thickness with γ as an adjustable parameter. We see that the data are well described by equation (A.1) with $\gamma = 0.055$.

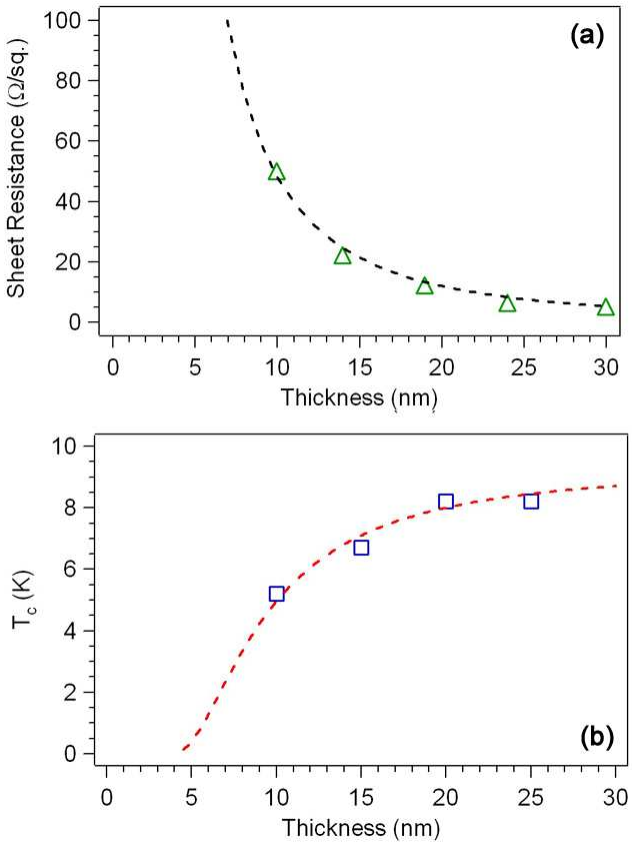

Figure A.4. (a) Sheet resistance R_{sq} measured above T_c as a function of thickness for Nb microbridges. Dashed line is an empirical fit, $R_{sq} = 4801/d^2$, where d is the thickness in nm. (b) Measured T_c as a function of film thickness. Dashed line is a fit to equation (A.1).

We found that the residual resistance ratio, or RRR, was a useful means of characterizing our devices and was a good predictor of thickness and hence T_c. The RRR is defined here as the ratio of the resistances at room temperature and just above T_c. In figure A.5 we plot the measured RRR as a function of film thickness, along with a linear fit.

We have also measured the perpendicular critical field H_{c2} for a 12 nm thick Nb microbridge device (with Al contacts). The resistance as a function of applied field is shown in figure A.6. This was measured at a bath temperature of 0.24 mK, using the

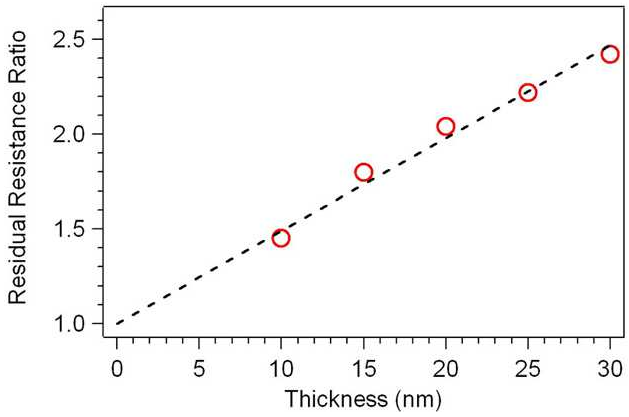

Figure A.5. Residual resistance ratio as a function of film thickness. Dashed line is a linear fit with a slope of 0.05.

cryogenic system described in chapter 3 with a 5 T superconducting solenoid magnet. The critical field can be used to determine the superconducting coherence length $\xi(T)$ from (Tinkham 1996)

$$H_{c2} = \frac{\Phi_0}{2\pi\xi^2(T)}, \tag{A.2}$$

where Φ_0 is the fluxoid quantum $hc/2e$. At a bath temperature of 0.24 K, we are in the regime where $T << T_c$ and hence $\xi(T) \approx \xi(0)$. Defining the midpoint of the resistive transition as approximately 2.7 T, we find $\xi(0) \approx 11$ nm.

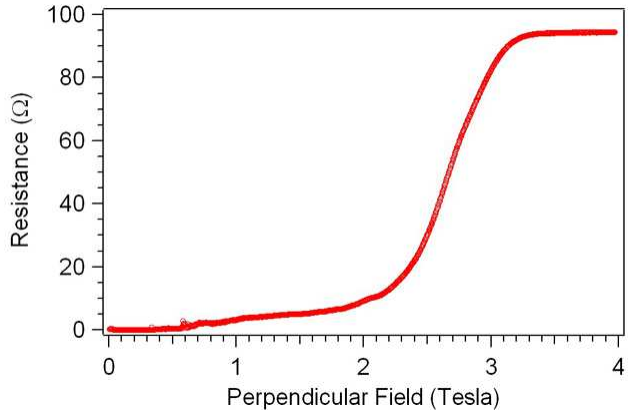

Figure A.6. Measured resistance as a function of applied perpendicular magnetic field at a bath temperature of 0.24 K. Resistance is measured with a 1 μA bias current.

The coherence length is relevant to our devices because thick non-superconducting contacts in good contact with the Nb film will drive normal the Nb in the microbridge a distance ~3$\xi(T)$ at each end due to the proximity effect (Siddiqi 2002). $\xi(T)$ scales as $1/(1-T/T_c)$ near T_c (Tinkham 1996). Immediately adjacent to the contacts, we assume the microbridge temperature is close to the bath temperature T_{bath}. For operation at $T_{bath}/T_c = 0.9$, we estimate $\xi(0.9) \approx 100$ nm. Although not negligible, this is still a relatively small length compared to the total microbridge length, which is either 5 μm or 2.5 μm.

This effect only occurs if the contacts are non-superconducting. For $T_{bath} < T_c$, where T_c refers to the microbridge critical temperature, the Nb underneath the Al in the contact region may be superconducting or may be driven into the non-superconducting state via the proximity effect. The state of the Nb in the contacts can be determined from a dc current-voltage (I-V) curve. The Nb in the contacts is much wider than the microbridge, and hence will have a much smaller current density for the same dc current. Below T_c, when the microbridge is driven into the normal state by an applied current, the slope of the I-V curve is then equal to the inverse of the resistance. If the Nb in the contacts is superconducting, this creates a normal metal-superconductor (NS) junction where the microbridge meets the contact, which has an additional, or excess, current due to Andreev reflection at the junction (Andreev 1964, Tinkham 1996). If the contacts are superconducting, a linear fit to the non-superconducting branch of the I-V curve will have a non-zero intercept on the current axis due to this excess current, as seen in figure A.7.

The superconducting energy gap Δ, and hence the T_c, of the Nb in the contacts can be determined from the value of this excess current following Klapwijk, Blonder and

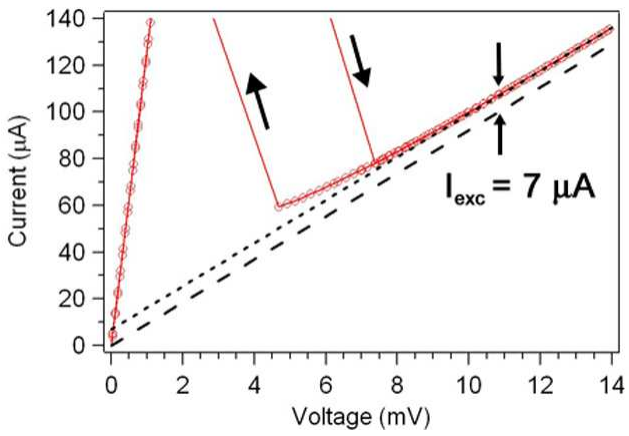

Figure A.7. Close-up of I-V curve of Nb microbolometer device measured at T_{bath} = 4.2 K showing an excess current I_{exc} = 7.0 μA. This indicates that the Nb in the contact region is superconducting.

Tinkham (1982), who relate the excess current to Δ for an NS junction with perfect interface transparency,

$$I_{exc} = \frac{1}{eR_n}\int_0^{\infty}\left[f_0(E-eV) - f_0(E)\right]A(E)\,dE \qquad \text{(A.3)}$$

where R_n is the resistance above T_c, f_0 is the Fermi distribution of the normal metal, E is the bias energy relative to the pair potential, and $A(E)$ is given by

$$A(E) = \begin{cases} 1 & |E| < \Delta \\ \left[|E| - \left(E^2-\Delta^2\right)^{1/2}\right] \Big/ \left[|E| + \left(E^2-\Delta^2\right)^{1/2}\right] & |E| > \Delta \end{cases}. \qquad \text{(A.4)}$$

The T_c determined from the data in figure A.7 is 5.1 K, which is close to the lower end of the microbridge transition. In this way, a dc I-V curves provide a simple diagnostic of the state of the contact pads. This is especially useful because it can be difficult in a two-wire resistance measurement to determine if the resistance below T_c has a contribution from the Al-Nb bilayer.

Appendix B:

Fabrication of THz Alignment Chips

Proper alignment of an antenna-coupled device at the focal point of a silicon (Si) lens is essential for achieving efficient THz coupling, as discussed in section 2.4. To facilitate this alignment, we have fabricated double-side patterned Si alignment chips. These chips are patterned on both sides with markings that are aligned to each other. A 6 mm diameter hyperhemispherical lens is aligned and affixed on one side, and the device substrate is aligned and affixed on the opposite side. We describe here the fabrication of these chips. This fabrication was performed with Dr. Luigi Frunzio.

The pattern pictured in figure B.1 was designed to fabricate twelve alignment pieces, 12 mm x 12 mm each, on a 2” diameter, high-resistivity, double-side-polished Si wafer. The pattern was designed in AutoCAD and printed on a transparency film at a resolution of 20,000 dpi by CAD/Art Services. The nominal local accuracy of the printed pattern is 2 μm and the nominal global accuracy is 12.5 μm. The cost of a transparency is ~10% the cost of a photolithography mask. Each half of the pattern was cut out of the transparency film and taped onto a 3 mm thick clear glass plate.

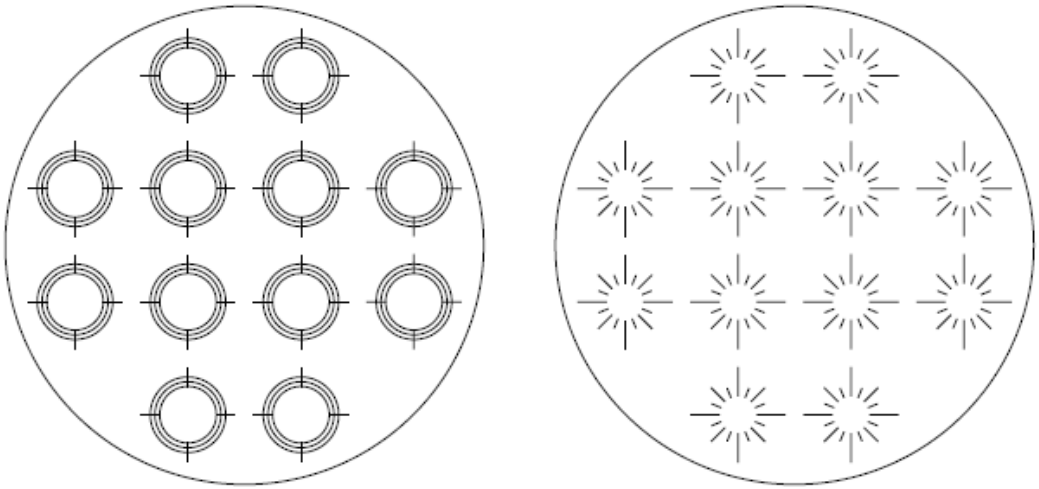

Figure B.1. Image of transparency mask used to fabricate double-sided alignment pieces.

The wafer was cleaned and then spun with AZ5214E photoresist at 4,000 rpm for 60 sec, followed by baking at 90 ^{0}C for 60 sec. Next the transparency mask and wafer were loaded into the EVG 620 mask aligner. The exposure used the recipe "LF8Z5214E_backalignment" in hard contact mode with a 2 sec UV exposure. The measured UV power output was 14.55 mW/cm^2 at 365 nm and 37.2 mW/cm^2 at 405 nm; the exposure time should be adjusted linearly for different power levels. Following exposure, the wafer was baked at 115 ^{0}C for 3 min, followed by a 60 second UV flood exposure in the Suss mask aligner. We used a small piece of tape to ensure that the wafer did not move on the stage of the Suss during the exposure (the chuck applies air pressure that causes an unsecured wafer to move). The wafer was then developed for 37 s in a 1:1 mixture of Microposit developer and DI water. We deposited 100 nm of Al in the Plassys MEB550S electron-beam evaporation system. Finally, we lifted-off in hot acetone (65 ^{0}C) for several hours followed by several minutes of sonication in the same acetone.

The same process is repeated for patterning the reverse side, using the other half of the transparency mask, with the following modifications. We used the recipe "LF8Z5214E_backalignment_bottom," being sure to select "bottom exposure" and "crosshair" from the list of options on the recipe. The mask was loaded using the 4" chuck (with two holes for viewing the back of the wafer) and the 5" mask frame. In "bottom exposure" mode, the imaging is all done from the bottom side microscope. After adjusting the mask but before loading the wafer, a crosshair appears on each side of the screen. Align each crosshair with the outermost point of an alignment pattern on the mask. Then load the wafer (on the 4" chuck; do not worry that the wafer is smaller than what the chuck is designed for), at which point you will adjust the wafer until the crosshairs line up with the outermost points of the appropriate alignment patterns on the back of the wafer. Now the mask on the front of the wafer is aligned with the pattern on the back of the wafer, and you can proceed with exposure, development, and deposition as before. When the fabrication is completed, the wafer can be diced into twelve individual pieces.

Appendix C:

Dissipative Cryogenic Low-Pass Filters

C.1 Introduction

The magnetically lossy transmission line as a low-pass filter has been known for many years (Schiffres 1964, Denny 1968). This type of filter is often used to achieve very broad high frequency attenuation combined with negligible dc resistance, e.g. for filtering the leads of power supplies. We have developed a magnetically lossy transmission line filter that is designed to have a passband that extends up to ~GHz combined with an extremely broad stopband over which incident signals are absorbed rather than reflected.

Our interest in developing this type of filter came from our work on microwave heterodyne mixing in superconducting microbolometers. The experimental apparatus used for these measurements can be seen in figure 2.3. The input impedance of the first stage amplifier is, in general, not 50 Ω at the LO and RF frequencies, which are often outside the amplifier's bandwidth. This impedance mismatch results in standing wave interference at the LO and RF frequencies. Because this interference depends on the device impedance, it is difficult to capture in a calibration. As an illustration, we show in

figure C.1 the measured attenuation from the coupled port to the input port of a -20 dB directional coupler with the transmitted port both properly and improperly terminated. Ensuring a proper termination at the transmitted port proved to be important for accurate bandwidth measurements, such as the data in figure 2.6. While a matched impedance could also be achieved by using an attenuator at the amplifier input, this decreases the signal-to-noise at the intermediate frequency output. The dissipative low-pass filters described in this appendix enable us to ensure a matched impedance at the transmitted port without compromising signal-to-noise. These filters have previously been described in Santavicca and Prober (2008).

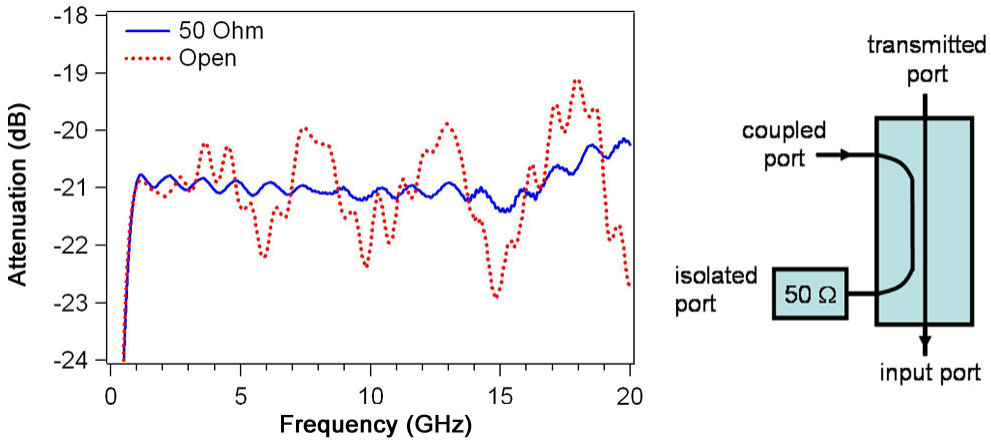

Figure C.1. Left: Measured attenuation from the coupled port to the input port of a 1-18 GHz -20 dB Mac Technology directional coupler with a 50 Ω and an open termination on the transmitted port. Right: Schematic of a directional coupler.

This type of filter is generally useful for microwave frequency measurements of non-linear quantum devices. Such devices are extremely sensitive to high frequency noise and hence require careful cryogenic filtering (Vion 1995). The termination impedance seen by the device can also have a significant effect on its performance. Termination by

an incorrect impedance may have a detrimental effect that is difficult to model or predict. An ideal filter will not only attenuate strongly out to very high frequency, it will also maintain a matched input impedance.

When measuring highly sensitive cryogenic devices, it is often important to attenuate room temperature thermal (blackbody) noise. For coupling via a 1D transmission line such as a coaxial cable, the noise power P per unit bandwidth B is given by the 1D Planck spectrum,

$$\frac{P}{B} = \frac{hf}{e^{hf/k_B T} - 1}. \qquad \text{(C.1)}$$

At T = 300 K, this extends in frequency up to ~10 THz. Cable losses effectively attenuate the highest frequencies, but a filter with a stopband extending to >100 GHz is desirable. It is difficult to achieve effective filtering at frequencies >> 10 GHz with lumped element components due to their parasitic reactance. To filter up to ~100 GHz, an alternative approach is required.

A much broader stopband can be achieved by using spatially distributed circuit elements instead of lumped-element components. Several types of non-impedance-matched distributed filters have been reported, primarily for filtering the biasing lines of single-electron and quantum computing circuits. The most widely used is the metal powder filter, which consists of a long wire embedded in a mixture of metal powder and epoxy (Martinis 1987, Fukushima 1997, Bladh 2003, Lukashenko 2008). This low-pass filter utilizes the capacitance between the wire and the powder as well as eddy-current dissipation in the powder and has a typical 3 dB bandwidth ~MHz. (The 3 dB bandwidth is the frequency at which the attenuation is 3 dB, or approximately ½ in linear units.)

Microfabricated versions of such non-impedance-matched distributed filters have also been reported (Vion 1995, le Sueur 2006).

To achieve impedance matching, a distributed filter must be constructed in a transmission line geometry with frequency-dependent dissipation in the conductor or the dielectric. Previous work described a filter based on the resistive coaxial cable Thermocoax (Zorin 1995) and a metal powder filter in a coaxial geometry (Milliken 2007). We describe a filter that uses a magnetically-loaded dielectric in a stripline geometry. This filter exploits a combination of magnetic and dielectric dissipation to achieve significantly greater attenuation per unit length in the stopband than previous impedance-matched filters. The stripline filter also demonstrates a return loss greater than 10 dB (less than 10% reflected power) out to 40 GHz. The performance of these three types of impedance-matched low-pass filters is compared in table C.1.

Filter	DC resistance per unit length (Ω/m)	Attenuation per unit length at 10 GHz (dB/m)	Return loss at 10 GHz (dB)
Thermocoax cable (Zorin 1995)	~50	~175	~6
Coaxial metal powder filter (Milliken 2007)	< 1	~590	>10
Stripline filter (this work)	< 1	>3000	>10

Table C.1. Comparison of lossy transmission line filters.

C.2 Filter Design

A stripline geometry was chosen because it is easier to construct than a coaxial geometry and, unlike a microstrip, the field lines are entirely inside the dielectric, maximizing the

dissipation. The stripline supports a TEM mode at low frequency, with higher order modes appearing when the enclosure begins to act as a waveguide.

To determine the attenuation constant, we consider a TEM mode in a transmission line with a complex permittivity and permeability. The permittivity can be expressed as $\varepsilon = \varepsilon' - j\varepsilon'' = |\varepsilon| e^{j\delta_\varepsilon}$, where $\tan\delta_\varepsilon = \varepsilon''/\varepsilon'$ is the dielectric loss tangent. Similarly, the permeability can be expressed as $\mu = \mu' - j\mu'' = |\mu| e^{j\delta_\mu}$, where $\tan\delta_\mu = \mu''/\mu'$ is the magnetic loss tangent. The complex propagation constant is $\gamma = j\omega\sqrt{\varepsilon\mu} = \alpha + j\beta$, where ω is the angular frequency, α is the attenuation constant, and β is the phase constant. For propagation in the x direction, the electric field magnitude is $E(x) = E(0)e^{-\gamma x}$. We can express the attenuation constant $\alpha = \mathrm{Re}[\gamma]$, which can be written using the above relations as

$$\alpha = (1.48\times10^{-8}) f \sqrt{\frac{\mu'\varepsilon'}{\mu_0\varepsilon_0}} \left\{ \sqrt{\left[1+\left(\frac{\varepsilon''}{\varepsilon'}\right)^2\right]\left[1+\left(\frac{\mu''}{\mu'}\right)^2\right]} - 1 + \left(\frac{\varepsilon''}{\varepsilon'}\right)\left(\frac{\mu''}{\mu'}\right) \right\}^{1/2} \qquad \text{(C.2)}$$

in units of Np/m, where f is the frequency and μ_0 and ε_0 are the free space permeability and permittivity, respectively. The transmitted power is thus $P(x) = P(0)e^{-2\alpha x}$. The attenuation due to the dielectric material depends on the length but is otherwise independent of the transmission line geometry and is only a function of the dielectric material properties. Magnetically-loaded dielectrics provide very high attenuation because they typically have a magnetic loss tangent that increases with frequency up to ~GHz combined with a large permittivity (Park 2000).

The magnetically-loaded dielectrics used in our filters are from the Eccosorb line of microwave absorbing materials from Emerson & Cuming Microwave Products. They

come in carbon- and magnetically-loaded varieties in different thicknesses and with several dielectric embedding materials. We used the FGM-40, GDS, and MCS materials, which are magnetically-loaded silicone sheets, as well as the CR-124 material, which is a magnetically-loaded epoxy. The magnetic loading material is carbonyl iron or ferrite powder, or a combination of the two.

A rectangular enclosure, machined in a block of copper, defines the outer dimensions of the stripline. The enclosure is filled with the Eccosorb material. Two SMA receptacles with an extended dielectric and pin contact (Applied Engineering Products part #9308-1113-001) are mounted on each end of the copper block such that the pins extend into the center of the enclosure. Connecting the pins is a strip cut from a sheet of 0.15 mm thick Cu foil. The ends of the strip are soldered to each pin contact. The silicone material has the advantage of allowing the strip to be modified after construction of the filter, as the strip is simply sandwiched between two layers of material. An image of two completed filters made with the silicone Eccosorb material is presented in figure C.2.

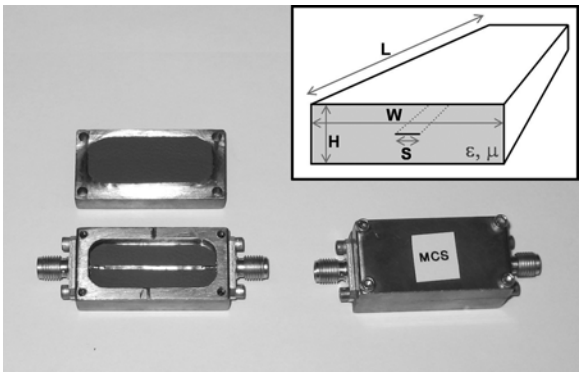

Figure C.2. Photograph of two completed filters, one open and one closed. Inset: sketch of the stripline geometry, shown in a cross-sectional cut viewed from the end.

The dimensions of each stripline filter, as illustrated in figure C.2, are summarized in table C.2. The center conductor width S was chosen by testing strips of different widths and selecting the one that gave the greatest average return loss in the measurement range 50 MHz – 40 GHz after a calibration at the coaxial connector reference plane. Introducing a slight taper on each end of the center conductor further improved the reflection coefficient. We used a linear taper for simplicity and found that the greatest return loss was obtained with a taper that transitions from the width of the pin to the width of the center conductor in a length of 2-3 mm. The stripline geometry assumes that the side walls do not significantly alter the field lines. This condition is valid if the width of the stripline enclosure W is much greater than the width of the center conductor S. In our design, the enclosure width is always more than ten times the width of the center conductor.

Dielectric Material	S (mm)	H (mm)	W (mm)	L (mm)
CR-124	1.4	4.6	18	32
FGM-40	1.1	2.0	13	32
GDS	0.8	1.5	13	32
MCS	1.1	2.0	13	32

Table C.2. Filter dimensions.

C.3 Filter characterization

The attenuation and return loss of the stripline filters made from the four different Eccosorb materials were measured at room temperature, 77 K, and 4.2 K using an HP 8722D 50 MHz – 40 GHz network analyzer. The attenuation is defined as *-10 log*

(P_{trans}/P_{inc}), where P_{trans} is the power measured at the output of the filter and P_{inc} is the power incident on the input of the filter. The return loss is defined as *-10 log (P_{ref}/P_{inc}),* where P_{ref} is the power that is reflected off the filter input. For testing at 77 K and 4.2 K, the filter was immersed in liquid nitrogen and liquid helium, respectively. The filter performance was unchanged after multiple thermal cycles. The attenuation of each filter is presented in figure C.3. The 3 dB bandwidth (f_{3dB}) increases as the temperature is lowered for all four filters. This is likely due to a decrease in the permittivity with decreasing temperature.

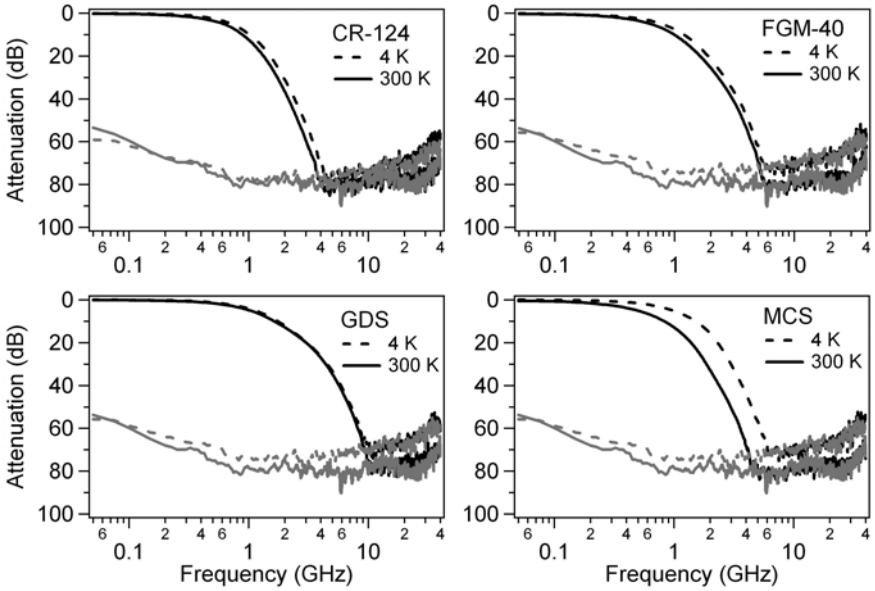

Figure C.3. Measured attenuation of the CR-124, FGM-40, GDS, and MCS stripline filters at room temperature (solid line) and 4.2 K (dashed line). The instrument noise floor is indicated in grey. (The noise floor is higher at 4.2 K because of the loss of the extra cables used to measure at low temperature.)

The signal can no longer be seen above the instrument noise floor above 4-10 GHz. Separate measurements were carried out using an Agilent E8254A signal generator and an HP8593E spectrum analyzer. Using a 1 kHz resolution bandwidth, the noise floor of the spectrum analyzer at 10 GHz was approximately -100 dBm. Using a source power

of 0 dBm, we could determine the frequency above which the filter displays greater than 100 dB of attenuation (f_{100dB}). These results, along with f_{3dB}, are summarized in table C.3.

Dielectric Material	f_{3dB} (GHz), 4.2 K	f_{3dB} (GHz), 77 K	f_{3dB} (GHz), 295 K	f_{100dB} (GHz), 295 K
CR-124	0.56	0.54	0.46	4.9
FGM-40	0.58	0.54	0.45	7.2
GDS	0.83	0.79	0.75	12.1
MCS	0.72	0.41	0.34	5.9

Table C.3. Summary of filter bandwidths at different temperatures.

Modifying the length of the stripline will modify the attenuation, enabling the bandwidth to be optimized for a particular application. In Figure C.4, we use the measured attenuation for a length of 32 mm to extrapolate the 3 dB bandwidth as a function of stripline length at both room temperature and 4.2 K. Given the inherent tradeoff between bandwidth and stopband attenuation, we note that filters with bandwidths >> 1 GHz may no longer have sufficient high frequency attenuation for some applications.

The return loss is approximately the same for all four filters and is highly sensitive to the coaxial-to-stripline transition. The return loss of the GDS stripline filter is plotted in figure C.5. At room temperature, the return loss is greater than 15 dB at all frequencies. The return loss is slightly lower at low temperature, which is likely related to a temperature-dependent permittivity, but remains greater than 10 dB at all temperatures measured. (The width of the center conductor was chosen based on room temperature measurements.) An improved coaxial-to-stripline transition or a filter made in a coaxial geometry could likely achieve a somewhat greater return loss. However, the average

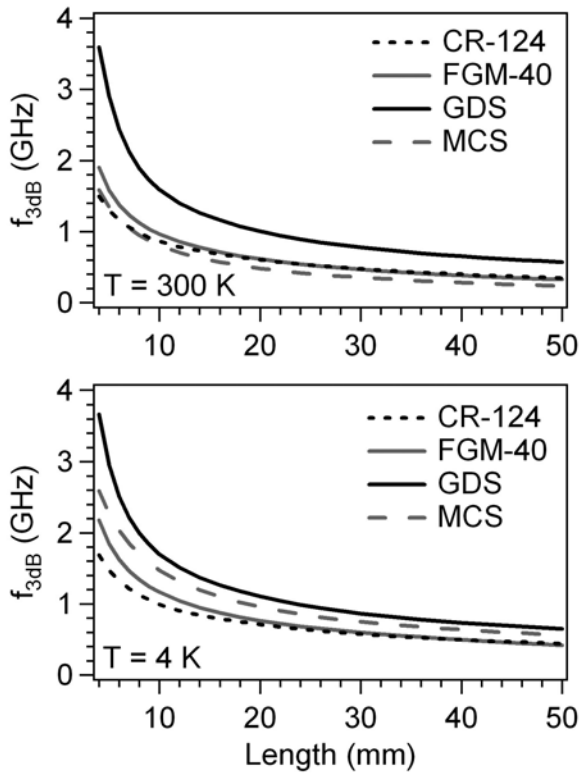

Figure C.4. Extrapolated 3 dB bandwidth for filters of different stripline lengths at both room temperature (top) and 4.2 K (bottom).

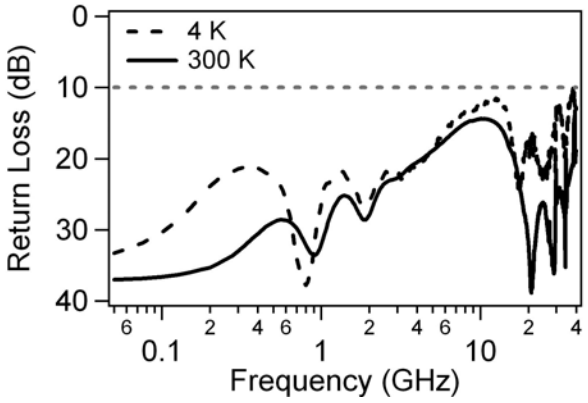

Figure C.5. Return loss of the GDS stripline filter at room temperature and 4.2 K. For reference, a return loss of 10 dB (10% reflected power) is indicated by the grey dashed line.

return loss over this frequency range is limited by the fact that the magnetic permeability, and hence the impedance, changes with frequency.

A sufficiently large external field will saturate the internal magnetization, decreasing the permeability and hence the attenuation. At room temperature, f_{3dB} of the MCS stripline filter increased from 0.34 to 0.65 GHz with an external field of approximately 0.1 T applied perpendicular to both the direction of signal propagation and the flat side of the center conductor. The field was applied with a permanent magnet, and the field strength was measured with a gaussmeter. The filter bandwidth returned to its original zero-field value upon removal of the external field.

An important issue for these filters is thermalization. As the filter is strongly absorbing in its stopband, it will also be an efficient emitter of thermal noise, with a noise power given by equation (C.1). In the Rayleigh-Jeans limit, this simplifies to the Johnson noise result, with a noise power per unit bandwidth of $k_B T$, where T is the physical temperature of the filter dielectric material. For measurements of ultra-sensitive devices, having the filter at low temperature is important for minimizing the noise power seen by the device. Recent work by Slichter *et al*. (2009) measured similar filters made from silicone-based Eccosorb material down to 50 mK and found that the silicone material did efficiently thermalize with its environment.

C.4 Conclusion

We have constructed and characterized magnetically lossy low-pass stripline filters for cryogenic measurements of sensitive devices. These filters simultaneously achieve a broad, high-attenuation stopband and high return loss measured out to 40 GHz. The 3 dB

bandwidth is between 0.3 and 0.8 GHz and can be adjusted beyond this range by changing the filter length. We also note that a significantly sharper roll-off can be achieved with only a modest change in the return loss by following the stripline filter with a conventional reactive filter of an appropriate bandwidth.

Bibliography

Abrahams, E., P.W. Anderson, P.A. Lee and T.V. Ramakrishnan, "Quasiparticle lifetime in disordered two-dimensional metals," *Phys. Rev. B* **24**, 6783 (1981).

Andreev, A.F., "The thermal conductivity of the intermediate state in superconductors," *Sov. Phys. JETP* **19**, 1228 (1964).

Andrews, D.H., W.F. Brucksch, W.T. Ziegler, E.R. Blanchard, "Attenuated superconductors I. For measuring infra‑red radiation," *Rev. Sci. Instrum.* **13**, 281 (1942).

Astafiev, O., S. Komiyama, T. Kutsuwa, V. Antonov, Y. Kawaguchi and K. Hirakawa, "Single-photon detector in the microwave range," *Appl. Phys. Lett.* **80**, 4250 (2002).

Balanis, C.A., *Antenna Theory: Analysis and Design, 3rd Edition*, Hoboken, New Jersey: John Wiley & Sons, Inc. (2005).

Balle, T.J., and W.H. Flygare, "Fabry-Perot cavity pulsed Fourier transform microwave spectrometer with a pulsed nozzle particle source," *Rev. Sci. Instrum.* **52**, 33 (1981).

Baxter, J.B., and C.A. Schmuttenmaer, "Conductivity of ZnO nanowires, nanoparticles, and thin films using time-resolved terahertz spectroscopy," *J. Phys. Chem. B* **110**, 25229 (2006).

Beard, M.C., G.M. Turner, and C.A. Schmuttenmaer, "Transient photoconductivity in GaAs as measured by time-resolved terahertz spectroscopy," *Phys. Rev. B* **62**, 15764 (2000).

Beard, M.C., G.M. Turner, and C.A. Schmuttenmaer, "Terahertz spectroscopy," *J. Phys. Chem. B* **106**, 7146 (2002).

Benedict, L.X., S.G. Louie and M.L. Cohen, "Heat capacity of carbon nanotubes," *Solid State Commun.* **100**, 177 (1996).

Benford, D.J., M.C. Gaidis, and J.W. Kooi, "Optical properties of Zitex in the infrared to submillimeter," *Appl. Optics* **42**, 5118 (2003).

Benford, D.J., T.A. Ames, J.A. Chervenak, E.N. Grossman, K.D. Irwin, S.A. Khan, B. Maffei, S.H. Moseley, F. Pajot, T.G. Phillips, J.-C. Renault, C.D. Reintsema, C. Rioux, R.A. Shafer, J.G. Staguhn, C. Vastel and G.M. Voellmer, "First astronomical use of multiplexed transition edge bolometers," *AIP Conf. Proc.* **605**, 598 (2002).

Bergeal, N., R. Vijay, V.E. Manucharyan, I. Siddiqi, R.J. Schoelkopf, S.M. Girvin, and M.H. Devoret, "Analog information processing at the quantum limit with a Josephson ring modulator," arXiv:0805.3452 (2008).

Bethune, D.S., C.H. Klang, M.S. de Vries, G. Gorman, R. Savoy, J. Vazquez, and R. Beyers, "Cobalt-catalyzed growth of carbon nanotubes with single-atomic-layer walls," *Nature* **363**, 605 (1993).

Bladh, K., D. Gunnarsson, E. Hurfeld, S. Devi, C. Kristoffersson, B. Smalander, S. Pehrson, T. Claeson, P. Delsing, and M. Taslakov, "Comparison of cryogenic filters for use in single electron experiments," *Rev. Sci. Instrum.* **74,** 1323 (2003).

Blake, G.A., "Microwave and terahertz spectroscopy," *Encyclopedia of Chemical Physics and Physical Chemistry*, eds. J.H. Moore and N.D. Spencer, Philadelphia: Institute of Physics Publishing (2001).

Burke, P.J., R.J. Schoelkopf, D.E. Prober, A. Skalare, W.R. McGrath, B. Bumble, and H.G. LeDuc, "Length scaling of bandwidth and noise in hot-electron superconducting mixers," *Appl. Phys. Lett.* **68**, 3344 (1996).

Burke, P.J., "High frequency electron dynamics in thin film superconductors and applications to fast, sensitive THz detectors," Ph.D. dissertation, Yale University (1997).

Burke, P.J., "An RF circuit model for carbon nanotubes," *IEEE Trans. Nanotech.* **2**, 55 (2003).

Castellanos-Beltran, M.A., K.D. Irwin, G.C. Hilton, L.R. Vale and K.W. Lehnert, "Amplification and squeezing of quantum noise with a tunable Josephson metamaterial," *Nature Physics* **4,** 929 (2008).

Charlier, J.-C., X. Blase, and S. Roche, "Electronic and transport properties of nanotubes," *Rev. Mod. Phys.* **79**, 677 (2007).

Chervenak, J.A., K.D. Irwin, E.N. Grossman, J.M. Martinis, C.D. Reintsema, and M.E. Huber, "Superconducting multiplexer for arrays of transition edge sensors," *Appl. Phys. Lett.* **74**, 4043 (1999).

Chung, H.S., M. Khalil, A.W. Smith, Z. Ganim, and A. Tokmakoff, "Conformational changes during the nanosecond-to-millisecond unfolding of ubiquitin," *Proc. Nat. Acad. Sci. USA* **102**, 612 (2005).

Clarke, J., P.L. Richards, and N.-H. Yeh, "Composite superconducting transition edge bolometer," *Appl. Phys. Lett.* **30**, 664 (1977).

Dayen, J.-F., T.L. Wade, M. Konczykowski, J.-E. Wegrowe, and X. Hoffer, "Conductance in multiwall carbon nanotubes and semiconductor nanowires," *Phys. Rev. B* **72**, 073402 (2005).

Denny, H.W., and W.B. Warren, "Lossy transmission line filters," *IEEE Trans. Electromag. Compat*. **10,** 363 (1968).

Deshpande, V.V., S. Hsieh, A.W. Bushmaker, M. Bockrath and S.B. Cronin, "Spatially resolved temperature measurements of electrically heated carbon nanotubes," *Phys. Rev. Lett.* **102**, 105501 (2009).

Diez, M.C., T.O. Klaassen, C. Smorenburg, V. Kirschner, and K.J. Wildeman, "Reflectance measurements on sub-millimetre absorbing coatings for HIFI," *Proc. SPIE* **4013**, 129 (2000).

Dresselhaus, M.S., G. Dresselhaus, and P. Avouris, eds., *Carbon Nanotubes: Synthesis, Structure, Properties and Applications*, New York: Springer-Verlag (2001).

Dyson, J.D., "The equiangular spiral antenna," *IRE Trans. Antennas Propagat*. **13**, 181 (1959).

Evans, G., D.C. Schmadel, A.B. Sushkov, and H.D. Drew, "Silicon beamsplitter for Fourier transform spectroscopy at far infrared frequencies," arXiv:0706.4302 (2007).

Filipovic, D.F., S.S. Gearhart, and G.M. Rebeiz, "Double-slot antennas on extended hemispherical and elliptical silicon dielectric lenses," *IEEE Trans. Microwave Theory Tech.* **41**, 1738 (1993).

Floet, D.W., E. Miedema, T.M. Klapwijk, and J.R. Gao, "Hotspot mixing: A framework for heterodyne mixing in superconducting hot-electron bolometers," *Appl. Phys. Lett.* **74**, 433 (1999).

Fu, K., R. Zannoni, C. Chan, S.H. Adams, J. Nicholson, E. Polizzi, and K.S. Yngvesson, "Terahertz detection in single wall carbon nanotubes," *Appl. Phys. Lett.* **92**, 033105 (2008).

Fuhrer, M.S., B.M. Kim, T. Durkop, and T. Brintlinger, "High-mobility nanotube transistor memory," *Nano Lett.* **2**, 755 (2002).

Fukushima, A., A. Sato, A. Iwasa, Y. Nakamura, T. Komatsuzaki, and Y. Sakamoto, "Attenuation of microwave filters for single-electron tunneling experiments," *IEEE Trans. Instrum. Meas*. **46**, 289 (1997).

Galeazzi, M., and D. McCammon, "Microcalorimeter and bolometer model," *J. Appl. Phys.* **93**, 4856 (2003).

Gao, B., A. Komnik, R. Egger, D.C. Glattli, and A. Bachtold, "Evidence for Luttinger-liquid behavior in crossed metallic single-wall nanotubes," *Phys. Rev. Lett*. **92**, 216804 (2004).

Gershenzon, E.M., M.E. Gershenzon, G.N. Gol'tsman, A.M. Lyul'kin, A.D. Semenov, and A.V. Sergeev, "Electron-phonon interaction in ultrathin Nb films," *Sov. Phys. JETP* **70**, 505 (1990).

Gupta, K.C., R. Garg, and I.J. Bahl, *Microstrip Lines and Slotlines*, Norwood, MA: Artech House, Inc. (1979).

Han, P.Y., M. Tani, M. Usami, S. Kono, R. Kersting, and X.-C. Zhang, "A direct comparison between terahertz time-domain spectroscopy and far-infrared Fourier transform spectroscopy," *J. Appl. Phys.* **89**, 2357 (2001).

Heersche, H.B., P. Jarillo-Herrero, J.B. Oostinga, L.M.K. Vandersypen, A.F. Morpurgo, "Bipolar supercurrent in graphene," *Nature* **446**, 56 (2007).

Hong, B.H., J.Y. Lee, T. Beetz, Y. Zhu, P. Kim and K.S. Kim, "Quasi-continuous growth of ultralong carbon nanotube arrays," *J. Am. Chem. Soc*. **127**, 15336 (2005).

Hwang, T.-L., S.E. Schwarz, and D.B. Rutledge, "Microbolometers for infrared detection," *Appl. Phys. Lett.* **34**, 773 (1979).

Iijima, S., "Helical microtubules of graphitic carbon," *Nature* **354**, 56 (1991).

Iijima, S., and T. Ichihashi, "Single-shell carbon nanotubes of 1-nm diameter," *Nature* **363**, 603 (1993).

Ikushima, K., Y. Yoshimura, T. Hasegawa, S. Komiyama, T. Ueda and K. Hirakawa, "Photon-counting microscopy of terahertz radiation," *Appl. Phys. Lett.* **88**, 152110 (2006).

Irwin, K.D., "An application of electrothermal feedback for high resolution cryogenic particle detection," *Appl. Phys. Lett*. **66**, 1998 (1995).

Irwin, K.D., and K.W. Lehnert, "Microwave SQUID multiplexer," *Appl. Phys. Lett*. **85**, 2107 (2004).

Irwin, K.D., and G.C. Hilton, "Transition-edge sensors," *Cryogenic Particle Detection*, ed. Christian Enss, New York: Springer (2005), pp. 63-150.

Itkis, M.E., F. Borondics, A. Yu, and R.C. Haddon, "Bolometric infrared photoresponse of suspended single-walled carbon nanotube films," *Science* **312**, 413 (2006).

Javey, A., J. Guo, Q. Want, M. Lundstrom, and H. Dai, "Ballistic carbon nanotube field-effect transistors," *Nature* **424**, 654 (2003).

Kanda, A., K. Tsukagoshi, Y. Aoyagi and Y. Ootuka, "Gate-voltage dependence of zero-bias anomalies in multiwall carbon nanotubes," *Phys. Rev. Lett.* **92**, 036801 (2004).

Karasik, B.S., and A.I. Elantiev, "Noise temperature limit of a superconducting hot-electron bolometer mixer," *Appl. Phys. Lett.* **68**, 853 (1996).

Karasik, B.S., W.R. McGrath, H.G. LeDuc and M.E. Gershenson, "A hot-electron direct detector for radioastronomy," *Supercond. Sci. Technol.* **12**, 745 (1999).

Karasik, B.S., and A.V. Sergeev, "THz hot-electron photon counter," *IEEE Trans. Appl. Supercond.* **15**, 618 (2005).

Kasumov, A.Yu., R. Deblock, M. Kociak, B. Reulet, H. Bouchiat, I.I. Khodos, V.T. Volkov, C. Journet, and M. Burghard, "Supercurrents through single-walled carbon nanotubes," *Science* **284**, 1508 (1999).

Kibis, O.V., M. Rosenau da Costa, and M.E. Portnoi, "Generation of terahertz radiation by hot electrons in carbon nanotubes," *Nano Lett.* **7**, 3414 (2007).

Klapwijk, T.M, G.E. Blonder, and M. Tinkham, "Explanation of subharmonic energy gap structure in superconducting contacts," *Physica* **109 & 100B**, 1657 (1982).

Kollberg, E.L. and K.S. Yngvesson, "Quantum-noise theory for terahertz hot electron bolometer mixers," *IEEE Trans. Microwave Theory Tech.* **54**, 2077-2089 (2006).

Koller, D., G.A. Ediss, L. Mihaly, and G.L. Carr, "Infrared measurements of possible IR filter materials," *Int. J. Infrared and Millimeter Waves* **27**, 835 (2007).

Komiyama, S., O. Astafiev, V. Antonov, T. Kutsuwa and H. Hirai, "A single-photon detector in the far-infrared range," *Nature* **403**, 405 (2000).

Kurtz, A.D., S.A. Kulin, and B.L. Averbach, "Effect of dislocations on the minority carrier lifetime in semiconductors," *Phys. Rev.* **101**, 1285 (1956).

Landau, L.D., and E.M. Lifshitz, *Statistical Physics, Third Edition*, Tarrytown, NY: Elsevier (1980).

Langley, S.P., "The bolometer," *Nature* **25**, 14 (1881).

Lawson, P.R., A. Ahmed, R.O. Gappinger, A. Ksendzov, O.P. Lay, S.R. Martin, R.D. Peters, D. P. Scharf, J.K. Wallace, and B. Ware, "Terrestrial Planet Finder Interferometer technology status and plans," *Proc. SPIE* **6268**, 626828 (2006).

Lee, A.T., P.L. Richards, S.W. Nam, B. Cabrera, and K.D. Irwin, "A superconducting bolometer with strong electrothermal feedback," *Appl. Phys. Lett.* **69**, 1801 (1996).

Leisawitz, D., "NASA's far-IR/submillimeter roadmap missions: SAFIR and SPECS," *Adv. Space Res*. **34**, 631 (2004).

le Sueur, H., and P. Joyez, "Microfabricated electromagnetic filters for millikelvin experiments," *Rev. Sci. Instrum.* **77**, 115102 (2006).

Lloyd-Hughes, J., S.K.E. Merchant, L. Fu, H.H. Tan, C. Jagadish, E. Castro-Camus, and M.B. Johnston, "Influence of surface passivation on ultrafast carrier dynamics and terahertz radiation generation in GaAs," *Appl. Phys. Lett.* **89**, 232102 (2006).

Loettgers, A., "Samuel Pierpont Langley and his contributions to the empirical basis of black-body radiation," *Phys. Perspect.* **5**, 262 (2003).

Lukashenko, A., and A.V. Ustinov, "Improved powder filters for qubit measurements," *Rev. Sci. Instrum*. **79**, 014701 (2008).

Luukanen, A., L. Gronberg, T. Haarnoja, P. Helisto, K. Kataja, M. Leivo, A. Rautiainen, J. Penttila, J.E. Bjarnason, C.R. Dietlein, M.D. Ramirez, and E.N. Grossman, "Passive THz imaging system for stand-off identification of concealed objects: results from a turn-key 16 pixel imager," *Proc. SPIE* **6948**, 69480O (2008).

Mann, D., A. Javey, J. Kong, W. Wang, and H. Dai, "Ballistic transport in metallic nanotubes with reliable Pd ohmic contacts," *Nano Lett.* **3**, 1541 (2003).

Martinis, J.M., M.H. Devoret, and J. Clarke, "Experimental tests for the quantum behavior of a macroscopic degree of freedom: The phase difference across a Josephson junction," *Phys. Rev. B* **35,** 4682 (1987).

Mather, J.C., "Bolometer noise: nonequilibrium theory," *Appl. Opt.* **21**, 1125 (1982).

Maune, H., H.-Y. Chiu, and M. Bockrath, "Thermal resistance of the nanoscale constrictions between carbon nanotubes and solid substrates," *Appl. Phys. Lett.* **89**, 013109 (2006).

Mazin, B.A., P.K. Day, K.D. Irwin, C.D. Reintsema, and J. Zmuidzinas, "Digital readouts for large microwave low-temperature detector arrays," *Nucl. Inst. Meth. Phys. Res. A* **559**, 799 (2006).

McEuen, P.L., M.S. Fuhrer, and H. Park, "Single-walled carbon nanotube electronics," *IEEE Trans. Nanotech.* **1**, 78 (2002).

Milliken, F.P., J.R. Rozen, G.A. Keefe, and R.H. Koch, "50 Ω characteristic impedance low-pass metal powder filters," *Rev. Sci. Instrum*. **78**, 024701 (2007).

Moseley, S.H., J.C. Mather, and D. McCammon, "Thermal detectors as x-ray spectrometers," *J. Appl. Phys.* **56**, 1257 (1984).

Nagaev, K.E., "Influence of electron-electron scattering on shot noise in diffusive contacts," *Phys. Rev. B* **52**, 4740 (1995).

Nahum, M., and J.M. Martinis, "Ultrasensitive-hot-electron microbolometer," *Appl Phys. Lett.* **63**, 3075 (1993).

Nemilentsau, A.M., G. Ya. Slepyan, and S.A. Maksimenko, "Thermal radiation from carbon nanotubes in the terahertz range," *Phys. Rev. Lett.* **99**, 147403 (2007).

Nosho, Y., Y. Ohno, S. Kishimoto, and T. Mizutani, "Relation between conduction property and work function of contact metal in carbon nanotube field-effect transistors," *Nanotechnology* **17**, 3412 (2006).

Oreg, Y., and A.M. Finkel'stein, "Suppression of T_c in superconducting amorphous wires," *Phys. Rev. Lett.* **83**, 191 (1999).

Park, J.-Y., S. Rosenblatt, Y. Yaish, V. Sazonova, H. Usunel, S. Braig, T.A. Aria, P.W. Bouwer and P.L. McEuen, "Electron-phonon scattering in metallic single-walled carbon nanotubes," *Nano Lett*. **4**, 517 (2004).

Park, M.-J., J. Choi, and S.-S. Kim, "Wide bandwidth pyramidal absorbers of granular ferrite and carbonyl iron powders," *IEEE Trans. Mag*. **36**, 3272 (2000).

Perebeinos, V., S.V. Rotkin, A.G. Petrov and P. Avouris, "The effects of substrate phonon mode scattering on transport in carbon nanotubes," *Nano Lett.* **9**, 312 (2009).

Petrov, A.G., and S.V. Rotkin, "Energy relaxation of hot carriers in single-wall carbon nanotubes by surface optical phonons of the substrate," *JETP Lett.* **84**, 156 (2006).

Pop, E., D. Mann, J. Cao, Q. Wang, K. Goodson and H. Dai, "Negative differential conductance and hot phonons in suspended nanotube molecular wires," *Phys. Rev. Lett*. **95**, 155505 (2005).

Pop, E., D. Mann, Q. Wang, K. Goodson and H. Dai, "Thermal conductance of an individual single-wall carbon nanotube above room temperature," *Nano Lett.* **6**, 96 (2006).

Pop, E., D.A. Mann, K. Goodson and H. Dai, "Electrical and thermal transport in metallic single-wall carbon nanotubes on insulating substrates," *J. Appl. Phys.* **101**, 093710 (2007).

Prasher, R., "Predicting the thermal resistance of nanosized constrictions," *Nano Lett.* **5**, 2155 (2005).

Prober, D.E., "Superconducting terahertz mixer using a transition-edge microbolometer," *Appl. Phys. Lett.* **62**, 2119 (1993).

Purewal, M.S., B.H. Hong, A. Ravi, B. Chandra, J. Hone and P. Kim, "Scaling of resistance and electron mean free path of single-walled carbon nanotubes," *Phys. Rev. Lett*. **98**, 186808 (2007).

Purewal, M.S., "Electron transport in single-walled carbon nanotubes," Ph.D. dissertation, Columbia University (2008).

Radosavljevic, M., M. Freitag, K.V. Thadani, and A.T. Johnson, "Nonvolatile molecular memory elements based on ambipolar nanotube field effect transistors," *Nano Lett.* **2**, 761 (2002).

Rana, F., "Graphene terahertz plasmon oscillators," *IEEE Trans. Nanotech.* **7**, 91 (2008).

Reese, M.O., "Superconducting hot electron bolometers for terahertz sensing," Ph.D. dissertation, Yale University (2006).

Reese, M.O., D.F. Santavicca, L. Frunzio, and D.E. Prober, "Niobium hot electron bolometer development for a submillimeter heterodyne array camera," *IEEE Trans. Appl. Supercond.* **17**, 403 (2007).

Richards, P.L., J. Clarke, R. Leoni, Ph. Lerch, S. Verghese, M.R. Beasley, T.H. Geballe, R.H. Hammond, P. Rosenthal, and S.R. Spielman, "Feasibility of the high T_c superconducting bolometer," *Appl. Phys. Lett.* **54**, 283 (1989).

Richards, P.L., "Bolometers for infrared and millimeter waves," *J. Appl. Phys.* **76**, 1 (1994).

Richards, P.L., "Bolometric detectors for measurements of the cosmic microwave background," *J. Supercond: Incorp. Nov. Mag.* **17**, 545 (2004).

Rodriguez-Morales, F., R. Zannoni, J. Nicholson, M. Fischetti, and K.S. Yngvesson, "Direct and heterodyne detection of microwaves in a metallic single wall carbon nanotube," *Appl. Phys. Lett.* **89**, 083502 (2006).

Rogovin, D. and D.J. Scalapino, “Fluctuation phenomena in tunnel junctions,” *Ann. Phys.* **86**, 1 (1974).

Rotkin, S.V., V. Perebeinos, A.G. Petrov and P. Avouris, “An essential mechanism of heat dissipation in carbon nanotube electronics,” *Nano Lett.* **9**, 1850 (2009).

Rutherglen, C., D. Jain, and P. Burke, “Rf resistance and inductance of massively parallel single walled carbon nanotubes: Direct, broadband measurements and near perfect 50 Ω impedance matching,” *Appl. Phys. Lett.* **93**, 083119 (2008).

Rutledge, D.B., D.P. Neikirk, and D.P. Kasilingam, “Integrated-circuit antennas,” *Infrared and Millimeter Waves* **10**, ed. K.J. Button, New York: Academic Press, Inc. (1983), pp. 1-90.

Ryzhii, V., M. Ryzhii, and T. Otsuji, “Negative dynamic conductivity of graphene with optical pumping,” *J. Appl. Phys.* **101**, 083114 (2007).

Santavicca, D.F., M.O. Reese, A.B. True, C.A. Schmuttenmaer, and D.E. Prober, “Antenna-coupled niobium bolometers for terahertz spectroscopy,” *IEEE Trans. Appl. Supercond.* **17**, 412 (2007).

Santavicca, D.F., A.J. Annunziata, M.O. Reese, L. Frunzio, and D.E. Prober, “A far-infrared Fourier transform spectrometer with an antenna-coupled niobium bolometer,” *Supercond. Sci. Technol.* **20**, S398 (2007).

Santavicca, D.F., and D.E. Prober, “Impedance-matched low-pass stripline filters,” *Meas. Sci. Technol.* **19**, 087001 (2008).

Santavicca, D.F., and D.E. Prober, “Terahertz resonances and bolometric response of a single-walled carbon nanotube," *Proc. 33rd Int. Conf. on IR, Millimeter and THz Waves* (IRMMW-THz 2008).

Santavicca, D.F., B. Reulet, B.S. Karasik, S.V. Pereverzev, D. Olaya, M.E. Gershenson, and D.E. Prober, “Energy resolution of terahertz single-photon-sensitive bolometric detectors,” arXiv:0906.1205 (2009).

Santhanam, P. and D.E. Prober, “Inelastic electron scattering mechanisms in clean aluminum films,” *Phys. Rev. B* **29**, 3733 (1984).

Schiffres, P., “A dissipative coaxial RFI filter,” *IEEE Trans. Electromag. Compat.* **6**, 55 (1964).

Schmuttenmaer, C.A., “Exploring dynamics in the far-infrared with terahertz spectroscopy,” *Chem. Rev.* **104**, 1759 (2004).

Semenov, A.D., H. Richter, H.-W. Hubers, B. Gunther, A. Smirnov, K.S. Il'in, M. Siegel, and J.P. Karamarkovic, "Terahertz performance of integrated lens antennas with a hot-electron bolometer," *IEEE Trans. Microwave Theory Tech.* **55**, 239 (2007).

Sherwin, M.S., C.A. Schmuttenmaer, and P.H. Bucksbaum, eds., "Opportunities in THz Science," Report of DOE-NSF-NIH Workshop, Feb. 2004.

Shi, L., J. Zhou, P. Kim, A. Bachtold, A. Majumdar, and P.L. McEuen, "Thermal probing of energy dissipation in current-carrying carbon nanotubes," *J. Appl. Phys.* **105**, 104306 (2009).

Siddiqi, I., "Critical temperature dependence of high frequency electron dynamics in superconducting hot-electron bolometer mixers," Ph.D. dissertation, Yale University (2002).

Skalare, A., Th. De Graauw, and H. van de Stadt, "A planar dipole array antenna with an elliptical lens," *Microwave and Optical Tech. Lett.* **4**, 9 (1991).

Skocpol, W.J., M.R. Beasley, and M. Tinkham, "Self-heating hotspots in superconducting thin-film microbridges," *J. Appl. Phys.* **45**, 4054 (1974).

Slichter, D.H., O. Naaman, and I. Siddiqi, "Millikelvin thermal and electrical performance of lossy transmission line filters," *Appl. Phys. Lett*. **94**, 192508 (2009).

Smith, P.R., D.H. Auston, and M.C. Nuss, "Subpicosecond photoconducting dipole antennas," *IEEE J. Quantum Electronics* **24**, 255 (1988).

Spietz, L., "The shot noise thermometer," Ph.D. dissertation, Yale University (2006).

Steinbach, A.H., J.M. Martinis, and M.H. Devoret, "Observation of hot-electron shot noise in a metallic resistor," *Phys. Rev. Lett.* **76**, 3806 (1996).

Swinyard, B., and T. Nakagawa, "The space infrared telescope for cosmology and astrophysics: SPICA A joint mission between JAXA and ESA," *Exp. Astron.* **23**, 193 (2009).

Tarasov, M., J. Svensson, L. Kuzmin, and E.E.B. Campbell, "Carbon nanotube bolometers," *Appl. Phys. Lett.* **90**, 163503 (2007).

Tinkham, M., *Introduction to Superconductivity, Second Edition*, Mineola, NY: Dover Publications (1996).

True, A.B., "Terahertz spectroscopy of amino acid enantiomers and polymorphs," Ph.D. dissertation, Yale University (2008).

Turner, G.M, M.C. Beard, and C.A. Schmuttenmaer, "Transient photoconductivity in dye-sensitized nanocrystalline TiO_2 films as measured by time-resolved THz spectroscopy," *J. Phys. Chem. B* **106**, 11716 (2002).

van der Vorst, M.J.M., "Integrated lens-antennas for submillimetre-wave applications," Ph.D. dissertation, Technical University of Eindhoven (1999).

van Exter, M., and D.R. Grischkowsky, "Characterization of an optoelectronic beam system," *IEEE Trans. Microwave Theory Tech.* **38**, 1684 (1990).

Vion, D., P.F. Orfila, P. Joyez, D. Esteve, and M.H. Devoret, "Miniature electrical filters for single-electron devices," *J. Appl. Phys*. **77,** 2519 (1995).

Wei, J., D. Olaya, B.S. Karasik, S.V. Pereverzev, A.V. Sergeev, and M.E. Gershenson, "Ultrasensitive hot-electron nanobolometers for terahertz astrophysics," *Nature Nanotech.* **3**, 496 (2008).

Weinreb, S., J. Bardin, H. Mani, and G. Jones "Matched wideband low-noise amplifiers for radio astronomy," *Rev. Sci. Instrum.* **80**, 044702 (2009).

Wellstood, F.C., C. Urbina, and J. Clarke, "Hot-electron effects in metals," *Phys. Rev. B* **49**, 5942 (1994).

Yao, Z., C.L. Kane and C. Dekker, "High field electrical transport in single-wall carbon nanotubes," *Phys. Rev. Lett.* **84**, 2941 (2000).

Yngvesson, K.S., "Very wide bandwidth hot electron bolometer heterodyne detectors based on single-walled carbon nanotubes," *Appl. Phys. Lett.* **87**, 043503 (2005).

Zmuidzinas, J., and P.L. Richards, "Superconducting detectors and mixers for millimeter and submillimeter astrophysics," *Proc. IEEE* **92**, 1597 (2004).

Zorin, A.B., "The thermocoax cable as the microwave frequency filter for single electron circuits," *Rev. Sci. Instrum*. **66**, 4296 (1995).